Real-Time Core-Hole Dynamics in X-ray Spectroscopy

Andrew J. Lee

A dissertation
submitted in partial fulfillment of the
requirements for the degree of

Doctor of Philosophy

University of Washington

2014

Reading Committee:

John J. Rehr, Chair

George F. Bertsch

Gerald T. Seidler

Program Authorized to Offer Degree:
UW Physics

University of Washington

Abstract

Real-Time Core-Hole Dynamics in X-ray Spectroscopy

Andrew J. Lee

Chair of the Supervisory Committee:
Professor John J. Rehr
Physics

While experimental developments have enabled the study of core-hole dynamics in X-ray spectroscopy, theoretical methods for dynamical effects are still underdeveloped. Additionally, traditional theoretical methods are in frequency space, in which the study of real-time dynamics does not come naturally. We develop a real-time formalism for calculating ordinary and time-dependent X-ray spectra. While we focus our calculations on ordinary (linear) XAS, we keep our methods sufficiently general that they are readily applied to pumped and nonlinear XAS. We combine DFT, TDDFT, and the Nozières-De Dominicis (ND) formalism to produce a real-time approach to model core-hole dynamics in X-ray spectroscopy. This method is based on a real-time time-correlation function. While the correlation function can be used alone, we also present a further approximation where we obtain the full Green's function as a convolution of the single-particle photoelectron Green's function calculated via the correlation function method, and the core-hole Green's function calculated via a cumulant expansion based approach. The cumulant expansion is obtained from the density response of the valence electrons to the core hole. Calculations for diamond, C_{60}, and graphite are presented. Our calculations reproduce frequency space calculations based on the ND formalism. However, in our method the photoelectron interacts with dynamic valence electrons, unlike in frequency space methods.

TABLE OF CONTENTS

Page

LIST OF FIGURES

GLOSSARY

CORE HOLE: the unfilled core level orbital left behind by an ejected electron. If one considers the electron–hole pair as an excitation from the ground state, the hole carries an effective positive charge.

CORE-HOLE GREEN'S FUNCTION: the Green's function giving the probability of the system reacting to the creation of a core hole and ending up at a particular energy. Note that this is distinct from the mathematical term in the study of differential equations. The core-hole Green's function is denoted as g_c.

CUMULANT EXPANSION: the Taylor expansion of the logarithm of a Green's function. In the thesis, it is used to calculate the core-hole Green's function.

DFT: density functional theory. A reformulation of quantum mechanics in terms of the particle density.

EELS: electron energy loss spectroscopy. An electron is scattered off the system and the momentum transfer and energy loss are measured.

EXCITON: a bound electron–hole pair treated as a single excitation. The electron is also called a photoelectron if it was excited by a photon.

KS: Kohn-Sham. In the KS formulation of DFT and TDDFT, fictitious KS particles interact only with an external KS potential which is a functional of the total particle density. The complicated many-body physics is contained in the exchange-correlation (XC) part of the density-functional.

ND: the classic Nozières-De Dominicis formalism for calculating XAS. The core-hole is treated as an effective external perturbation on non-interacting non-core electrons. The total Green's function (F) is split into the core-hole Green's function (g_c) and the photoelectron Green's function (G).

PAW: the Projector Augmented Wavefunctions method. The PAW provides a smooth and efficient representation of wavefunctions, from which the physical "all-electron" wavefuctions can be reconstructed as needed.

PBE: the Perdew-Burke-Ernzerhof exchange-correlation (XC) functional, a form of Generalized Gradient Approximation (GGA). We use its adiabatic extension for the XC in our TDDFT calculations.

PHOTOELECTRON: the electron created by exciting an electron to above the Fermi level.

PHOTOELECTRON GREEN'S FUNCTION: the photoelectron Green's function gives the probability of a photoelectron being created at a certain energy. Also referred to as the "transient Green's function." The photoelectron Green's function is denoted as G.

TDDFT: time-dependent density functional theory. A reformulation of time-dependent quantum mechanics in terms of the time-dependent density.

TRANSIENT GREEN'S FUNCTION: see "photoelectron Green's function."

XAS: X-ray absorption spectroscopy. The X-ray excites a core electron to create a core hole and a photoelectron in a level above the Fermi energy. The intensity of light absorbed is measured.

XC: the exchange-correlation functional. Often also referred to as the "kernel" or "functional." A part of the KS density-functional external potential, the XC term contains information on the many-body physics. In practice it needs to be approximated. We use the PBE approximation and its adiabatic extension in the thesis.

XPS: X-ray photoelectron spectroscopy. Like in XAS, the X-ray excites a core electron to create a core hole. However, in XPS the photoelectron has enough energy to exit the system, and the energy of the photoelectron is measured.

ACKNOWLEDGMENTS

I thank my adviser, Professor John Rehr, for providing the opportunity to work on computational electronic structure theory, and for his guidance and encouragement.

I thank Professor George Bertsch, for his guidance, for his interest and support for my ideas, and for his deep theoretical insights.

I thank Professor Gerald Seidler, for his encouragement to keep thinking big. During the development of theory, I always kept his vision in mind.

I thank Dr. Joshua Kas for the many helpful discussions and explanations regarding X-ray spectroscopy, Dr. Fernando Vila for his insights in real-time methods and quantum chemistry, Dr. Kevin Jorissen for his feedback and advice, and Dr. John Vinson for his helpful discussions and his help in using part of the code from his project, OCEAN.

I thank Shunsuke Sato and Professor Kazuhiro Yabana for their collaboration.

I thank my colleagues Dr. Towfiq Ahmed, Egor Klevak, Shauna Story, Erik Lentz, Scott Hayashi, and Siri Vimolchalao, for their friendship, support, encouragement, and discussions.

Finally I would like to thank the members of my supervisory committee, Professors John Rehr, George Bertsch, Gerald Seidler, Subhadeep Gupta, Anton Andreev, Stephen Sharpe, and Christine Luscombe, and former member James Mayer.

DEDICATION

to my dear mother and father

Chapter 1

INTRODUCTION

This dissertation focuses on real-time methods for the study of X-ray spectroscopy. While experimental methods have long existed for probing the dynamics of electronic structures with X-ray spectroscopy, the theoretical study of dynamics is still in the early stages of development. Methods for modelling dynamics are actively being developed and are in the forefront of current electronic theory research [1]. Traditional methods, which are in frequency space, have both conceptual and computational difficulty in modeling dynamics. The most natural way is to instead model electronic structure systems in real-time. Recently, real-time methods have been used to study non-linear dynamics in the context of optical absorption [2]. However, the extension of optical absorption methods to X-ray absorption methods is not straightforward. In this dissertation we seek to develop real-time methods applicable to X-ray spectroscopy.

This chapter motivates the study of X-ray absorption spectroscopy (XAS), describes the role core-hole dynamics plays in the understanding of XAS, and discusses real-time methods for the study of core-hole dynamics. We also define the purpose of this thesis and give an overview.

In X-ray absorption spectroscopy, a core electron absorbs an X-ray photon and jumps to an unoccpied orbital. This provides information about the local electronic structure in the vicinity of the absorber, unlike optical absorption [3]. Such information is useful in studying the local chemical properties of the system, and material properties such as the band gap [4]. The XAS can be approximated as the unoccupied density of states projected onto the dipole operator operating on a core wavefunction. For example, a spherically symmetric $1s$ core state will become a p wave upon operation by the dipole operator, and the XAS is approximately the unoccupied density of states projected onto this p wave. Since the core state is well localized, the projection is local to the absorber. In this way XAS provides an approximate local view of the unoccupied density of states.

X-ray emission spectroscopy (XES), also provides information about the local electronic structure in the vicinity of the absorber, but this time about the occupied levels [5]. In this way it gives complementary information to XAS. XES can be modeled with similar theoretical techniques as XAS. We will mostly focus on XAS in this thesis. However the discussions of XAS can be readily extended to XES.

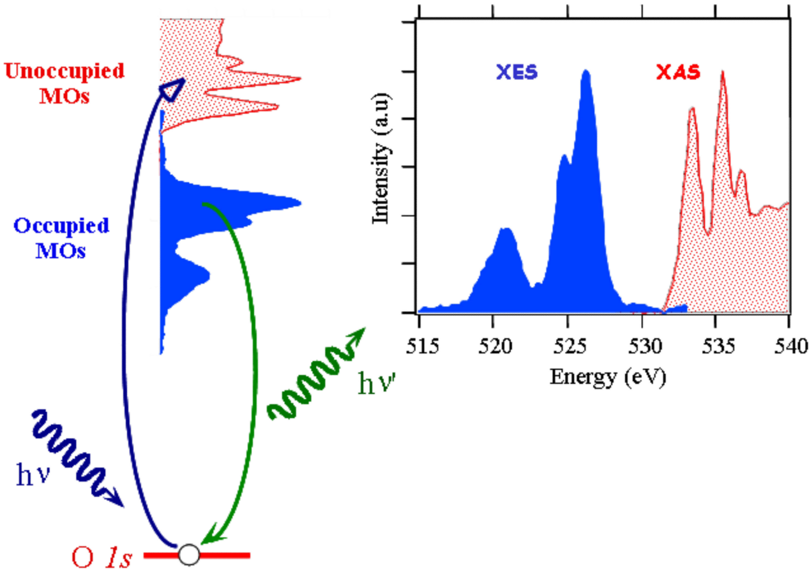

Figure 1.1: Schematic of X-ray Absorption/Emission Spectroscopy (XAS/XES) transitions for an Oxygen absorber. In XAS, a photon is absorbed by the photoelectron initially occupying the core orbital (dark blue wavy line) and the photoelectron jumps to an unoccupied molecular orbital (MO). The energy of the absorbed photon is the energy difference of the core and final orbitals. In XES, an electron from an occupied MO falls into the empty core orbital (core hole) created by a prior absorption event, emitting a photon of the energy difference between the initial and core orbitals. $h\nu$: photon energy. a.u.: arbitrary units. *Source:* Dong *et al.* [4], Copyright © SPIE. Reused with permission.

The theory of XAS is complicated by the creation of the core hole. The electrons dynamically respond to and screen the core hole, which is effectively an additional positive charge density[1]. Therefore the density of states changes to reflect this. Furthermore, the shake up of the valence electrons also absorbs energy which is not accounted for in the projected-density-of-states approximation. Although this description focuses on XAS, other types of X-ray spectroscopy also require an understanding of core-hole dynamics. Furthermore, the system will always dynamically respond to the probe.

Dynamics is of even greater importance in spectroscopy techniques like pump-probe XAS which fundamentally probes dynamics and therefore cannot be modeled with traditional methods [1]. In the classic pump-probe experiments, a pumping laser excites the system and a second laser then acts as the probe for an absorption measurement. The first and second laser pulses can vary in time, so the dynamics of the reaction to the first pulse is probed by the second. The recent experimental development of the X-ray Free Electron Lasers (XFELs), a new class of lasers, can be used in pump-probe experiments at very high temporal and spatial resolution [6]. Each pulse can be as short as 7 fs [7], allowing for fine time resolution. The fine time resolution allows pump-probe experiments to probe dynamics in more detail.

Furthermore XFELs can probe the effects of multiple core holes in X-ray spectroscopy [8]. For example, multiple core holes have be created in an experiment on Neon gas [9]. The multiple excitons can dynamically affect each other, and the XAS becomes nonlinear, i.e. the XAS becomes no longer a linear function of photon intensity. Core-hole dynamics plays a central role in this regime. Since the first absorption event leaves the system in an excited state, the second absorption event requires modeling of the time-dependent dynamics. The methods developed in this thesis can readily address pump-probe and multiphoton absorption. Further extensions may be able to treat time-dependent Auger emission, which become non-linear and time-dependent in XFEL experiments with a focused beam [8].

The first XFEL source, the Linac Coherent Light Source (LCLS), first came online in 2009. Since then the technology has improved and the pulses will continue to become brighter and shorter. The LCLS represents the beginning of a new age of X-ray spectroscopy, where the dynamics of electronic structure plays an even greater role than before [10].

---

[1] In XES the a similar problem arises from the system reacting to the annihilation of the core hole.

The development of theoretical methods for modeling the electronic structure dynamics observed in these experiments involves sophisticated techniques. Since the direct solution of a many-body quantum mechanical system is impractical, Kohn-Sham Density Functional Theory (KS DFT) and its time dependent extension (KS TDDFT) are often employed in the study of electronic structure theory [11]. DFT replaces interacting electrons with fictitious KS particles that have the same density as the true system. Since we are interested in dynamics, we focus on TDDFT, from which we may obtain the time dependent electronic density [12]. TDDFT brings great effiency advantages over explicit time evolution of the true many-body state. However, observables need to be expressed as a functional of the density. While in theory all observables can be obtained from the density, in practice it is difficult to construct the required expressions.

To this end, we may look to methods from optical spectroscopy. In 1996, Yabana and Bertsch developed a real-time TDDFT (RT-TDDFT) method for obtaining the optical spectrum from dipole response [13]. The dipole response is the function of time obtained by integrating the density times the dipole field, and therefore it is simple to obtain from RT-TDDFT. In 2007, Takimoto *et al.* developed an RT-TDDFT method for non-linear optical absorption spectroscopy [2]. Takimoto *et al.* found that the real-time method using a Crank-Nicolson propagator implemented with a predictor-corrector scheme is numerically stable enough for practical calculations and scales much better than frequency space methods for large systems.

However, the frequency of the X-ray field presents difficulties in adapting the methods developed for optical response to X-ray absorption. In a direct attempt to obtain the dipole response for X-ray fields in the same way as for optical fields, one requires explicit modelling of the core electron and an extremely small time step relative to the total simulation time. The X-ray energy is on the order of 1000 eV which is very large compared with the energy scale of the features in the near-edge XAS, which are on the order of 0.1 eV or greater. In terms of times, the period of an X-ray field is in attoseconds and below. The period of the oscillations we are interested in, which come from energy differences in the XAS peaks, is in hundreds to thousands of attoseconds. Therefore the response would oscillate at a frequency much larger than the differences in features we are interested in, meaning our time step would be much smaller than time scale of interest. Furthermore, as will be discussed in Chapter 3, it is in practice difficult to approximate the core-valence and valence-valence correlations simultaneously within a single determinant in TDDFT.

We bypass modelling the X-ray field and core electrons explicitly by deriving an expression from the dipole response that has the form of a time-correlation function of KS states from KS TDDFT. This form allows us to factor out the high frequency oscillation, and to insert the photoelectron and effective core-hole potential by hand without having to excite an explicit core electron via an explicit X-ray field. The time correlation based methods can be applied to obtain the spectrum directly, or they can be combined with the valence core-hole response so that the spectrum becomes a convolution between a time correlation function and a Green's function describing the shakeup of the valence electrons due to the creation of the core hole.

1.1 Organization of the thesis

The rest of this chapter gives an overview of electronic structure theory and X-ray spectroscopy and their standard theoretical approaches. Chapter 2 describes adapting Fermi's golden rule to a real-time formalism. Chapter 3 introduces a two-determinant approximation for X-ray spectroscopy. Chapter 4 is the main theoretical chapter and describes how to derive a practical real-time method for exploring time-dependent X-ray dynamics from the response in a two-determinant approximation. Calculations in later chapters are based on the formal developments in Chapter 4. Chapter 5 presents calculations using a convolved Green's function approach based on ND, where the photoelectron correlation function is convolved with the core-hole Green's function. The core-hole Green's function is obtained via considering the density response of the valence electrons to the core hole. Chapter 6 describes time-dependent experiments that our real-time methods can be applied to and future directions for real-time X-ray spectroscopy. Appendices A and B describe the Real Time X-ray Spectroscopy (RTXS) software package developed for the calculations in the thesis. Appendix C describes a time-shifted correlation function based approach for calculating X-ray spectra. Appendix D contains technical details that are referred to as needed.

1.2 Conventions and notations

Throughout this thesis we use Hartree atomic units, $m = e = \hbar = 1$.

We use bold symbols to indicate the physical many-body operators and wavefunctions and ordinary symbols for Kohn-Sham effective single-particle operators and wavefunctions. For example, $\mathbf{H}$ is a many body Hamiltonian, whereas H is a single particle Kohn-Sham Hamiltonian. $|\mathbf{\Psi}\rangle$ is a many body wavefunction while $|\psi\rangle$ is a single particle wavefunction.

We place a tilde on top of wavefunctions and partial waves to denote pseudized versions, whereas symbols without the tilde are taken to refer to all-electron versions. For example, $|\tilde{\psi}\rangle$ is a pseudo-wavefunction whose corresponding all-electron wavefunction is $|\psi\rangle$.

We place a prime on quantities containing an effective core hole potential, or evolving under such a potential.[2] For example, H is the Kohn-Sham Hamiltonian before a core hole is introduced, while H' is the Hamiltonian with an effective core hole potential. Furthermore, if $|\psi_i(t)\rangle$ is a Kohn-Sham single-particle wavefunction evolving under H, then $|\psi_i'(t)\rangle$ is a wavefunction evolving under H'.

Note that Chapters 2 and 3 are copies of published papers and do not necessarily follow the conventions described here.

1.3 Overview of methods in X-ray spectroscopy

There are various X-ray spectroscopy techniques which are useful in probing electronic structure. We are mainly interested in X-ray absorption spectroscopy (XAS) and X-ray absorption near edge structure (XANES). The electron energy loss spectroscopy (EELS) and X-ray photoemission spectroscopy (XPS) experimental data can be used to check the different quantities that go into a calculation of XAS.

For XAS, in each absorption event a core-level electron is excited by a photon of known energy into an unoccupied state. The detector measures the number of photons transmitted, and from that one obtains the amount of absorption as a function of photon frequency. This gives information about the unoccupied energy levels. In their classic work, Nozières and

---

[2] We model the creation of a core hole by turning on an effective core-hole potential. We do not explicitly model core-level wavefunctions.

De Dominicis (ND) realized that one can describe the XANES with a Green's function where a photoelectron and structureless core-hole are created at the time of absorption, then evolved, with the system under the influence of an effective core-hole potential, and annihilated at a later time [14]. The ND Green's function for XAS and the spectrum are given by

$$F(t) = \lim_{\delta t \to 0^+} i \langle \boldsymbol{\Psi}_g | c_c^\dagger(t) c_x(t - \delta t) c_x^\dagger(0 + \delta t) c_c(0) | \boldsymbol{\Psi}_g \rangle \tag{1.1}$$

$$\mu(\omega) = \Im \frac{1}{\pi} \int_0^\infty dt e^{i\omega t} F(t). \tag{1.2}$$

This describes the process where a core hole and photoelectron are created at time 0 when the system is in the ground state $\boldsymbol{\Psi}_g$, then both destroyed at time t. The operator c_c creates a core hole and $c_x^\dagger$ creates a photoelectron. One of the goals of this thesis is to calculate the Green's function F and obtain the spectrum $\mu(\omega)$ in a suitable approximation. The other goal, which is broader and parallel to the first, is to develop a method that can be adapted to time dependent XAS and other X-ray spectroscopies, where there may be multiple absorption events or a pumping field. Therefore while we focus on F for most of this thesis, we shall keep the other goal in mind and develop methods which are sufficiently general.

The traditional method to calculate XAS is to approximate Fermi's golden rule in frequency space. In Fermi's Golden Rule the spectrum is given by the equation

$$\mu(\omega) = 2\pi \sum_{k'} |\langle \boldsymbol{\Psi}_i | c_x^\dagger c_c | \boldsymbol{\Psi}_g \rangle|^2 \delta_\Gamma(\omega - \epsilon_i) \theta(\omega - E_F), \tag{1.3}$$

where ω is the energy of the incoming photon, c_c creates a core hole, c_x creates a photoelectron in the state $d|c\rangle$ where d is the dipole operator representing the electric field and $|c\rangle$ is the core state, $\boldsymbol{\Psi}_g$ is the ground state many body wavefunction, Γ is the core-hole lifetime, $\boldsymbol{\Psi}_i$ is a many body eigenstate with energy ϵ_i, E_F is the Fermi energy, and $\delta_\Gamma(\omega) = \frac{1}{\pi} \frac{\Gamma^2}{\omega^2 + \Gamma^2}$.

Since the many body eigenstates are impractical to calculate, to simplify we use the Δ Self Consistent Field (ΔSCF) approximation. There are a few variations depending on how one treats the valence electrons. In the initial-state rule (ISR), the valence electrons are approximated as not reacting at all to the X-ray. In the final-state rule (FSR), valence electrons are approximated as going directly to the new ground state under the effective core-hole potential. In the transition state potential approximation, the valence electrons are approximatated as going directly to the new ground state under an effective core-hole potential with half the physical strength [3]. The common theme is that the valence wavefunctions are approximated as going to some state that can be modeled as an SCF KS state. Within these approximations, the valence-electron parts of the many-body wavefunction can be dropped from Eq. 1.3, since the absorption event is assumed to cause the valence electrons to transition with complete certainty into our chosen state. The spectrum is given by

$$\mu(\omega) = 2\pi \sum_{k'} |\langle k'|d|c\rangle|^2 \delta_\Gamma(E - \epsilon_{k'})\theta(E - E_F), \tag{1.4}$$

where k' is a single particle eigenstate of the Kohn-Sham Hamiltonian H' where the valence density is given by our chosen approximation.

Note that the formulation does not include any dynamical effects, and the effect of the valence electrons is to statically screen the core-hole potential in the calculation of eigenstates $|k'\rangle$. The physical reasoning behind choosing the different approximations to the valence electrons is that during the process of creating a core hole and photoelectron, the screening due to the valence electrons is assumed to be static. Only the strength of the screening needs to be chosen. If the creation of photoelectron is immediate relative to the screening, then the eigenstates "initial-state" Kohn-Sham Hamiltonian is used, where there is no core hole and the valence density is the same as in the ground state. In the approximation where the photoelectron is created very slowly, the "final-state" Kohn-Sham Hamiltonian is used, where the valence electrons are assumed to have adiabatically relaxed into the new ground state with a core hole. Both these methods can be used to calculate XAS, and sometimes they can be close to experiment, however there is no *ab initio* method to know which to use to best match experiment. Furthermore, it is empirically found that a "transition-state" Hamiltonian in some cases fits experiment best. In this approximation, the valence electrons are relaxed under a half strength effective core-hole potential.

In this thesis we go beyond the approximation of immediate or very slow creation of the photoelectron to include some dynamical effects from the interaction between the valence electrons and the core hole (intrinsic effects), and between the valence electrons and the photoelectron (extrinsic effects). In particular, we use real-time methods, which are more natural for modeling dynamics, and besides that are more intuitive since the propagators are all originally formulated in real time as opposed to frequency space.

In one method, we split up the XAS Green's function into a core-hole Green's function which includes the intrinsic interactions between the core hole and the valence electrons and a transient Green's function which models the photoelectron. The core-hole Green's function is interesting in itself since it can be compared via other spectroscopies, Electron Energy Loss Spectroscopy (EELS) and X-ray Photoemission Spectrocopy (XPS), described below. The transient Green's function is similar to the classic method of calculating XAS above, and can be compared directly to it.

In EELS, an electron is scattered off the sample, and its energy loss is measured. During the scattering event a core hole is created. EELS gives information pertaining to the charge shakeup of the system. In this work, EELS is approximately modeled by the core-hole response function $\beta(\omega)$ [15], defined below, and EELS experiment compares closely to our calculations.

$$\beta(\omega) = \frac{\omega}{\pi}\Re\int_0^\infty dte^{i\omega t}\int d^3xv_c(t)(\rho(t)-\rho(0)) \tag{1.5}$$

where v_c is the effective core-hole potential. The core-hole Green's function depends directly on β and so EELS provides a rough intermediate check. The connection is that the EELS is roughly the response due to a coulomb potential.

In XPS, the X-ray excites an electron with enough energy to leave the system and reach a detector [16]. The electron energy is measured at the detector. XPS is useful to separate the photoelectron Green's function from the core-hole Green's function. This is because the photoelectron is ejected into an energy level where the density of states is approximately flat.

1.4 General formalisms

The work of this thesis in general relies on the formalisms of Density Functional Theroy (DFT), Time-Dependent Density Functional Theory (TDDFT), and Projector Augmented

Waves (PAW). We use DFT to calculate ground states, PAW for calculatiing matrix elements for excited states, and TDDFT to evolve the excited states. This section presents these basic ingredients. There are various details and variations on this basic pattern, which will be discussed in separate chapters.

1.4.1 DFT and TDDFT

The Schrödinger equation is too complicated solve for large systems. Every particle depends on every other particle, so the problem is difficult to break apart. Furthermore the number of configurations quickly becomes unmanageable with increasing system size [11]. One method to improve efficiency is to formulate quantum mechanics in terms of the density instead of wavefunctions. The density contains much less information than the many-body state. This class of theories is called Density Functional Theory (DFT)[17]. We focus on the Kohn-Sham DFT (KS DFT) [18].

In KS DFT, the many body Hamiltonian is replaced by a single-particle Hamiltonian which is a functional of electron density. The original interacting electrons are replaced by ficticious KS electrons that interact only with the density. The density dependence is constructed so that the ground state of the KS system has the same density as the true density. The ground state density in principle can be used to calculate the ground state wavefunction $\mathbf{\Psi}_g$, and therefore all information about the ground state. The Kohn-Sham Hamiltonian is given by

$$H(\rho) = T + V_H(\rho) + V_{ext} + V_{XC}(\rho), \tag{1.6}$$

where V_H is the Hartree potential, which accounts for the electrostatic repulsion of an electron from the electron charge density, V_{ext} is an external static potential, which accounts for the nuclear charges, V_{XC} is the exchange correlation functional, which accounts for Fermi exclusion and electronic correlations. Note that in our calculations the nuclei are modeled as fixed charges and they only enter our models as part of V_{ext}.

When DFT and KS DFT were first formulated in the 1960s and given rigorous justification, there was no practical method to calculate the exchange-correlation functional. It was not until the Local Density Approximation (LDA) [19] and later the Generalized

Gradient Approximation (GGA) [20] were developed in the 1980s that DFT calculations became practical. These approximations rely on the exact exchange-correlation for a uniform electron gas, and local or semilocal functionals of the density. Throughout this thesis our calculations use the Perdew-Burke-Ernzerhof (PBE) functional [21], a form of GGA, and its adiabatic extension to TDDFT.

Both these and later approximations, while giving surprisingly accurate results for certain phenomena, are also known to have significant deficiencies [22]. For example, it is known that with GGA, charge transfer over a distance of a few angstroms generally predicts a much lower energy than in experiment [23]. Thus one must be careful to recognize the limitations of the functional when using KS DFT and KS TDDFT.

The KS ground state wavefunction is solved for self-consistently according to the coupled equations

$$\begin{aligned} H(\rho)|\psi_i\rangle &= \epsilon_i|\psi_i\rangle \\ \rho(\vec{r}) &= \sum_i \psi_i^*(\vec{r})\psi_i(\vec{r}) \end{aligned} \tag{1.7}$$

where the sum is over the states below the Fermi level.[3] The calculation consists of diagonalizing the KS Hamiltonian, obtaining a density, obtaining a new KS Hamiltonian from the new density, and so on.

While DFT is limited to solving for the ground state, TDDFT can calculate response functions of excited systems. This means TDDFT is useful in spectroscopy. For example, the optical spectrum can be obtained from the dipole response. In TDDFT the Kohn-Sham Hamiltonian is used to propagate the single particle wavefunctions.

$$i\hbar\frac{d}{dt}|\psi_i\rangle = H(\rho)|\psi_i\rangle \tag{1.8}$$

Here, $\{\psi_i\}$ are an arbitrary set of Kohn-Sham wavefunctions that can be evolved to via TDDFT propagation from the ground state wavefunction.

Formally, the DFT and TDDFT are based on two theorems, the Hohenberg-Kohn and Runge-Gross theorems.[17, 12] The Hohenberg-Kohn theorem establishes a one-to-one relationship between a static external potential, modulo a constant shift, and the ground

---

[3] Note that ψ_i are automatically orthogonal by being eigenstates of the Hamiltonian, therefore the density can be obtained without taking a determinant.

state density. This is the mathematical foundation of DFT. The Runge-Gross theorem does the same for a time-dependent external potential, modulo a constant in space, but time-dependent shift in potential. This is the mathematical foundation of TDDFT. In TDDFT, the true many body state being modeled may be excited out of the ground state by the dependent potential.

In this thesis, we add a core-hole potential as an effective external potential while evolving the wavefunctions using TDDFT. We use a half-step predictor-corrector Crank-Nicolson numerical propagator which is norm conserving and therefore numerically stable. This allows us to efficiently propagate wavefunctions with sufficient precision while using a large time step relative to other propagators, such as polynomial expansion based propagators.

1.4.2 Projector Augmented Wavefunctions

A common optimization that can be performed for DFT calculations is to neglect the core electrons, and smooth out the potentials and the valence KS wavefunctions in the core regions of atoms [24]. KS wavefunctions are highly varying in the core regions, so smoothing them out in this way improves the efficiency of their description. The pseudopotential is one way to perform this optimization. However, the method of pseudopotentials loses information about the core region. In 1990 Blochl described the Projected Augmented Wavefunction (PAW) method in which pseudopotentials were used to create pseudo-wavefunctions, yet the core region could still be reconstructed as needed [25]. GPAW implements the PAW method, which is important when calculating overlaps with the core wavefunction for XAS.

Since the core electrons do not interact significantly except when the core hole is created or destroyed, we may use the frozen core approximation where the core electrons are not evolved explicitly. In addition, valence electrons and photoelectron are smooth outside the core, which is where most of the interactions occur. Therefore the we approximate these physical wavefunctions with pseudo-wavefunctions. The physical wavefunctions are called “all-electron” wavefunctions because they are calculated in the presence of the core electrons, while the pseudo-wavefunctions are calculated with the core electrons removed and replaced with a pseudopotential chosen such that the core of the pseudo-wavefunctions are smooth.

In the Projector Augmented Wavefunction (PAW) formalism, wavefunctions are described by a combination of pseudo-wavefunctions and a core reconstruction operator, $\mathcal{T}$, that maps pseudo-wavefunctions to all-electron wavefunctions [25].

To construct the core reconstruction operator we require a set of corresponding pseudo partial waves and all-electron partial waves, which differ only in the core regions of atoms. The pseudo-wavefunctions are formally constructed from a linear combination of the pseudo partial waves, and to perform reconstruction one simply projects onto each pseudo partial wave, and adds a correction term for each partial wave. Formally we have

$$\begin{aligned} |\psi\rangle &= \mathcal{T}|\tilde{\psi}\rangle \\ &= \left(1 + \sum_{A,i_A} \Big(|\phi_{i_A}\rangle - |\tilde{\phi}_{i_A}\rangle\Big) \langle \tilde{p}_{i_A}|\right) |\tilde{\psi}\rangle \end{aligned} \tag{1.9}$$

where ϕ_{i_A} are all-electron partial waves, and tilde and denotes pseudized variants, e.g. $\tilde{\phi}_{i_A}$ is the ith pseudo partial wave for the Ath atom.

The pseudo partial waves are intended to be smooth so they can be described with fewer grid points. The PAW cuttoff radius is adjusted to allow enough freedom to smooth the pseudo partial waves [24].

In practice, the partial waves form only a finite, incomplete basis and are chosen such that expansions of wavefunctions in partial waves quickly converge.

In this work, the projectors are zero outside of the PAW cutoff radius for the particular atom. The corrections $\Big(|\phi_i\rangle - |\tilde{\phi}_i\rangle\Big)$ are by construction also zero outside of the PAW cutoff radius. Therefore the PAW correction depends only on information inside the core regions and only affects the core regions.

The PAW correction is important when creating the photoelectron, since it is explicitly a function of the core wavefunction. Additionally, the PAW is important for the modeling the core-hole potential efficiently. The core-hole potential is only highly varying in the core region.

Chapter 2

LOCAL TIME-CORRELATION APPROACH FOR CALCULATIONS OF X-RAY SPECTRA

Originally published as Phys. Rev. B 86, 115107 [26],

by A. J. Lee, F. D. Vila, and J. J. Rehr.

We present a local time-correlation function method for real-time calculations of core level x-ray spectra (RTXS). The approach is implemented in a local orbital basis using a Crank-Nicolson time-evolution algorithm applied to an extension of the SIESTA code, together with projector augmented wave (PAW) atomic transition matrix elements. Our RTXS is formally equivalent to ΔSCF Fermi's golden rule calculations with a screened core-hole and an effective independent particle approximation. Illustrative calculations are presented for several molecular and condensed matter systems and found to be in good agreement with experiment. The method can also be advantageous compared to conventional frequency-space methods.

2.1 Introduction

We present an approach for real-time calculations of x-ray spectra (RTXS), including x-ray absorption (XAS) and emission (XES), based on local time-correlation functions. Formally such correlation functions form the starting point for the many-body theory of x-ray spectra, e.g., in the classic work of Nozières and De Dominicis (ND).[14] Calculations based on time-correlation functions can be advantageous both formally and for practical calculations of many physical properties.[27] They have recently been applied to problems ranging from non-linear optical response[2] to thermal vibrations.[28] Nevertheless, x-ray spectra for deep core-levels have traditionally been calculated in frequency space using Fermi's golden rule.[29, 3, 30, 31]

Calculations of time-dependent response have been of increasing interest, especially with the advent of high brightness pulsed x-ray sources.[32] One approach to such calculations is based on time-dependent density functional theory (TDDFT).[13, 33] Real-space, real-time implementations of TDDFT have been developed for both linear and non-linear optical response.[13, 2] However, these approaches are currently restricted to the UV-VIS range due to basis set limitations and the need for very short time-steps to treat the x-ray regime and very long simulation times to account for the valence response. The many-body formulation based on time-dependent Green's functions is particularly useful, e.g., to describe the x-ray edge singularity. [14, 34] However, calculations of XAS within the ND formalism require transient Green's functions and the response to the sudden creation and destruction of a core-hole, for which a number of approaches have been proposed.[35, 36, 37] Nevertheless, edge-singularity effects are most important in metallic systems near threshold, and are typically suppressed due to lifetime and other broadening effects.

For the above reasons, we restrict our attention in this paper to the simpler, limiting case of x-ray response in the presence of a static, adiabatically screened core-hole. The extension to dynamical response will be reserved for a subsequent paper. This initial step is interesting in its own right, since it facilitates comparison with frequency-domain calculations and is often a good approximation for molecular and non-metallic materials. In particular this limiting case is equivalent to Fermi's golden rule within a ΔSCF approximation in an effective, independent particle picture. For XAS this picture is referred to as the *final-state rule.*[38] Like Green's function approaches in frequency space,[39] the time-correlation function method is efficient, since it avoids the need for explicit sums over occupied or unoccupied states and depends only on local properties. Indeed the approaches are similar and can be related via time-Fourier transforms. Our approach is implemented using a real-time extension of the SIESTA code [2] with a Crank-Nicolson time-evolution operator,[40] and projector augmented wave (PAW) transition matrix elements.[41] This implementation results in a practical and generally applicable code that builds in full-potential electronic structure and self-consistent core-hole screening. Moreover, for the systems investigated, the code yields results in as good or better agreement with experiment than conventional frequency-space methods.

2.2 Formalism

2.2.1 Time-correlation function

Assuming that the core- and valence-electron states can be treated as independent, factorizable subspaces, our starting point is an expression for the core-level XAS $\mu(\omega)$ in terms of a local time-correlation function $\langle\psi_+(0)|\psi_+(t)\rangle$ defined below,

$$\mu(\omega) = \frac{1}{\pi}\,\mathrm{Re}\int_0^\infty dt\, e^{i\omega t} G_c(t)\langle\psi_+(0)|\psi_+(t)\rangle. \tag{2.1}$$

The time correlation function characterizes the response to x-ray excitation *via* an interaction Hamiltonian (e.g., the dipole interaction) from a given core-orbital $|c\rangle$ with energy ϵ_c. Here $G_c(t) = i\theta(t)\exp[i(\epsilon_c + i\Gamma)t]$ is the bare core-hole Green's function with core-hole lifetime Γ. The time-evolution of $|\psi_+(t)\rangle$ is governed by the single particle equation of motion[27]

$$i\frac{\partial|\psi_+\rangle}{\partial t} = \mathbf{H}'(t)|\psi_+(t)\rangle, \tag{2.2}$$

where $\mathbf{H}'(t)$ is the dynamic, final-state one-electron Hamiltonian in the presence of a core-hole in level $|c\rangle$. Here and elsewhere below, we use atomic units $e = \hbar = m = 1$, and a prime denotes the presence of a core-hole. For deep core-states the initial "seed state" $|\psi_+(0)\rangle$ created by the dipole interaction $d(x)\exp(i\omega t)$ in XAS is

$$|\psi_+(0)\rangle \equiv \mathcal{P}\,|\psi(0)\rangle = \mathcal{P}\,d(x)|c\rangle, \tag{2.3}$$

which is localized with respect to the absorption site. Here $\mathcal{P} = \mathbf{1} - \Sigma_k^{occ}|k\rangle\langle k|$ is the projector onto the sub-space of unoccupied valence and continuum states $|k\rangle$, i.e., energy eigenstates of the ground state Hamiltonian above the Fermi energy E_F. This projection reflects the fact that transitions to occupied states are excluded in the full many-body treatment of XAS. For an inhomogeneous system, one must also average over the chemical shifts for all core-state energy levels. A typical time correlation function for the dipole response for the C K-edge XES of benzene is shown in Fig. 2.4.

The projector $\mathcal{P}$ can be handled in several ways: i) One way is to construct $\mathcal{P} = \mathbf{1} - \Sigma_k^{occ}|k\rangle\langle k|$ explicitly from the initial occupied Kohn-Sham states $|k\rangle$. ii) A simpler alternative is to start with an unprojected seed state $|\psi(0)\rangle = d|c\rangle$. With this latter choice the restriction to unoccupied states is added *ex post facto* through Fourier filtering and the introduction of an *ad hoc* factor $\theta(E - E_F)$ in Eq. (2.1), where $E = \omega + \epsilon_c$. In practice, the Fermi energy E_F is set at mid-gap between the occupied and unoccupied states. In this paper we have generally used this alternative approach ii). However, a potential drawback is that the seed state may contain rapidly oscillating energy states that require relatively short time-steps to treat accurately.

X-ray emission spectra (XES) can be calculated similarly from the correlation function $\langle\psi_-(0)|\psi_-(t)\rangle$ and a time-evolution similar to that in Eq. (2.2) governed by the initial state Hamiltonian $\mathbf{H}(t)$ (i.e., the *initial state rule*). Here the seed state is $|\psi_-(0)\rangle = \mathcal{P}_{occ}|\psi(0)\rangle$ i.e., with the projector $\mathcal{P}$ replaced by the projector $\mathcal{P}_{occ} = \Sigma_k^{occ}|k\rangle\langle k|$ onto occupied states below E_F. Unless otherwise specified we will focus below on the XAS case, with the understanding that the treatment for XES is similar apart from the treatment of the core-hole potential and projector $\mathcal{P}$.

A number of many-body effects can be incorporated in RTXS. For example, intrinsic losses from the dynamical response to the core-hole can be added subsequently *via* convolution with an additional broadening function given by the Fourier transform of the exponential $e^{C(t)}$, where the cumulant $C(t)$ can also be obtained from the transient Green's function.[14, 34] Final state lifetime effects due to extrinsic processes and interference effects lead to additional damping, which here are crudely represented as an additional exponential decay factor $e^{-\gamma t}$. Note that the core-hole lifetime Γ as well as the decay of the correlation function serve as natural convergence factors in the calculation of the XAS which limit the maximum time in the evaluation of Eq. (2.1). These effects will be considered in more detail in a subsequent paper.

To evaluate the time-correlation function, we use a fixed, local, non-orthogonal basis set $\phi_j(\vec{x}) \equiv |j\rangle$, as in the SIESTA code.[42] It is also convenient to define dual states $\langle\tilde{j}| = \Sigma_{j'} S^{-1}_{jj'}\langle j'|$, where $S_{jj'} = \langle j|j'\rangle$ is the overlap matrix. These states satisfy the orthogonality relations $\langle\tilde{j}|j'\rangle = \delta_{jj'}$, and are also well localized with respect to atomic sites to the extent the overlap matrix and its inverse are short-ranged. In this local orbital orbital basis, the time-evolved state $|\psi(t)\rangle$ can be expanded as

$$|\psi(t)\rangle = \sum_j |j\rangle c_j(t). \tag{2.4}$$

At $t = 0$ the coefficients $c_j(0) = M_{jc}$ are given by quasi-local transition-matrix elements

$$M_{jc} = \langle\tilde{j}|d|c\rangle = \sum_{j'} S^{-1}_{jj'}\langle j|d|c\rangle. \tag{2.5}$$

As noted above, the time-evolution of $|\psi(t)\rangle$ can be expressed in terms of the unitary time-evolution operator $U(t,0)$ such that $|\psi(t)\rangle = U(t,0)|\psi(0)\rangle$, where

$$U(t,0) = T\exp\left[-i\int_0^t dt\,\mathbf{H}'(t)\right], \tag{2.6}$$

and T is the time-ordering operator. Thus the time-correlation function can be calculated directly using the transition-matrix elements and the local matrix elements of $\mathbf{U}$

$$\langle\psi(0)|\psi(t)\rangle = \sum_{jj'}\langle c|d^\dagger|j\rangle U_{jj'}(t,0)\langle\tilde{j}'|d|c\rangle. \tag{2.7}$$

Calculations starting from $|\psi_+(0)\rangle$ or $|\psi_-(0)\rangle$ are similar, and make use of the same operator $U(t,0)$. Due to the local nature of the transition-matrix elements $\langle\tilde{j}|d|c\rangle$ for deep core-orbitals $|c\rangle$, the sums over orbitals in these basis-set expansions are limited to a small neighborhood of the core-site. Moreover, since the final state Hamiltonian is constant during the period of integration, the calculation of the time-evolution operator is highly efficient.

In our implementation for RTXS, the time evolution operator $U_{jj'}(t,t')$ is evaluated as a product over many small time-steps Δ using a Crank-Nicolson algorithm, i.e., $c_j(t+\Delta) = \sum_{j'} U_{jj'}(t+\Delta,t)c_{j'}(t)$, where (in matrix notation) the differential time-evolution operator is

$$\mathbf{U}(t+\Delta,t) = \frac{\mathbf{1} - i\mathbf{S}^{-1}\mathbf{H}'(\bar{t})\Delta/2}{\mathbf{1} + i\mathbf{S}^{-1}\mathbf{H}'(\bar{t})\Delta/2}, \tag{2.8}$$

and $\bar{t} = t + \Delta/2$. This approximation is manifestly unitary and also time-reversible to 2nd order in the time interval Δ, due to evaluating the operators at the interval midpoint $\bar{t}$. This prescription has been found to be stable for relatively long time intervals Δ. $\mathbf{H}'(t)$ is the

Hamiltonian of the final state evaluated in the local basis, which is independent of time over the region of integration. In XAS, a core-hole is created during the photoelectron excitation while the remaining electrons relax to provide a screening charge. Thus, in addition to the Hartree Hamiltonian h_H and final state self-energy Σ, $\mathbf{H}'(t)$ includes the screened core-hole potential v_{ch} with matrix elements $H'_{jj'} = \langle j|h_H + v_{ch} + \Sigma|j'\rangle$.

In practice, the core-hole effect is introduced by substituting the neutral pseudopotential of the absorbing atom, with one that matches the full core-hole potential for the core-state $|c\rangle$. The system is then relaxed self-consistently in SIESTA in the presence of the core-hole. This produces, in a single initialization calculation, a Hartree Hamiltonian including the Coulomb potential obtained from the core-hole relaxed density, and a local pseudocharge. The resulting Hamiltonian is used for the subsequent propagation. For XES simulations v_{ch} is not applicable, and the Hamiltonian matrix elements used are $H_{jj'} = \langle j|h_H + \Sigma|j'\rangle$. Although all matrix elements of $H'_{jj'}$ and $S_{jj'}$ are needed in the time evolution, only the local matrix elements $U_{jj'}(t, 0)$ for j and j' in the neighborhood of the core-orbital are needed in the calculation of $\mu(\omega)$. In practical RTXS calculations, SIESTA is used only to obtain the matrix elements of $\mathbf{H}'$ (or $\mathbf{H}$) and $\mathbf{S}$, the Fermi energy E_F and the basis functions $\phi_j(\vec{x})$ needed to construct the atomic matrix elements. The time-evolution operator matrix elements are calculated subsequently.

Physically, the Fourier transform of the time-correlation function can be interpreted as a local density of final, unoccupied electron states $\rho_+(\omega)$ defined for the state $|\psi_+\rangle$; i.e., the levels and amplitudes allowed by the transition operator in the presence of the core-hole,

$$\rho_+(\omega) = \frac{1}{\pi\|\psi_+\|^2}\,\mathrm{Im}\int_0^\infty dt\, e^{i\omega t}\langle\psi_+(0)|\psi_+(t)\rangle, \tag{2.9}$$

where $\|\psi_+\|^2 \equiv \langle\psi_+(0)|\psi_+(0)\rangle$ is the normalization constant. For example, for K-shell absorption, the state $|\psi_+(0)\rangle$ is a superposition of local atomic-like p-orbitals and $\rho_+(\omega)$ corresponds to the local final, unoccupied state p-DOS, projected onto those orbitals. Similarly the density $\rho_-(\omega)$ corresponds to the density of occupied states of the initial state Hamiltonian.

2.2.2 Equivalence to Fermi's golden rule

As noted in the introduction, the time-correlation approach discussed herein for dipole mediated transitions is equivalent to Fermi's golden rule within an effective independent particle picture and the ΔSCF approximation. To show this, one may evaluate the time correlation function formally in terms of the scattering eigenstates $|k'\rangle$ of H' calculated in the presence of a core-hole. By expanding in one-particle states and applying the projector $\mathcal{P}$ we obtain the conventional sum-over-states expression for the golden rule in the independent particle approximation

$$\mu(\omega) = \sum_{k'} |\langle c|d|k'\rangle|^2 \delta_\Gamma(E - \epsilon_{k'})\theta(E - E_F), \tag{2.10}$$

where $E = \omega + \epsilon_c$ and δ_Γ is a δ-like function of unit weight broadened by the core-hole lifetime Γ.

Alternatively one can demonstrate the equivalence from a spectral representation of the time-evolution operator. Given that the time-Fourier transform of $\mathbf{U}$ is proportional to the one particle Green's function $G'(E)$ for the final state, [cf. Eq. (2.9)] calculated (for XAS) in the presence of a core-hole, the XAS from a core level at energy ϵ_c is

$$\mu(\omega) = -\frac{1}{\pi}\,\mathrm{Im}\,\langle c|d^\dagger \mathcal{P}\, G'(E)\, \mathcal{P} d|c\rangle, \tag{2.11}$$

which agrees with the formalism in the real-space Green's function (RSGF) approach used, e.g., in the FEFF codes.[43] Here $G'(E) = [E - H' + i\Gamma]^{-1}$ is the retarded one particle Green's function at energy $E = \omega + \epsilon_c$, H' is the one-electron Hamiltonian of the final quasi-particle state including a screened core-hole and a final state self-energy Σ, and again $\mathcal{P}$ is the projector onto unoccupied states above the Fermi energy. Finally, in the limiting case of an empty conduction band described by Wannier orbitals, this result for $\mu(\omega)$ reduces to

$$\mu(\omega) = |M_{0c}|^2 \rho'_{00}(E), \tag{2.12}$$

in agreement with Eq. (41) of Ref. [35]. Here $E = \epsilon_c + \omega$ and $\rho'_{00}(E)$ is the local density of states at the absorption site 0 in the presence of a core-hole.

2.2.3 Local Projection

In practice it is computationally useful to simplify the above by projecting the initial state onto basis functions centered on the excited atom, when the initial state has a small overlap with other basis functions. For the systems studied in this paper, this produces good agreement with other theories and experiment as long as the projector is applied to the energy eigenvectors as well. Given a complete set of eigenvectors $\{|k\rangle\}$ with eigenvalues E_k so that $|k\rangle = \sum_j a_{kj}|j\rangle$, we may expand the seed state as

$$|\psi(0)\rangle = \sum_j c_j(0)|j\rangle = \sum_{k,ij} a^*_{ki} S_{ij} c_j(0)|k\rangle, \tag{2.13}$$

and the absorption/emission intensity for a given eigenvalue E_k as

$$W_k = |\langle k|\psi(0)\rangle|^2 = \sum_{ij} |a^*_{ki} S_{ij} c_j(0)|^2. \tag{2.14}$$

Due to the highly localized nature of the core states, the seed state can be approximated as a local initial state $\mathcal{P}_A|\psi(0)\rangle$, where $\mathcal{P}_A$ projects onto the subset of basis set vectors centered on the excited atom A,

$$\mathcal{P}_A = \sum_{i \in A} |i\rangle\langle\tilde{i}|. \tag{2.15}$$

Within this approximation, the local spectral weight is

$$W^A_k = \left|\langle k|\mathcal{P}^\dagger_A \mathcal{P}_A|\psi(0)\rangle\right|^2 = \sum_{ij \in A} |a^*_{ki} S_{ij} c_j(0)|^2, \tag{2.16}$$

and the time-correlation function $C(t) = \langle\psi(0)|\psi(t)\rangle$ can be approximated as a local quantity

$$C_A(t) = \langle\psi_A(0)|\psi_A(t)\rangle, \tag{2.17}$$

where

$$|\psi_A(t)\rangle = \mathbf{U}(t,0)\mathcal{P}^\dagger_A \mathcal{P}_A|\psi(0)\rangle. \tag{2.18}$$

Although this simplification provides only minor performance improvements, it highlights the local nature of the process where a photo-electron state is created.

2.2.4 Transition Matrix Elements

To obtain the seed state for the time correlation formalism, we must first compute the transition matrix elements M_{jc} in Eq. (2.5). These matrix elements involve a core state $|c\rangle$, a local basis function $|j\rangle$, and the dipole interaction $d(x)$ (in position-representation). Since the SIESTA $|j\rangle$ basis functions are atomic orbitals of the pseudoatom, the core regions must be reconstructed to find the correct matrix elements.[25, 44] For this purpose we use the Projector Augmented Wave (PAW) engine from the core-level spectroscopy code OCEAN. [45]

Given an arbitrary all-electron wavefunction $|\psi_{ae}\rangle$ and its associated pseudowave $|\psi_{ps}\rangle$, the PAW reconstruction transformation operator $\mathcal{T}$ is defined as

$$|\psi_{ae}\rangle = \mathcal{T}|\psi_{ps}\rangle. \tag{2.19}$$

Thus, the pseudowave $\{|\phi^i_{ps}\rangle\}$ and all-electron basis orbitals $\{|\phi^i_{ae}\rangle\}$ satisfy the relation

$$|\phi^i_{ae}\rangle = \mathcal{T}|\phi^i_{ps}\rangle. \tag{2.20}$$

We may therefore define a projector basis set $\{\langle p^i|\}$ that satisfies $\langle p^i|\phi^j_{ps}\rangle = \delta_{ij}$ inside some cutoff r_c, to be specified below; $\{|\phi^i_{ps}\rangle\}$, $\{|\phi^i_{ae}\rangle\}$, and $\{\langle p^i|\}$ are set to zero outside r_c. This cutoff is chosen so that it satisfies OCEAN's requirement that it be large enough that the pseudo- and all-electron wavefunctions agree beyond it. Furthermore, we require r_c to be greater than the SIESTA pseudowavefunction cutoff, beyond which the basis functions are set to zero.

The PAW reconstruction operator is given formally by

$$\mathcal{T} = 1 + (|\phi^i_{ae}\rangle - |\phi^i_{ps}\rangle)\langle p^i|. \tag{2.21}$$

Since $|c\rangle$ is well localized within r_c, the reconstruction operator simplifies to $\mathcal{T} = |\phi^i_{ae}\rangle\langle p^i|$. Then the matrix elements may be expressed as $\langle\tilde{i}|\mathcal{T}^\dagger d|c\rangle$, resulting in the following expression for the seed state:

$$|\psi_{ps}(0)\rangle = \sum_{i,j} |i\rangle\langle\tilde{i}|p^j\rangle\langle\phi^j_{ae}|d|c\rangle. \tag{2.22}$$

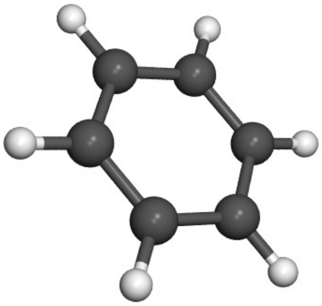

Figure 2.1: Gas phase structure of benzene (C_6H_6) used in the RTXS and StoBe simulations,[46] where C is dark grey and H is white.

It should be noted that the calculation of $\langle\tilde{i}|p^j\rangle$ is possible because we choose r_c greater than the $|i\rangle$ cutoff. Moreover, the core reconstruction calculation for XAS is done without a core-hole, consistent with the approach described in Section 2.2.1.

2.3 Computational Details

2.3.1 Model Systems

To demonstrate the versatility of the RTXS time-correlation approach, we present illustrative calculations for three representative systems: benzene (C_6H_6), trinitrotoluene (TNT, $C_7H_5N_3O_6$) and diamond. Benzene (Fig. 2.1) is simulated in its gas phase conformation.[46] For TNT we use one of the symmetry-inequivalent molecules in its crystalline structure (Fig. 2.2).[47] We have previously shown[48] that this yields well converged results compared to experiment. Diamond is modeled using a $C_{47}H_{60}$ hydrogen-capped cluster, shown in Fig. 2.3, generated using the experimental lattice constant of 3.5668 Å and including 5 carbon shells around a central absorber. For comparison, diamond calculations were also performed using periodic boundary conditions (PBC) on a 2×2×2 supercell of the conventional 8-atom orthogonal cell with the same lattice constant.

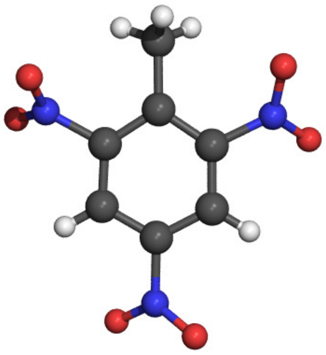

Figure 2.2: Structure of a single symmetry-inequivalent molecule of trinitrotoluene (TNT, $C_7H_5N_3O_6$) used in the RTXS, StoBe and FEFF simulations, where C is dark grey, H is white, O is red (light grey) and N is blue (medium grey).

2.3.2 RTXS

The RTXS calculations use a SIESTA triple-ζ basis set with two d-polarization functions on the C, N and O atoms and two p-polarization functions on the H atoms (TZDP). The cutoff radii are set using an energy shift[42] of 1 meV, which results in typical cutoffs of about 5 to 10 Bohr. The SIESTA calculations also use an auxiliary real-space grid with an equivalent planewave cutoff of 150 Ry. This choice of polarization functions and cutoff radii ensures a good representation of all the valence occupied states, as well as the valence unoccupied states up to about 30 eV above threshold. For consistency with the StoBe simulations described below, all RTXS simulations used the PBE[21] exchange-correlation functional. Typical total RTXS simulations were carried out to $t_{max} =$ 5-15 fs, long enough that modes with frequencies above 0.5-1 eV do not appear as non-periodic trends. The typical time steps were 0.01 fs which accommodate frequencies as high as 50 eV. The final spectra are shifted to fit experimental peak positions and broadened to match the experimental broadening. To do this, first an exponential damping is added to the raw correlation such that the correlation is below 0.01 at the end of the time series; this yields an initial Lorentzian broadening. Second, Gaussian broadening is added to the Fourier transformed spectra to match experimental

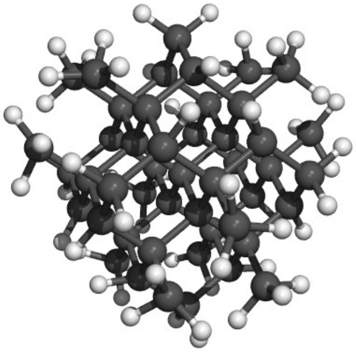

Figure 2.3: Structure of the hydrogen-capped diamond cluster ($C_{47}H_{60}$) used in the RTXS, StoBe and FEFF simulations, where C is dark grey and H is white. The cluster is generated using the experimental structure of diamond with lattice constant 3.5668 Å, and includes 5 carbon shells around the absorber.

broadening. For XAS, the Gaussian broadening has a standard deviation $\sigma(E)$ which varies with energy:

$$\sigma(E) = \begin{cases} \sigma_{min} & E < E_1, \\ \sigma_{min} + \gamma(E - E_1) & E_1 \leq E \leq E_2, \\ \sigma_{min} + \gamma(E_2 - E_1) & E > E_2, \end{cases} \tag{2.23}$$

where σ_{min}, E_1, E_2, and γ depend on the system. For XES, the Gaussian broadening is constant. This approach is analogous to that implemented in StoBe.[3, 5]

We use non-relativistic, kinetic-energy optimized, norm-conserving pseudopotentials, with and without a core-hole. These are generated with OPIUM[49], using the PBE exchange-correlation functional. The neutral and core-hole pseudopotential cutoff radii are equal, except as needed by the introduction of the core-hole. In the systems simulated here only C and N atoms are excited. For the N pseudopotential, the reference configuration is $1s^2\ 2s^2\ 2p^3$ and for C it is $1s^2\ 2s^2\ 2p^2$ or $1s^1\ 2s^2\ 2p^2$, depending on the presence of a core-hole. For carbon without a core-hole, the core cutoff radii are 1.40 Bohr for all l-channels. For carbon with a core-hole, the cutoff radii are 1.25 Bohr for all l-channels, except the $2p$ states, which have a cutoff radius of 1.20 Bohr. For nitrogen without a core-hole, the cutoff radii are 1.25 Bohr for all l-channels.

2.3.3 StoBe

For comparison, StoBe-deMon simulations were carried out using the IGLO-III[50] basis set for the absorbing atoms, while the (311/211) ECP StoBe basis set[51] was used for all other atoms except H which used the 6-311+G set.[52] The Coulomb and exchange correlation potentials were fitted and expanded over auxiliary basis sets with (NC(s), NC(spd); NXC(s), NXC(spd)) *s* and *spd*-type functions. Auxiliary sets of (5,2;5,2) quality were used for the C, N and O atoms, and of (3,1;3,1) quality for the H atoms. All StoBe-deMon calculations used the PBE[21] exchange-correlation functional. The XAS[3] and XES[5] StoBe-deMon calculations use the "frozen-orbital" approximation with Kohn-Sham single-particle orbitals. While the XES simulations use ground-state orbitals, XAS results were obtained using the Transition Potential approximation, a simplification of the Slater's Transition State core-hole approximation, in which the core spin-orbital is populated with half an electron and the excited half electron is neglected. This allows obtaining all excited states from one diagonalization. In contrast it should be noted that the RTXS simulations use a full self-consistently screened core-hole. For comparison, we also performed test StoBe calculations using a full core-hole. For the systems studied here we find that, apart from an energy shift, the half core-hole and full core-hole spectra are quite similar.

2.3.4 FEFF

Additional comparisons were carried out using version 9 of the FEFF code.[43] This approach is based on the RSGF formalism which includes approximate calculations of many-body effects including inelastic losses and Debye-Waller factors. For XAS the final state is calculated in the presence of a statically screened core-hole, i.e. the final state rule (FSR); for XES the calculations are done without a core-hole. In many respects the RSGF approach in FEFF is the frequency-space analog of the RTXS approach discussed in this paper. However, FEFF uses a basis of relativistic, angular-momentum scattering states $|L, \mathbf{R}\rangle$ to describe electronic states. Therefore, it is expected to be more accurate than

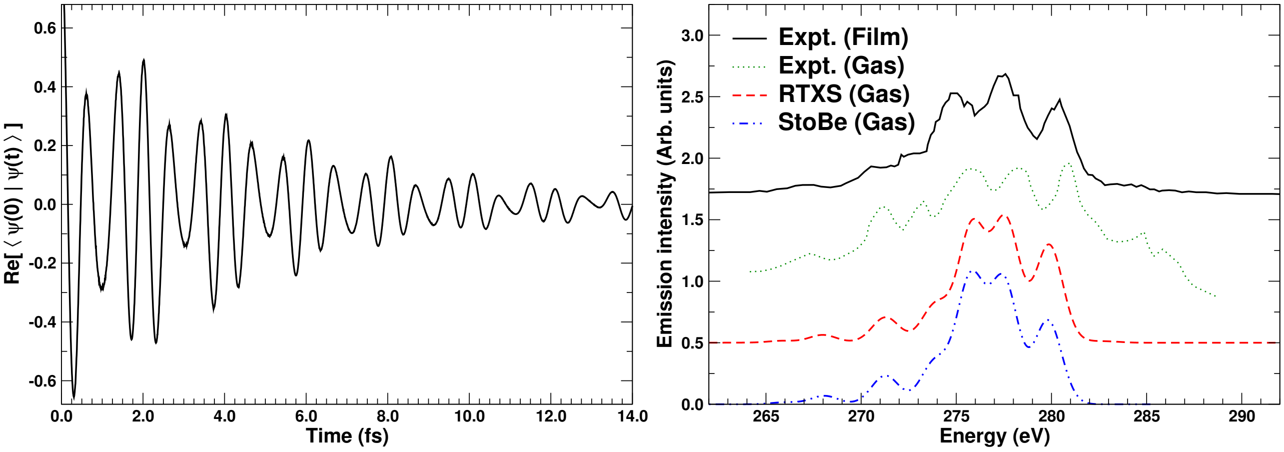

Figure 2.4: Left: Real part of the Fourier filtered RTXS time correlation function for the C K-edge XES of benzene. Right: Real-time (RTXS) corresponding to the time correlation function shown to the left) and StoBe simulations of the C Kα XES of benzene gas (C_6H_6) compared to experiment in film[53] and gas phase[54] conditions. The gas phase measurement corresponds to electron rather than photon excitation.

either RTXS and StoBe at energies high above the edge. However, FEFF's use of spherical muffin-tin potentials makes the code less accurate near the edge. The core-hole potential is obtained using a self-consistent Dirac-Fock calculation for an atom with an atomic configuration containing a hole in a given level, e.g., $1s$ for the K-shell calculations presented here. Here we have used the FEFF9 code with 5 Å clusters for the generation of the self-consistent muffin-tin potentials and 9 Å clusters for the calculations of the full multiple scattering XAS (or XES).

2.4 Results

2.4.1 Benzene

Given its structural and electronic simplicity, benzene is a good system to test our approach. The XES autocorrelation function, shown in Fig. 2.4, has a relatively simple structure involving a few timescales. The associated spectrum (also in Fig. 2.4), is domi-

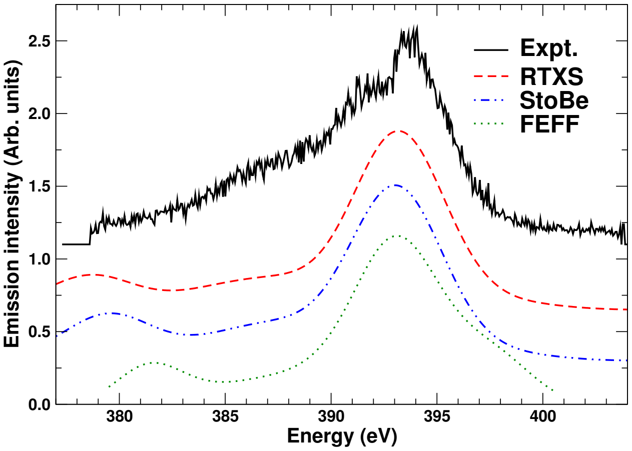

Figure 2.5: Real-time (RTXS), StoBe and FEFF simulations of the N Kα XES of trinitrotoluene (TNT, $C_7H_5N_3O_6$) compared to experiment measured in a film.[48]

nated by three high intensity peaks 4, 6 and 8 eV below threshold, and three low intensity ones at lower energies. The width σ is set to 0.7 eV and the spectrum is shifted by 286.0 eV to match experiment. The high intensity peaks are associated with clearly visible 0.4-0.6 fs periods in the autocorrelation function, and are due to emission from orbitals with symmetry $1e_{1g}$ (279.8 eV), $3e_{2g}$ (277.5 eV), and $1b_{2u}/3e_{1u}$ (276.0 eV).

For comparison, Fig. 2.4 also shows experimental and StoBe results. The agreement with StoBe is quite good and serves as a validation of our methodology. The most noticeable difference arises for the two most intense peaks. The small difference in intensity ratio is due mostly to the projection onto local basis orbitals from the initial state. Both RTXS and StoBe calculations show good overall agreement with experiment, and slightly underestimate the splittings in the triplet of intense peaks.

2.4.2 Trinitrotoluene

Trinitrotoluene (TNT) poses a more significant challenge to the theory due to its complex electronic structure and multiple absorbing N atoms.[48] As for C_6H_6, we find very good agreement between RTXS and StoBe (Fig. 2.5). For RTXS, σ was set to 2.0 eV and the spectrum shifted by 407.0 eV to match the K-shell experiment. Moreover, we also find fairly

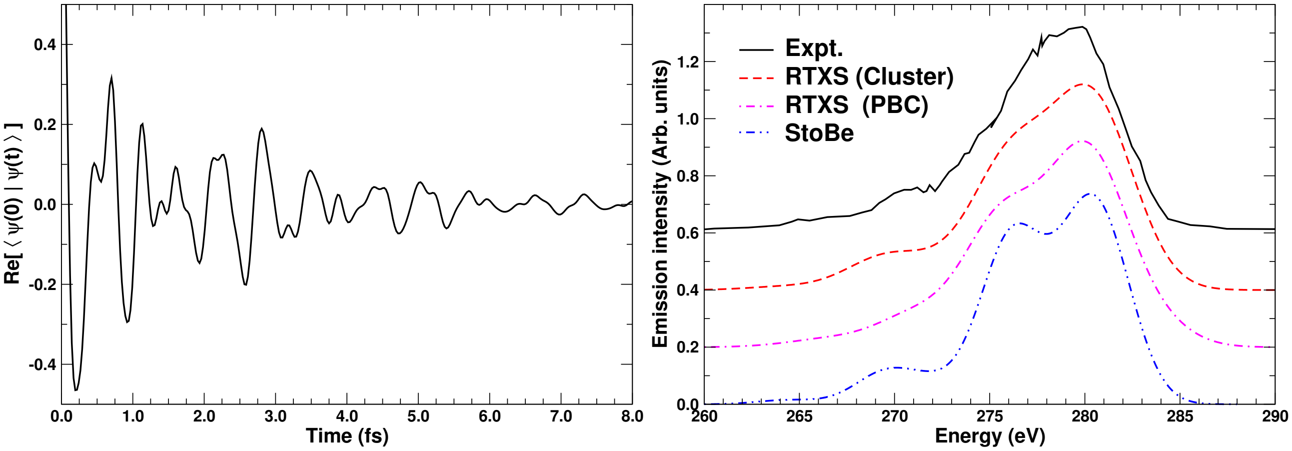

Figure 2.6: Left: Real part of the Fourier filtered RTXS time correlation function for the C K-edge XES of diamond (simulated using a $C_{47}H_{60}$ cluster). Right: Real-time (RTXS, corresponding to the time correlation function shown to the left) and StoBe simulations of the C Kα XES of diamond compared to experiment.[55] The RTXS calculations used either a $C_{47}H_{60}$ cluster or a 2×2×2 supercell of the conventional 8-atom orthogonal cell with periodic boundary conditions (PBC).

good agreement with the RSGF approach in FEFF; however, the discrepancies are likely due to the use of spherical muffin-tin potentials in FEFF. As discussed in Ref. [48], the lower intensity with respect to experiment in the 385-390 eV region is due to an underestimation of the transition intensities associated with σ_{NC} bonds. In general, intensities associated with σ bonds are more affected by vibrational distortions (not included in our simulations) than π bonds.

2.4.3 Diamond

As a third example we present results for diamond, a relatively simple yet challenging insulating crystalline solid. Fig. 2.6 shows the RTXS XES results in comparison with StoBe calculations and experimental measurement. For RTXS, σ was set to 1.9 eV and the spectrum is shifted by 285.6 eV to match experiment. As in the previous examples, the agreement between RTXS and StoBe is fairly good despite the slightly different broadening schemes. The

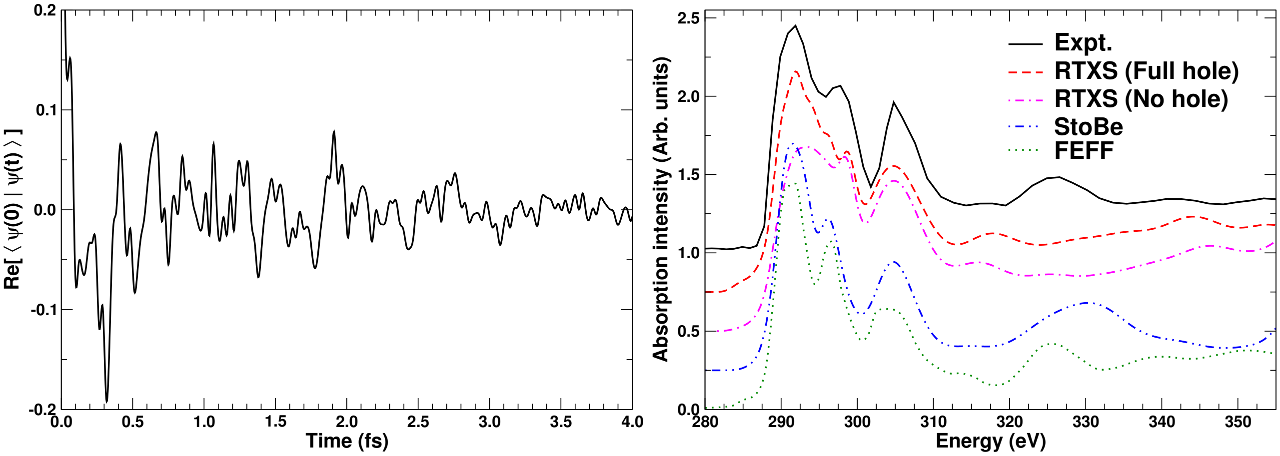

Figure 2.7: Left: Real part of the Fourier filtered RTXS time correlation function for the C K-edge XAS of diamond (simulated using a $C_{47}H_{60}$ cluster). Right: Real-time (RTXS, corresponding to the time correlation function shown to the left), StoBe and FEFF simulations of this system versus experiment.[56] The RTXS XAS is calculated with and without a core-hole, while StoBe uses a half core-hole prescription.

RTXS results are also in very good agreement with experiment, accounting for the broad 275-283 eV feature, and the small peak at 270 eV. In RTXS, the broad feature is composed of two peaks at 279.8 eV and 276.9 eV, with almost equal intensity, and a less intense peak at 274.7 eV. The two latter peaks form the broad shoulder at about 275 eV. The overall width of this feature, about 7.9 eV, corresponds to the occupied valence bandwidth and is in good agreement with experimental width of 7.2eV. The broad feature at 270 eV is composed of several low intensity peaks. Fig. 2.6 also shows the real-time autocorrelation function associated with the RTXS XES. Given the number of states involved in the XES, it is not surprising that the correlation function is quite complex, exhibiting a variety of timescales. Most noticeable are periods of about 0.5 and 0.4 fs, associated with the broad 275-283 eV feature, overlaid with shorter (about 0.2 fs) oscillations associated with the broad feature at 270 eV.

Our RTXS implementation is currently able to compute XES spectra using periodic boundary conditions (PBC), i.e., with the initial state Hamiltonian without a core-hole.

Fig. 2.6 shows a comparison between the $C_{47}H_{60}$ cluster model and PBC model, where the PBC calculation used a 2×2×2 supercell of the conventional 8-atom orthogonal cell. Both methods give similar results, with the cluster approach being closer to experiment, in particular in the 270 eV region.

Fig. 2.7 presents the XAS spectra of diamond computed with RTXS, StoBe and FEFF, compared to experiment. The RTXS spectra uses broadening parameters $\sigma_{min} = 0.8$ eV, $E_1 = 297.9$ eV, $E_2 = 302.9$ eV, and $\gamma = 0.4$ eV, using the notation in Eq. (2.23), and a shift of 285.7 eV to match the energies of the experimental peaks. In the near-edge region (285-310 eV), RTXS is in very good agreement with experiment, showing better splittings and relative intensities at 292 and 298 eV than either FEFF and StoBe. RTXS also shows very good agreement in the overall width of the unoccupied valence band, with a predicted width of 11 eV *vs* 11.5 eV observed in the experiment. In the edge region FEFF has limitations originating from the use of spherical potentials that hinder its ability to represent highly directional bonds. At higher energies (i.e., above 310 eV), RTXS yields worse agreement than either FEFF or StoBe. This is likely due to the limitations in the local basis sets - local numerical atomic orbitals for SIESTA and Gaussian-type orbitals for StoBe - which only provide a limited representation of the delocalized states in the continuum. Exploratory calculations show that with the present basis set, RTXS results begin to exhibit variations due to the quality of the basis set 30 eV above threshold. On the other hand FEFF provides the broadest overall agreement with experiment due to the superior performance of the RSGF approach at high energies. Fig. 2.7 also shows the associated autocorrelation function, which is significantly more complicated than the XES one. Given that the spectrum is composed of a large number of states, it is difficult to observe any dominant timescales.

As described in Section 2.2.1, XAS spectra present an additional challenge with respect to XES in that an adequate treatment the screened core-hole is required. In addition, it appears that the treatment of core-hole screening is responsible for much of the difference in diamond absorption spectra between StoBe and RTXS. Therefore it is interesting to explore the effect of ignoring the core-hole in the RTXS calculations. As shown in Fig. 2.7, we find that the core-hole has a noticeable effect near the edge, increasing the intensity and narrowing the width of the feature associated with the σ bonds at 292 eV. This reflects the large charge density relaxation and consequent excitonic enhancement induced by the attractive core-hole potential on the bond network surrounding the absorber. At present our RTXS implementation is limited to the no core-hole or fully screened (i.e., with SCF-DFT screening) core-hole approximations. More flexible core-hole treatments, e.g., using partial core charging, would allow better comparisons with other methods such as the half core-hole used in StoBe.

2.5 Conclusions

We have introduced a real-time approach (RTXS) for the calculation of XAS and XES based on time-correlation functions. The approach is equivalent to ΔSCF Fermi's golden rule calculations. The spectra are calculated from the Fourier transform of the autocorrelation function of the time-evolving wavefunction, together with the core-hole Green's function. The method is implemented as an extension of our real-time time-dependent density functional SIESTA code, and includes PAW transition matrix elements. We have compared RTXS calculations of XAS and XES with spectra from experiment, StoBe and FEFF. RTXS and StoBe produce similar emission spectra, with RTXS slightly closer to experiment in the case of diamond. In contrast, notable differences are found between RTXS and StoBe for XAS. In the case of diamond, RTXS models the near-edge XAS region more realistically than either FEFF or StoBe. The improvement compared to FEFF is likely due to the inclusion of non-spherical potentials, while differences with StoBe are probably due to the treatment of core-hole screening.

We thank G. Bertsch, J. Kas, R. Markiewicz, D. Prendergast, A. Rubio, R. Santra, and J. T. Vinson for discussions and insights. This work was initiated at a KITP program on X-ray Frontiers, and was supported in part by NSF CDI Grant PHY-0835543.

2.6 Addendum: comparison of core-hole effects with GPAW

Due to difficulties of using PAW matrix elements with SIESTA, we changed the DFT/TDDFT engine to GPAW after the publication which constitues the main parts of this chapter. GPAW contains the PAW matrix elements natively, and the code is better tested than the our implementation which attempts to insert PAW matrix elements from OCEAN into SIESTA. Core-hole comparisons with the GPAW engine show similar effects to those explore with SIESTA.

For example, for a 48 carbon diamond cluster capped with hydrogen atoms, we compare a full core-hole (final-state rule) calculation and half core-hole (transition-state rule) calculation with with our collaborators Sato and Yabana's [57] TDDFT using method of continuous fractions, and experiment[1].

We find that having a full core-hole overestimates the excitonic effects in the near edge region. If we adjust the strength to half core-hole, the near edge peak decreases in intensity and and becomes closer to experiment. This implies that perhaps studying the dynamics of the core-hole screening might elucidate the discrepancy with experiment.

Our close agreement with Sato's calculations implies that the main features of the calculated spectra are likely consistent across implementations.

---

[1] The core holes in the RTXS calculations are modeled within the PAW setups.

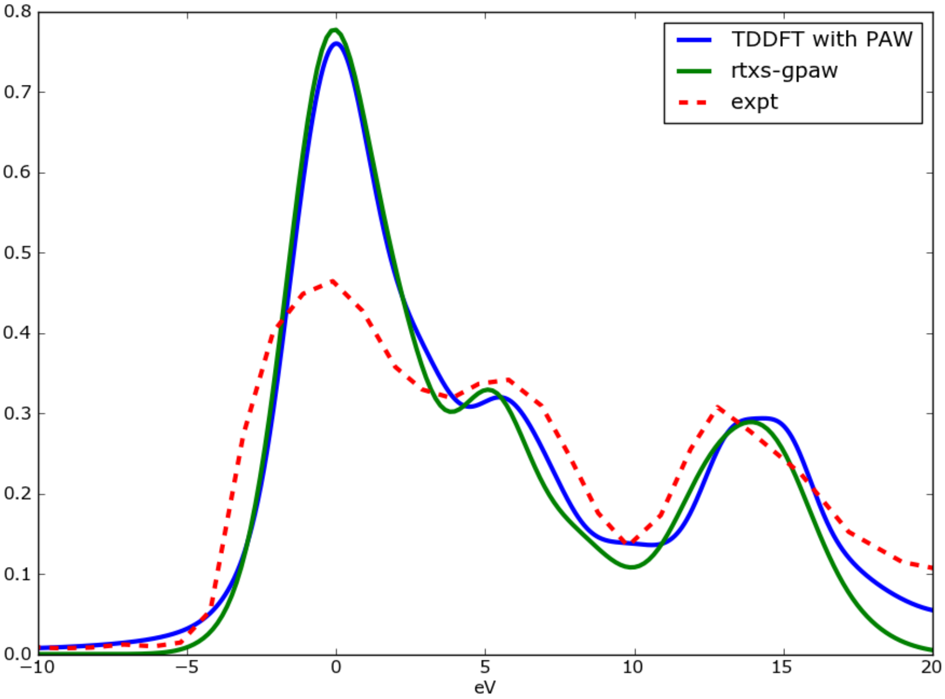

Figure 2.8: Diamond XAS with full core hole compared with TDDFT and experiment.

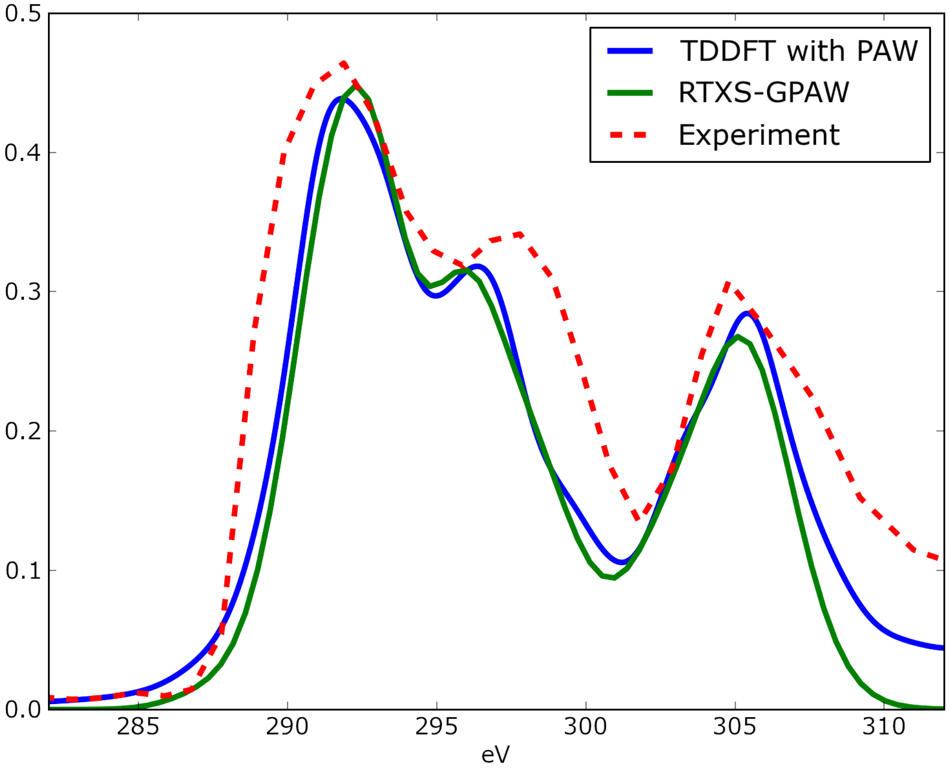

Figure 2.9: Diamond XAS with half core hole compared with TDDFT and experiment.

Chapter 3

TIME-DEPENDENT MEAN-FIELD THEORY FOR X-RAY NEAR-EDGE

Originally published as Phys. Rev. B 89, 075135 [58],

by G. F. Bertsch and A. J. Lee.

We derive equations of motion for calculating the near-edge X-ray absorption spectrum in molecules and condensed matter, based on a two-determinant approximation and Dirac's variational principle. The theory provides an exact solution for the linear response when the Hamiltonian or energy functional has only diagonal interactions in some basis. We numerically solve the equations to compare with the Mahan-Nozières-DeDominicis theory of the edge singularity in metallic conductors. Our extracted power-law exponents are similar to those of the analytic theory, but are not in quantitative agreement. The calculational method can be readily generalized to treat Kohn-Sham Hamiltonians with electron-electron interactions derived from correlation-exchange potentials.

3.1 Introduction

Time-dependent density functional theory (TDDFT) has proven to be a very useful tool for calculating the linear response of molecules and condensed matter systems. The overall features of the dielectric function are reproduced quite well, and the agreement at zero frequency in insulators is often at the few percent level. It also describes the plasmon peaks in the UV absorption spectrum and the corresponding energy loss spectrum in inelastic electron scattering.

The good experience in TDDFT in the optical regime encourages its application to

X-ray absorption, which has a rich near-edge structure that is only partially described by single-electron physics. Indeed, some aspects of the X-ray response are accessible to TDDFT[59, 60, 61, 62]. However, other aspects, particularly the dynamics of core-hole relaxation, are beyond the scope of the theory. This is because the fundamental assumption that the wave function be represented by a single Slater determinant is too restrictive when the core orbital is part of that determinant. The single-determinant theory can describe correlations between the core hole and the valence electron but not correlation effects within the valence space. To overcome this deficiency, we propose here a theory based on two separate Slater determinants, one for the initial and another for the final state. We derive the equations of motion in Sect. II below. We refer the reader to Ref. [63] for an review of the foundations of TDDFT and its recent extensions. In Sect. III following we apply our extension to the well-known Mahan-Nozières-De-Dominicis (MND) Hamiltonian. A comprehensive discussion of analytic and numerical methods to solve it is given in the review by Ohtaka and Tanabe [64]. The equations we solve numerically are exact for the MND Hamiltonian. We will argue that they are much easier than other methods to apply to DFT functionals which contain electron-electron interactions.

We note that a multicomponent TDDFT has already been derived as a generalization of the Runge-Gross theorem[65, 66]. It can be motivated as follows[67]. The ansatz permits a closer approximation to the physical starting wave function, and thus the accompanying density functional is then likely to be amenable to a simpler approximation. However, the extensions derived from the Runge-Gross theorem are typically based on a representation by particle-hole excitations of a single determinant[68]. Our derivation and equations of motion are different, resembling more the multi-determinant theory of nuclear excitations proposed in Ref. [69]. There is no underlying functional in our treatment here, although the equations are motivated by TDDFT. Each Slater determinant has its own density and evolves with the Kohn-Sham equation based on that density.

The final time-dependent equation that we solve numerically is Eq. (3.15) below; the response is evaluated using Eqs. (3.13) and (3.16).

3.2 The two-determinant approximation

We derive equations of motion from Dirac's variational principle

$$\delta \int dt \left\langle \Psi(t) \middle| i\frac{d}{dt} - H \middle| \Psi(t) \right\rangle = 0, \tag{3.1}$$

varying the wave function $|\Psi\rangle$ in the space of Slater determinants. The resulting time-dependent Kohn-Sham (KS) equations are then solved for the time-dependent wave function $|\Psi(t)\rangle$. For discussion of the action principle in the context of TDDFT, see Ref. [70, 71].

The linear response to an operator $\mathcal{O}$ is obtained from the time-dependent correlator $\langle[\mathcal{O}(t), \mathcal{O}(0)]\rangle/i$ calculated from

$$R(t) = \lim_{\lambda\to 0} \frac{1}{\lambda} \langle \Psi_\lambda(t)|\mathcal{O}|\Psi_\lambda(t)\rangle. \tag{3.2}$$

Here the initial state has been prepared by applying an impulsive field $V(r,t) = \lambda\mathcal{O}\delta(t)$ to the KS ground state $|\Psi_g\rangle$. In linear order, this modifies the initial wave function to

$$|\Psi_\lambda(0_+)\rangle = (1 - i\lambda\mathcal{O})|\Psi_g\rangle. \tag{3.3}$$

The resulting wave function is evolved by KS equations to determine the matrix element in Eq. (2). The connection of Eq. (2) to the more familiar frequency-dependent response $S(\omega)$ is given by

$$S(\omega) \equiv \sum_f \langle f|\mathcal{O}|0\rangle^2 \delta(E_f - \omega) = \frac{1}{\pi}\int_0^\infty dt R(t) \sin\omega t. \tag{3.4}$$

Since λ is small in Eq. (3.2), the evolved wave function is still largely in the ground state with only a small amplitude of excited states. This is fatal for calculating effects of the core hole excitation such as the relaxation of the valence wave function in the presence of the core hole. By considering separate determinants for the components of the wave function with and without the core electron excitation, the correlations associated with valence electrons can be treated as well as they are in the optical response. There is no danger of violating the Fermi statistics because the two components of the wave function are necessarily orthogonal.

Our starting point is the following ansatz for the variational wave function,

$$|\Psi\rangle = a_g c_c^\dagger |\Psi_{vg}\rangle + a_c|\Psi_c\rangle \tag{3.5}$$

where N_e is the number of active electrons in addition to the core electron. Here $|\Psi_{vg}\rangle = \prod_{\alpha}^{N_e} c^\dagger_\alpha|\rangle$ is the Slater determinant of the valence electrons in a state with the core electron in its ground state orbital. Correspondingly, $|\Psi_c\rangle = \prod_{\beta}^{N_e+1} c^\dagger_\beta|\rangle$ is the Slater determinant for a state with the excited core electron in the valence band. The two sets of valence-band orbitals are expressed in terms of the valence-band basis states i as $c^\dagger_\alpha = \sum a_{\alpha i} c^\dagger_i$ and $c^\dagger_\beta = \sum a_{\beta i} c^\dagger_i$ where $a_{\alpha i}$ and $a_{\beta i}$ are time-dependent amplitudes. We may choose these expansion coefficients to satisfy the conditions $\sum_i a^*_{\alpha i} a_{\alpha' i} = \delta_{\alpha\alpha'}$, etc. The amplitudes of the two Slater determinants (SD's), $a_g(t)$ and $a_c(t)$ will determine the mixing of the two determinants. They satisfy the normalization condition $|a_g|^2 + |a_c|^2 = 1$.

The MND Hamiltonian has the form

$$\hat{H} = \hat{H}_v(c^\dagger_i, c_i) + \hat{H}_c(c^\dagger_i, c_i) c_c c^\dagger_c. \tag{3.6}$$

The first term is the valence Hamiltonian to be constructed from the corresponding Kohn-Sham density functional. The second term adds the excitation energy of the core hole as well as its field acting on the valence electrons.

The variation in Eq. (1) is to be carried out with respect to changes in the wave function $|\Psi\rangle$ that preserve its character as a sum of two SD's. In the single-determinant theory, one takes the variational derivatives of $|\Psi\rangle$ with respect to $a_{\alpha,i}$ treating them as independent variables. This results in the usual time-dependent Kohn-Sham (KS) with the single-particle Hamiltonian given by

$$\hat{H}_{KS} = \sum_{i,j} \langle\Psi| \frac{\delta^2 \hat{H}_v}{\delta c^\dagger_i \delta c_j} |\Psi\rangle c^\dagger_i s_{ij} c_j \tag{3.7}$$

where $s_{ij} = \pm 1$ is a phase factor depending on the ordering of the operators in $\hat{H}_v$. However, as a consequence of the overcompleteness of the variables, the overall phase of the time-dependent KS wave function no longer has any physical meaning. For example, if the orbitals are eigenstates of the KS Hamiltonian, the overall phase is $\exp(-i \sum_n^{N_e} \epsilon_n t)$ where ε_n are the KS eigenvalues. The correct phase is $\exp(-i\langle\Psi|H|\Psi\rangle t)$; the two are only equal in the absence of electron-electron interactions. This phase plays no role in the single-determinant theory, but with two determinants it is crucial to have correct relative phases.

The proper procedure to apply Eq. (1) is to require that the wave function variations in

$$\left\langle \delta\Psi \middle| i\frac{d}{dt} - \hat{H} \middle| \Psi(t) \right\rangle = 0 \tag{3.8}$$

are independent of each other. An orthogonal (and thus independent) set of wave function variations may be defined by making use of Thouless's representation[72] of the SD's. The equations of motion are obtained by taking $|\delta\Psi\rangle$ as the set of 1-particle 1-hole excitations of the instantaneous SD,

$$|\delta\Psi\rangle \in |\alpha_p\alpha_h\rangle \equiv c^{\dagger}_{\alpha_p} c_{\alpha_h} |\Psi(t)\rangle. \tag{3.9}$$

in accordance with Thouless's theorem. For a state of N_e particles in a basis of dimension N_b, there are $N_e(N_b - N_e)$ particle-hole amplitudes to be determined compared to the $N_e N_b$ amplitudes in the representation Eq. (3.5). However, the use of Eq. (3.9) requires calculating both particle and hole orbitals in an instantaneous basis, which is very costly in carrying out the time evolution. An easier way to avoid the phase introduced by the Kohn-Sham single-particle Hamiltonian is by projection. The action of $\hat{H}_{KS}$ on the SD can be expressed in the instantaneous particle-hole basis as

$$\hat{H}_{KS}|\Psi\rangle = E_{KS}|\Psi\rangle + \sum_{\alpha_p,\alpha_h} v(\alpha_p, \alpha_h)|\alpha_p\alpha_h\rangle \tag{3.10}$$

where $E_{KS} = \langle\Psi|\hat{H}_{KS}|\Psi\rangle$. The unwanted first term can be removed in any basis simply by updating the wave function using the projected KS Hamiltonian $\hat{H}_{KS} - E_{KS}$. Thus, the single-particle orbitals are calculated as usual, but the phase of the SD is corrected by $\exp(+i\langle\hat{H}_{KS}\rangle\Delta t)$ at each time step. For our numerical example below, the problem does not arise because there is no electron-electron interaction in the valence space.

To summarize, we solve independently the time-dependent Kohn-Sham equations for $|\Psi_g\rangle$ and $|\Psi_c\rangle$. The two determinants are coupled by the X-ray photon interaction,

$$\hat{H}_x = v_x(c^{\dagger}_x c_c + c^{\dagger}_c c_x), \quad c^{\dagger}_x = \sum_i f_i c^{\dagger}_i \tag{3.11}$$

with f a form factor. Varying with respect to a_g, a_c one obtains the 2×2 matrix equation for these variables,

$$i\frac{d}{dt}\begin{pmatrix} a_c \\ a_g \end{pmatrix} = a_c \begin{pmatrix} \langle\Psi_c|\hat{H} - E_{KS,c}|\Psi_c\rangle & v_x\langle\Psi_c|\hat{H}_x c^{\dagger}_c|\Psi_{vg}\rangle \\ v_x\langle\Psi_{vg}|c_c\hat{H}_x|\Psi_c\rangle & \langle\Psi_{vg}|\hat{H} - E_{KS,g}|\Psi_{vg}\rangle \end{pmatrix} \begin{pmatrix} a_c \\ a_g \end{pmatrix}. \tag{3.12}$$

The hermiticity of $\hat{H}_x$ ensures that the normalization condition remains satisfied during the course of the evolution. The off-diagonal matrix element in this equation is expressible as the $N{+}1 \times N{+}1$ determinant

$$\langle \Psi_c | c_x^\dagger | \Psi_{vg} \rangle = \begin{vmatrix} \langle \beta_1 | \alpha_1 \rangle & ... & \langle \beta_1 | x \rangle \\ \langle \beta_2 | \alpha_1 \rangle & ... & \\ ... & & \\ \langle \beta_{N+1} | \alpha_1 \rangle & ... & \langle \beta_{N+1} | x \rangle \end{vmatrix}. \tag{3.13}$$

While this determinant is well-known in the analytic theory of the near-edge response[64], it is absent from the usual time-dependent Kohn-Sham theory based on a single Slater determinant.

To evaluate the linear response to the field of the X-ray photon, we start with the ground state wave function at time zero, which we call $|\Psi_g(0)\rangle$. We now perturb the system by an impulsive X-ray field, $\lambda \hat{H}_x \delta(t)$. The immediate evolution introduces a small component of the core-excited state into the wave function,

$$|\Psi(0_+)\rangle = |\Psi_g(0)\rangle + i\lambda v_x |\Psi_c(0)\rangle, \tag{3.14}$$

where $|\Psi_c(0)\rangle = c_x^\dagger |\Psi_{vg}(0)\rangle$. Eq. (3.14) has the required form as a sum of two determinants. Each is evolved in time with its own Kohn-Sham Hamiltonian. The evolution of $|\Psi_{vg}\rangle$ is trivial since the ground is stationary. All the dynamics comes from the evolution of $|\Psi_c\rangle$ by the time-dependent HS equations,

$$i\frac{da_{\beta i}}{dt} = \sum_j \langle i | \hat{H}_{KS} | j \rangle a_{\beta j} \text{ for } 1 \geq \beta \geq N_e + 1 \tag{3.15}$$

Then the real-time response from Eq. (3.2) is

$$R(t) = 2v_x^2 \mathrm{Re}\ \langle \Psi_c(t) | c_x^\dagger | \Psi_{vg}(t) \rangle. \tag{3.16}$$

This can be easily Fourier-transformed by Eq. (3.4) to give the absorption spectrum.

Our procedure provides an exact solution for the linear response if $\hat{H}_v$ and $\hat{H}_c$ are strictly one-body operators. This is because the intrinsically two-body part of the Hamiltonian does not make two-particle excitations or entangle the two Slater determinants after the initialization.

3.3 Numerical calculations

In this section we demonstrate the practicality of the method as applied to the MND Hamiltonian. The computer codes employed here are available at Ref. [73].

We write the two terms in the Hamiltonian as

$$\hat{H}_v = \frac{E_b}{N_b - 1} \sum_{i=1}^{N_b} (i - N_b/2) c_i^\dagger c_i \tag{3.17}$$

and

$$\hat{H}_c = \frac{v_c}{N_b} c_x^\dagger c_x, \quad c_x^\dagger = \sum_i^{N_b} c_i^\dagger. \tag{3.18}$$

Here E_b is the width of the band, and N_b is the number of orbitals in the band. We shall express energies in units of E_b, and time in units of $\hbar/E_b$. We start with a half-filled band, taking the number of valence electrons N_e to be $N_e = N_b/2$. We present calculations for the parameter sets listed in Table I.

As explained in the literature [64], the core-hole interaction strength v_c is not the most physically direct quantity determining the near-edge response. The effect of the Fermi-surface edge is more closely related to the shift of the single-particle orbital energies due to the core hole. Calling the shift $\Delta\varepsilon$, the relevant quantity is

$$\Delta\varepsilon \frac{dn}{d\varepsilon} = \frac{\delta}{\pi} \tag{3.19}$$

where $dn/d\varepsilon$ is the density of orbital states at the Fermi level. In the last equality, this is related to the scattering phase shift δ at the Fermi surface. The values of δ associated with the computed parameter sets are given in the last column of Table I.

The Greens function theory in Ref. [14] for the time-dependent response decomposes it into two factors, the overlap of Fermi sea determinants and the Greens function of the electron that was promoted to the valence band. We write the overlap of the Fermi sea determinants as

$$G(t) = \langle \Psi_{vg} | e^{-i(\hat{H}_v + \hat{H}_c)t} | \Psi_{vg} \rangle. \tag{3.20}$$

The main quantity of interest is the determinant in Eq. (3.16) which we call g_c, as

$$g_c(t) = \langle \Psi_c(t) | c_x^\dagger | \Psi_{vg}(0) \rangle \tag{3.21}$$

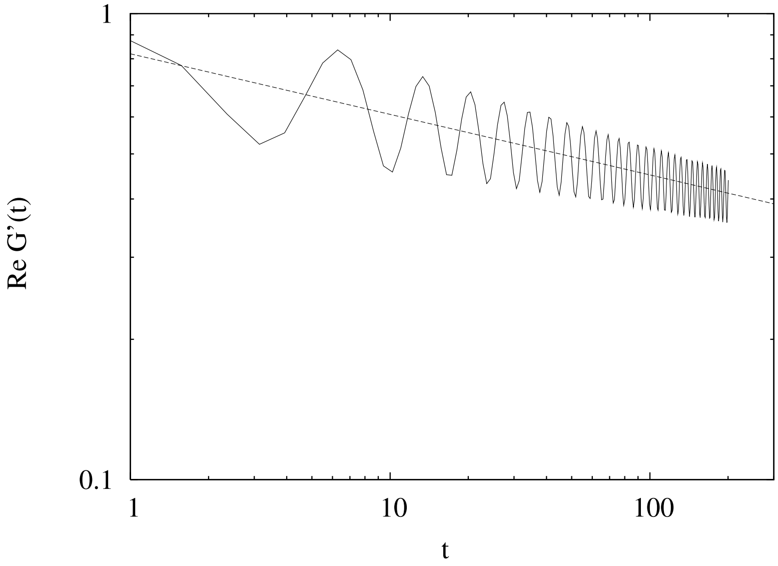

Figure 3.1: Re $G'(t)$ as a function of time for parameter set A. The line shows a visual power-law fit, $G'(t) \sim t^{-0.13}$.

Nozières and De Dominicis decompose it into two factors, $g_c(t) = g(t)G(t)$. We will not make use of that separation.

3.3.1 Fermi sea evolution

We first examine the Fermi sea overlap. To remove the phase of the core-excited ground state, we will examine the quantity

$$G'(t) = e^{i\sum_\alpha \varepsilon_\alpha t} \langle \Psi_{vg} | e^{-i(\hat{H}_v + \hat{H}_c)t} | \Psi_{vg} \rangle, \tag{3.22}$$

where ϵ_α are the Kohn-Sham eigenvalues of the ground-state orbitals. Figure 1 shows Re $G'(t)$ for parameter set A of Table I. It is plotted on a log-log scale to facilitate comparison with result of Ref. [14],

$$G(t) \sim (1/t)^{(\delta/\pi)^2}. \tag{3.23}$$

The predicted power-law dependence should be applicable over the time domain starting from $t_0 \sim 1/E_b$ and going to $t_1 \sim dn/d\varepsilon = N_b/E_b$, the time necessary to resolve individual orbitals in the band. In our units the range is $(t_0, t_1) = (1, N_b)$. One notices immediately that $G'(t)$ has a considerable oscillatory component. The oscillation has been found in other treatments of the problem as well, eg. [74, Eq. (3.4)]. As discussed in Ref. [64], the oscillation may be attributed to the deeply bound orbital at the bottom edge of the valence band. The line in the graph corresponds to the power law $G(t) \sim (1/t)^\gamma$ with $\gamma = 0.13$.

case	N_b	N_e	v_c	δ/π
A	256	128	-0.8	0.38
B	8	4	-0.8	0.39
C	512	256	-0.8	0.38
Z	256	128	0	0

Table 3.1: Parameter sets for the Hamiltonian Eq. (3.17,3.18).

This is rather close to the predicted power law derived in Ref. [14], $\gamma = (\delta/\pi)^2 \approx 0.14$.

The spectral function associated with $G'(t)$ is its Fourier transform,

$$G'(\omega) = \int_0^\infty dt e^{i\omega t} G'(t). \tag{3.24}$$

Fig. 3.2 plots Re $G'(\omega)$ for parameter sets A and B. For the set A shown in the left-hand panel one can see the peaks associated with individual states of the many-particle wave function. The dimension of the many-particle space is given by $\binom{N_b}{N_e} = 20$. The ground state is the peak on the far left, and 8-9 other states are visible in the plot. The right-hand plot shows Re $G'(\omega)$ for parameter set A. Here the individual states are so closely spaced that one can see only smooth curves. There are clearly two peaks in the spectrum, one associated with the ground state and its low-energy excitations, and the other associated with a localized orbital bound or nearly bound to the core hole. The secondary peak was discussed in Ref. [75] and also recently in Ref. [76]. In Fig. 3 we have replotted the Re $G'(\omega)$ ground-state peak on a log-log scale to make visible a power-law dependence on ω. The expected range of validity for a power law is within the interval $(\omega_0, \omega_1) = (1/N_b, 1)$

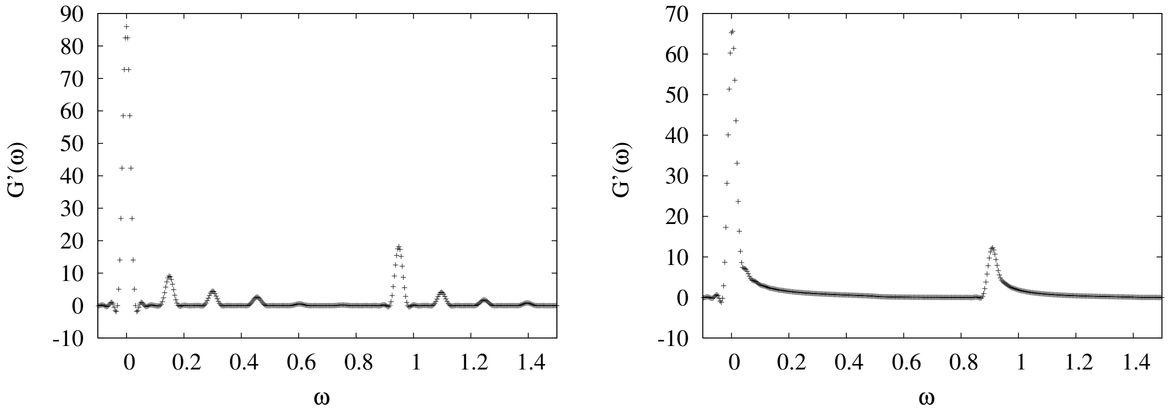

Figure 3.2: Re $G'(\omega)$ as a function of ω. Left-hand panel: results for a low-dimensional system, parameter set B. Right-hand panel: results for parameter set A.

in our units. The line in Fig. 3 shows the power-law $\omega^{-1.13}$. We can see that it provides a reasonable fit in the range $(0.02, 0.3)$ with some oscillation at low frequency.

3.3.2 Inclusion of the core electron

We now examine the propagation of the core-hole excited determinant with the core electron promoted to the valence band. The number of electrons in the determinant is now $N_b/2+1$. The initial wave function has equal amplitudes for the x electron in all the unoccupied orbitals; it thus has the same localization as the core-hole potential. Just as a reminder of the non-interacting physics, we show in Fig. (3.4) the imaginary part of $g_c(\omega)$ at $v_c = 0$. It is uniform across the region of unoccupied orbitals, with sharp edges at the Fermi surface and at the top of the band. The right-hand panel shows the Greens function with parameter set A. Note that the peak associated with a hole at the bottom of the valence band is missing. Evidently, the electron added by $c_x^\dagger$ operator ensures with a high probability that the hole is filled. The results in the right-hand panel are plotted in Fig. 3.5 on a log-log scale. The line is a visual fit to power-law behavior. Evidently, a power law gives a reasonable description over the energy interval $0.02 - 0.3$. According to the theory, the exponent is determined by

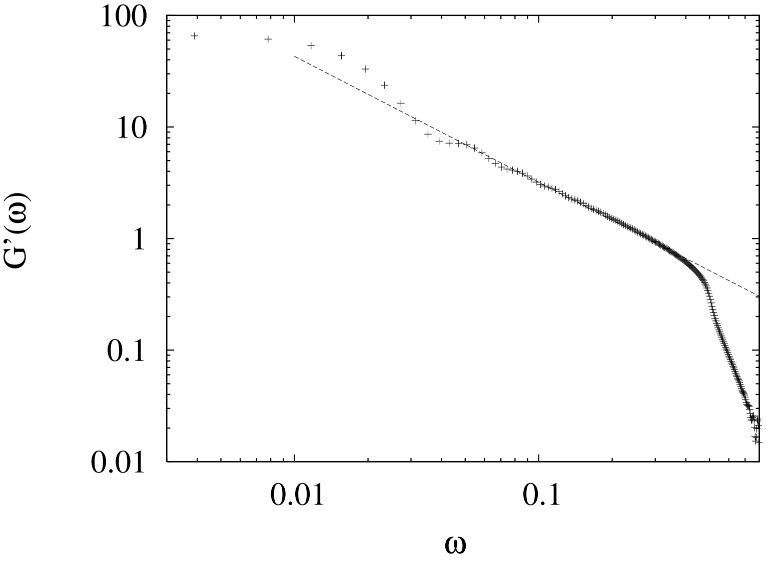

Figure 3.3: The same $G'(\omega)$ as in Fig.2b, plotted on a log-log scale. The line shows a visual power-law fit, $G'(\omega) \sim \omega^{-1.13}$.

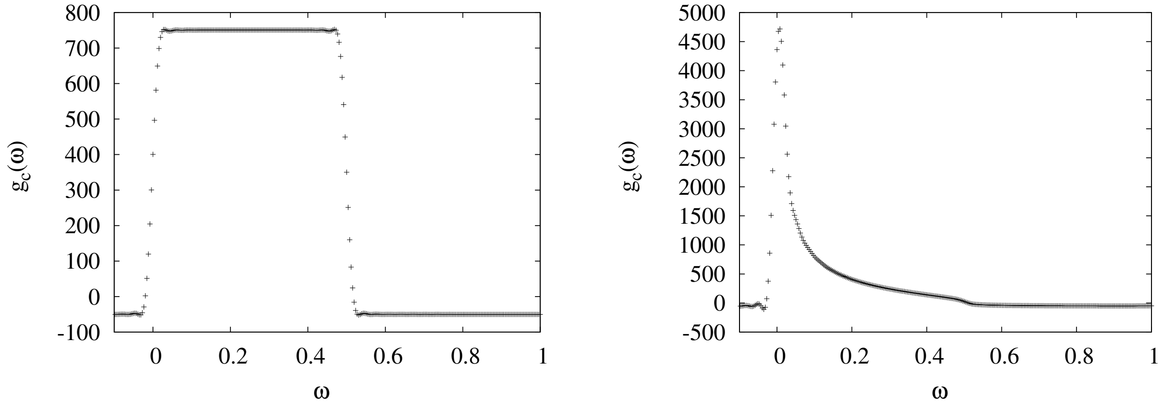

Figure 3.4: Left panel: core-excited Greens function with no interaction, parameter set Z. Right panel: the same quantity with parameter set A. Note the difference in vertical scale.

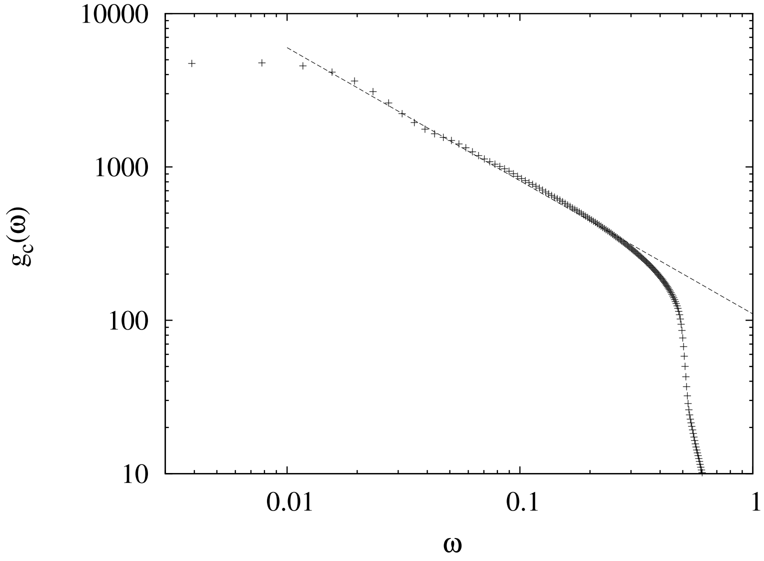

Figure 3.5: The determinant $g_c(\omega)$, plotted on a log-log scale. The line shows an approximate power law fit, $g_c(\omega) \sim \omega^{-0.85}$.

the phase shift according to the dependence [1].

$$\gamma = -2\frac{\delta}{\pi} + \frac{\delta^2}{\pi^2}. \tag{3.25}$$

Taking δ/π from Table I, the predicted value is $\gamma = -0.62$, compared to $\gamma = -0.85$ from the fit.

The small disagreement we find here persists over a large range of δ. Figure 3.6. shows a comparison over the range of δ accessible to the Hamiltonian. We see that the exponent is proportional to δ for small δ as in Eq. (3.25), but the coefficient is somewhat higher.

3.3.3 Other numerical treatments

Various numerical treatments of the MND Hamiltonian have been discussed and reviewed in Ref. [64]. The two main approaches are the Greens function formulation[77, 78, 79, 80, 74] and the formulation in terms of many-body determinantal wave functions[81, 82, 83, 84, 85].

---

[1] This is for a single partial wave and spin projection.

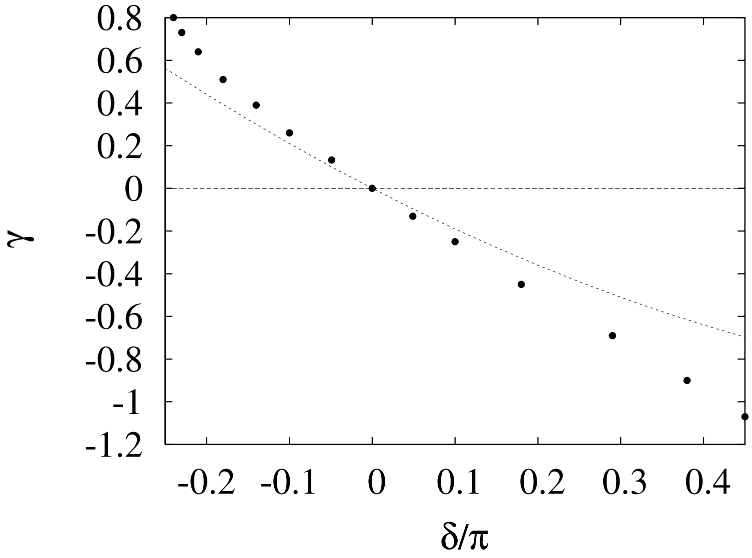

Figure 3.6: Solid circles: the power-law exponent extracted from the extended TDDFT response for the space $(N_b, N_e) = (256, 128)$. Dashed line: the analytic formula Eq. (3.25). The numerically computed exponent was extracted from the calculated $g_c(\omega)$ at $\omega = 0.03$ and 0.2 .

The former requires constructing functions of at least two variables in the time or frequency domain, governed by equations that are nonlocal in those variables. In this respect, the real-time wave function method is much more efficient since there is only one time variable and the equations to be solved are local in time. An early numerical work following the wave function approach is Ref. [81]. These authors constructed the numerically exact solutions of the core-hole excited Hamiltonian, and then used the ground state and one-particle excitations of the Hamiltonian as the final states. This procedure of enumerating the eigenstates was also used in Refs. [84]. The wave function approach was also used in Ref. [85], and the determinant was evaluated in real time, as in our approach. However, the procedure adopted there was based on the formulation of Ref. [75] which requires a matrix inversion. The near-singularity of the matrix apparently caused numerical difficulties that do not arise in the real-time approach. From a computational point of view, our approach is closest to that used in Ref. [82] and [83]. We note that these authors found that the critical exponents of the analytic Greens function treatment were only in qualitative agreement with the numerical results outside of a very small interval near $\omega = 0$.

3.4 Summary and outlook

We have derived an extension of time-dependent density functional theory that contains at least some of the subtle many-particle physics of X-ray near-edge absorption in metals. Numerically, the real-time theory is easy to carry out if the time-dependent electron-electron interaction is neglected. The absorption shows that the X-ray absorption power-law behavior is in qualitative agreement with the analytic results of Ref. [86], but not identical to them. A similar conclusion was obtained in Ref. [82].

Physically, the most important effect of the many-electron physics is core-hole screening. There are several numerical calculations in the literature that follow the Greens formalism of Ref. [14] and focus on this screening effect. For the absorption spectra, a commonly used approximation treats the system as fully relaxed in the presence of the core hole. Good fits can also be obtained under the assumption that the dynamic screening reduces the core-hole effects by a factor of two[62]. That work also presented a real-time dynamic calculation, but apparently used a diagonal approximation to Eq. (3.16). In any case, dynamic effects related to the core hole can be easily calculated in the real time method, so there is no reason to use any of these approximations.

So far we have not discussed the electron-electron interactions within the valence band. They are potentially important and are needed to treat the additional screening associated with the plasmon degree of freedom. Langreth has proposed a way to include plasmon effects in the Greens approach [34] and it was applied with some success in Ref. [87]. However, it involves distinct calculations for the plasmon physics and for the X-ray absorption. In contrast, the real-time TDDFT provides a unified framework for including the electron-electron interaction in the calculation. In the two-determinant theory one can simply add the Coulomb field of the instantaneous charge density of $|\Psi_c\rangle$ to the field generated by v_c. Of course, the presence of the interaction requires considerably more computational effort. The Coulomb field has to be calculated at each time step. Also, the overall phase of the $|\Psi_c\rangle$ has to be computed using one of the methods discussed in Sect. II. We believe that the problem is still computationally quite tractable; we leave the implementation to a future publication.

Acknowledgment

We acknowledge discussions with J.J. Rehr, A. Bulgac, and K. Yabana and helpful comments from C. Ullrich. We also thank U. Mosel Ref. [76] to our attention. This work was supported by the National Science Foundation under Grant PHY-0835543 and by the (US) Department of Energy under Grant No. DE-FG02-00ER41132.

Chapter 4

OBTAINING A DETERMINANTAL CORRELATION FUNCTION FROM RESPONSE

We derive an equivalence between the correlation function in a double-determinantal KS TDDFT and the true correlation function. The correlation function arises naturally from considering the density cross terms between a determinantal state where the X-ray was absorbed and a determinantal state where it was transmitted. The KS correlation function can then be naturally divided into transient and core-hole diagrams similarly to what Nozières and De Dominicis (ND) did for non-interacting electrons. We conjecture that although we lack a suitable approximate double-determinantal exchange-correlation (XC) kernel, we can still use the usual single-determinantal TDDFT functional to either calculate only the transient part, or to obtain the entire correlation function in the long-time limit given enough degrees of freedom.

4.1 Introduction

The absorption spectrum for optical and UV frequencies may be obtained from RT-TDDFT via the dipole response [13, 2]. The dipole response is the function of time obtained by integrating the density times the dipole field. However, this scheme is impractical to apply directly to XAS, due to limitations of ab-initio approximations to the exchange-correlation (XC) functional, and for efficiency reasons, since the photon frequency would be at least two orders of magnitude greater than the features of interest in the spectrum. In order to bypass these practical limitations, we introduce a double-determinantal Kohn-Sham TDDFT formulation. This allows us to model the exciton explicitly. Furthermore, by propagating the determinants separately we do not need to use a small enough time step to model the X-ray frequency. We obtain the spectrum from the dipole response of the double-determinantal system. The spectrum is shown to be equivalent to a determinantal correlation function.

4.2 Derivation from double determinantal TDDFT response

We excite a core-level electron with an electric field representing the X-ray. The electric field has a delta-function time-dependence and actually excites all frequencies, including X-ray and optical. However, we are only interested in X-ray frequencies, so we only consider states where a core level has absorbed the photon.

Let the external potential be approximated as $V = d$, the dipole operator. The X-ray excites the core electron $|c\rangle$ to create a photoelectron at time $t = 0$, $|\psi_x(0)'\rangle = (1 - \mathcal{P})d|c\rangle$, where $\mathcal{P}$ is the projector onto occupied ground state orbitals. Note that $d|c\rangle$ is well localized so we have ignored the X-ray wavelength.

Following Bertsch and Lee 2014 [58], we define the KS many-body state as a linear combination of a ground-state and excited-state determinants,

$$|\mathbf{\Psi}(t)\rangle = a_g|\mathbf{\Psi}_g(t)\rangle + a_x|\mathbf{\Psi}_x(t)\rangle \tag{4.1}$$

$$|\mathbf{\Psi}_g(t)\rangle = \det\{|\psi_i(t)\rangle\} \tag{4.2}$$

$$|\mathbf{\Psi}_x(t)\rangle = \det\{|\psi_i'(t)\rangle\}, \tag{4.3}$$

where $\mathbf{\Psi}_g$ is the ground state and $\mathbf{\Psi}_x$ is the excited state. Note that $\{|\psi_i(t)\rangle\}$ is the set of all KS ground-state valence electrons plus the KS core state $|c(t)\rangle$, while $\{|\psi_i'(t)\rangle\}$ is the set of all excited KS valence electrons plus the KS photoelectron $|\psi_x'(t)\rangle$. The amplitudes a_g and a_x depend on the strength of the X-ray field. They only change when a photon is absorbed or emitted, which does not happen during the time we take the response. Note that we will derive XAS from this state's density so we may invoke Runge-Gross theorem. The density is

$$\begin{aligned}\rho(\mathbf{r}) &= \langle\mathbf{\Psi}(t)|\hat{\rho}(\mathbf{r})|\mathbf{\Psi}(t)\rangle \\ &= |a_g|^2\rho_g(\mathbf{r},t) + |a_x|^2\rho_x(\mathbf{r},t) + 2\Re a_g^* a_x\langle\mathbf{\Psi}_g(t)|\hat{\rho}(\mathbf{r})|\mathbf{\Psi}_x(t)\rangle,\end{aligned} \tag{4.4}$$

where

$$\hat{\rho}(\mathbf{r}) = \sum_i \bigotimes_j (1 - \delta_{ij} + \delta_{ij}|\mathbf{r}\rangle\langle\mathbf{r}|) \tag{4.5}$$

is the density operator. The density ρ_g of the ground-state KS determinant $\mathbf{\Psi}_g$ is equivalent to the true ground-state density, and the density ρ_x of the excited-state determinant $\mathbf{\Psi}_x$

is equivalent to the true excited-state density. For details on this equivalence, see Section D.3.

We evolve the ground-state electrons with the ground-state KS Hamiltonian H and the excited state electrons with the excited KS Hamiltonian $H' = H + v_c$, which has an effective core-hole potential v_c. There are some important concerns regarding the XC functional which we will look into later. For valence levels, $|\psi_i(t)\rangle = |\psi_i(0)\rangle e^{-i\epsilon_i t}$ are simply the KS occupied ground states. We let $|c(t)\rangle = |c(0)\rangle e^{-i\epsilon_c t}$. The excited valence levels are initially in the ground state, $|\psi_i'(0)\rangle = |\psi_i(0)\rangle$. As previously stated, the photolectron is initialized as $|\psi_x(0)'\rangle = (1 - \mathcal{P})d|c\rangle$. In summary,

$$|\psi_i(t)\rangle = |\psi_i(0)\rangle e^{-i\epsilon_i t} \tag{4.6}$$

$$|\psi_i'(0)\rangle = |\psi_i(0)\rangle \tag{4.7}$$

$$\frac{d}{dt}|\psi_i'(t)\rangle = -iH'[\rho_x(t), \rho(t)]|\psi_i'(t)\rangle. \tag{4.8}$$

We readily obtain the spectrum from the density response, which is

$$\begin{aligned}\int d^3x V(\mathbf{x})\rho(\mathbf{x},t) = \int d^3x V\left(|a_g|^2\rho_g(\mathbf{x},t) + |a_x|^2\rho_x(\mathbf{x},t)\right)\\ + 2\Re a_g^* a_x \sum_k \det_{i,j}\langle\psi_i(t)|\mathcal{V}_{kj}|\psi_j'(t)\rangle\end{aligned} \tag{4.9}$$

where the operator $\mathcal{V}_{kj}$ is equal to V when $k = j$ or 1 when $k \neq j$. Note that ρ_g has no time dependence, and ρ_x oscillates only at optical and UV frequencies. The only terms to have any oscillations at the X-ray frequencies are the cross terms. Retaining only these physically relevant terms, we obtain

$$\int d^3x V(\mathbf{x})\rho(\mathbf{x},t) = 2\Re a_g^* a_x \sum_k \det_{i,j}\langle\psi_i(t)|\mathcal{V}_{kj}|\psi_j'(t)\rangle \tag{4.10}$$

Note that every term contains a factor of $e^{i\epsilon_c t}$ so we can factor it out of our time-evolution calculations.

Let us see how the terms in the determinant go. It can be expanded as

$$\begin{aligned}
&\langle c(t)|V|\psi'_x(t)\rangle \det_{i\neq c,j\neq x}\langle\psi_i(t)|\psi'_j(t)\rangle \\
&+\sum_{k\neq x}(-1)^{k-1}\langle c(t)|V|\psi'_k(t)\rangle \det_{i\neq c,j\neq k}\langle\psi_i(t)|\psi'_j(t)\rangle \\
&+\sum_{k\neq x,l\neq c}(-1)^{k+l}\langle\psi_l(t)|V|\psi'_k(t)\rangle \det_{i\neq l,j\neq k}\langle\psi_i(t)|\psi'_j(t)\rangle.
\end{aligned} \tag{4.11}$$

The major term is the first one, and represents the photoelectron returning to the core hole, emitting a photon. The second term is recognizable as the "diagrams" for a valence electron to emit a photon and end up in the core level. The last term contains "diagrams" where some electron winds up in the core level without emitting a photon, and some other electron emits a photon and ends up in the valence hole left by the first. These diagrams are probably negligible. Note that the "diagrams" we speak of are not perturbation theory diagrams, rather they are TDDFT KS diagrams! Also, these diagrams arise from N-body permutation cycles.

Note that the full determinant is simply the correlation function $\langle\mathbf{\Psi}_g(t)|V|\mathbf{\Psi}_x(t)\rangle$. Since the ground state simply oscillates with a single frequency E_0, we may write, up to some overall constant factors and the ground-state phase factor e^{iE_0t},

$$\begin{aligned}
\int d^3xV\rho(t) &= \langle\mathbf{\Psi}_g(0)|V|\mathbf{\Psi}_x(t)\rangle \\
&= \langle\mathbf{\Psi}_g(0)|d|\mathbf{\Psi}_x(t)\rangle \\
&= \langle\mathbf{\Psi}_x(0)|\mathbf{\Psi}_x(t)\rangle.
\end{aligned} \tag{4.12}$$

The last line is a determinantal autocorrelation function. The real part of the Fourier transform of this correlation function is the spectrum, therefore

$$F(t) = i\langle\mathbf{\Psi}_x(0)|\mathbf{\Psi}_x(t)\rangle \tag{4.13}$$

where F is the full Green's function for XAS. This is the same as the original expression for the Green's function, except the true many-body state has been replaced by a determinant of KS TDDFT states.

4.3 The double-determinantal XC functional

Interestingly we recover a determinantal autocorrelation function from the response. This method requires a double-determinantal KS Hamiltonian with a corresponding double-determinantal XC functional, however we have not developed such a functional. Instead we attempt to approximate the double-determinantal KS Hamiltonian by evolving two sets of KS states using single-determinantal KS Hamiltonians and using their cross terms. In this approximation the relative phase between the two determinants is not taken into account, and therefore there is no guarantee that the correlation function, which is derived from a product the two determinants, is accurate. Indeed, our calculations show that the spectrum obtained in this way contains regions of significantly negative intensity[1]. The KS determinants appear to interact non-trivially via the (correct) XC functional. We would need to create a new XC functional to obtain a closer approximation to the true density in order remove the pathologies in our Green's function.

We assume the correct double-determinantal XC kernel would differ from our current approximation only by providing a relative phase correction on the two determinants[2]. This comes from assuming each determinant evolves with the same density as in the corresponding single-determinantal TDDFT formulation. In other words, we expect the correct double-determinantal KS formulation to be compatible with the single-determinantal KS formulation when considering only the single-determinantal densities. With the phase correction we expect that we would recover the true spectrum and the negative intensities would vanish.

Even though we lack the phase-corrected XC, perhaps we may recover an approximate spectrum by invoking a separation of the Green's function similar to the Nozières-De Dominicis (ND) formalism, to be developed in the next section and in Chapter 5, or by taking a long time limit, where the density reaches a statistical equilibrium, to be developed in Appendices C and D.

---

[1] See Fig. C.1 and the accompanying discussion.

[2] Note that we can change a single-particle wavefunction by a spacially dependent phase, and retain the same instantaneous density. However this would change its momentum, and therefore its time-dependent density.

4.4 Nozières-De Dominicis-like separation of Green's function

Adapting the Nozières-De Dominicis (ND) formalism to our double-determinantal KS TDDFT formalism, we define the core-hole Green's function g_c as

$$g_c(t) = ie^{i\epsilon_c t} \det_{i\neq c, j\neq x} \langle \psi_i(t)|\psi'_j(t)\rangle. \tag{4.14}$$

The major terms in the determinant in Eq. (4.13) can be approximated as

$$\begin{aligned} F(t) \approx\ & g_c \langle c(0)|V|\psi'_x(t)\rangle \\ & + g_c \sum_j (-1) \frac{\langle c(0)|V|\psi'_j(t)\rangle \langle \psi_j(t)|\psi'_x(t)\rangle}{\langle \psi_j(t)|\psi'_j(t)\rangle} \\ & + g_c \sum_{jk} \epsilon_{jk} \frac{\langle c(0)|V|\psi'_j(t)\rangle \langle \psi_j(t)|\psi'_k(t)\rangle \langle \psi_k(t)|\psi'_x(t)\rangle}{\langle \psi_j(t)|\psi'_j(t)\rangle \langle \psi_k(t)|\psi'_k(t)\rangle} \\ & + \cdots \end{aligned} \tag{4.15}$$

where ϵ_{jk} is the Levi-Civita symbol. Notice the core-hole Green's function g_c factors out cleanly and we obtain the transient Green's function G. In practice we could also try simply dividing the full determinant by g_c to obtain G as a check.

We may obtain g_c via the cumulant method developed by Kas *et al.* [15]. We show in Chapter 5 that by taking the first term in our transient Green's function expansion, and using the cumulant method to obtain g_c, the pathologies that appear in the full determinant due to the lack of the XC phase correction are diminished.

Interestingly the original diagrams from ND can be translated directly into terms in our determinant. The zig-zags like those in Fig. 4.1 belong to the transient Green's function, and correspond with the photoelectron evolving via the TDDFT propagator into a valence hole, and the ejected valence particle continuing on, eventually evolving into the original photoelectron state. The two-point bubbles like in Fig. 4.2 correspond to terms in the determinant where two electrons are off diagonal, that is, the electrons have switched places. The separation of the diagrams in the original ND comes about from the assumption that the electrons have been renormalized such that they are effectively non-interacting. In our case the separation is due to our expression of the Green's function in terms of non-interacting KS electrons.

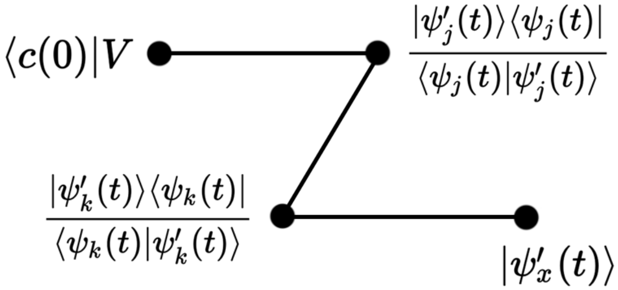

Figure 4.1: An example KS diagram in the transient Green's function (G). The lines represent contractions. Note that all vertices in the diagram occur at the same time except $\langle c(0)|V$.

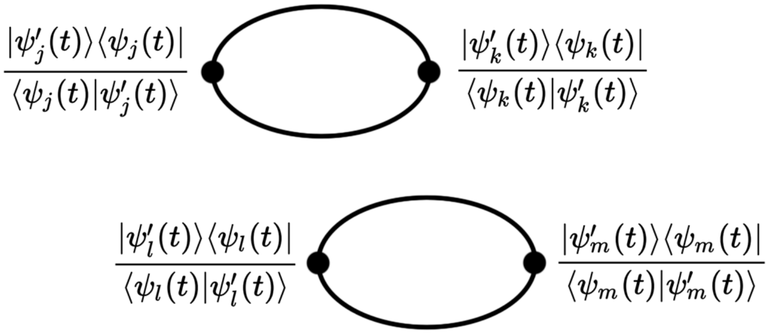

Figure 4.2: An example KS diagram in the core-hole Green's function (g_c). The lines represent contractions. The diagrams represent corrections on the diagonal term in the determinant. The sum of all diagrams, multiplied by the diagonal term, is the total correction.

Chapter 5

CONVOLVED CORRELATION AND CUMULANT APPROACH

In the original Nozières-De Dominicis (ND) formalism, the ground state valence electrons are renormalized so as to become effectively non-interacting particles. The effective core-hole potential is treated as a perturbation on the ground state. The XAS is then given by the Green's function

$$F(t'-t) = i \lim_{\tau \to t, \tau' \to t'} \langle 0 | c_c^\dagger(t') c_x(\tau') c_x^\dagger(\tau) c_c(t) | 0 \rangle \tag{5.1}$$

where $c_x^\dagger$ creates a photoelectron and c_c creates a core hole. This describes a core hole being created at time t, a photoelectron being created at a small time τ later, then the system propagates until time τ' when the photoelectron is annihilated and soon after the core hole is annihilated at t'.

Furthermore, the full Green's function F can be split into two parts, the core-hole Green's function g_c which includes the valence electrons' reaction to the core hole, and the transient Green's function G which contains information for the photoelectron evolving under an effective core-hole potential.

We present a few distinct methods to calculate F. Conceptually, the simplest is to calculate the F directly in real time using a determinantal time-correlation method. In this chapter we do not allow the electrons to interact. The determinantal method can also treat interacting electrons, however this presents its own practical complications which are discussed in Appendices C and D. Another method is to split the determinantal correlation function as in Eq. (4.15). In this method we may include interactions by calculating an approximation to G using the the time-correlation approach, and g_c using a cumulant expansion which takes as input the time dependent density response to the core hole. We may obtain the time dependent density using TDDFT, and calculate our approximation to G using the KS states from KS TDDFT.

5.1 *Initial state*

In all real-time methods discussed below, we begin by forming an initial state, then we evolve to obtain various time series from which we extract the spectrum. The initial state is created from a combination of valence electron and photoelectron initial states.

Within the original formulation of ND, the valence electrons are in the ground state when the core hole and photoelectron are created. Therefore in following ND we create an photoelectron orthogonal to the occupied states of the ground state Hamiltonian. The photoelectron state is then

$$|\psi_x(0)\rangle = (1 - \mathcal{P}^{occ})d|c\rangle \tag{5.2}$$

where d is the dipole operator, which can have any polarization, and $|c\rangle$ is the core state. We choose d to point in one of three orthogonal polarizations, and obtain three possible initial states. At the end of the calculation we average over the spectra for each polarization.

5.2 *Nozières-De Dominicis Formalism*

5.2.1 Non-interacting determinantal method

By assuming the ground state Kohn-Sham wavefunctions represent electrons renormalized such that they are non-interacting, we obtain a many-body state that is the determinant of the occupied ground state Kohn-Sham stationary states. We then evolve the Kohn-Sham wavefunctions under an effective core-hole potential, defining the many-body state at each time as the determinant of the time-dependent Kohn-Sham wavefunctions. From the time-dependent determinantal state, we obtain the correlation function directly.

In detail we obtain the many-body state via

$$|\boldsymbol{\Psi}(t)\rangle = \det\left\{|\psi_i(t)\rangle\right\}. \tag{5.3}$$

The set of $\{|\psi_i(t)\rangle\}$ include the Kohn-Sham valence electrons and a photoelectron ψ_x given initially by

$$|\psi_x(0)\rangle = d|c\rangle \tag{5.4}$$

where d is the dipole operator and $|c\rangle$ is the core-hole wavefunction. We evolve the time dependent the Kohn-Sham wavefunctions under a screened core-hole potential v_c^{FSR} obtained via a DFT SCF calculation with a core hole. This is the same SCF calculation as in the final-state rule. We full Hamiltonian we evolve under is $H_0 + v_c^{FSR}$, where H_0 is the ground state Kohn-Sham Hamiltonian.

$$|\psi_i(t)\rangle = e^{-i(H_0+v_c^{FSR})t}|\psi_i(0)\rangle \tag{5.5}$$

The full Green's function can be obtained via

$$\begin{aligned} F(t) &= i\langle \mathbf{\Psi}(0)|\mathbf{\Psi}(t)\rangle \\ &= i \det_{ij} \langle \psi_i(0)|\psi_j(t)\rangle \end{aligned} \tag{5.6}$$

The spectrum is the imaginary part of the Fourier transform

$$\begin{aligned} \mu(\omega) &= \Im F(\omega) \\ &= \Re \int_{-\infty}^{\infty} d\omega e^{i\omega t} \langle \mathbf{\Psi}(0)|\mathbf{\Psi}(t)\rangle. \end{aligned} \tag{5.7}$$

Note that we may also obtain the core-hole Green's function g_c simply by omitting the photoelectron ψ_x from the determinant $\mathbf{\Psi}$. Let us call this determinant $\mathbf{\Psi}_{val}$. Then

$$g_c(t) = i\langle \mathbf{\Psi}_{val}(0)|\mathbf{\Psi}_{val}(t)\rangle. \tag{5.8}$$

Note that in this method, once we assume the particles evolve under a non-interacting Hamiltonian, as ND does, then the correlation method described here contains no further approximations. The only choices made are what to use for the non-interacting Hamiltonian, and what the initial states are.

5.2.2 Separate Green's functions method

In the original ND formalism, the full Green's function calculated in frequency space by splitting into a core hole Green's function g_c, which contains interactions between the valence electrons and the core hole, and a transient Green's function G, which contains the photoelectron's interaction with the screened core hole. As discussed in Chapter 4, we adapt the ND equations to TDDFT KS states.

Formally, we take the core-hole Green's function g_c, the transient Green's function G, the total Green's function F, and XAS μ as given by

$$\begin{aligned} g_c(t) &= i\langle 0|e^{i\mathcal{H}t}c_c^\dagger e^{-i\mathcal{H}t}c_c|0\rangle \\ &= e^{iE_0t}\langle 0|c_c^\dagger e^{-i\mathcal{H}t}c_c|0\rangle \end{aligned} \tag{5.9}$$

$$G(t) = \langle c|d^\dagger \mathcal{P}e^{-i\mathbf{H}'t}\mathcal{P}d|c\rangle \tag{5.10}$$

$$\begin{aligned} F(t) &= i\langle 0|e^{i\mathcal{H}t}c_c^\dagger c_x e^{-i\mathcal{H}t}c_x^\dagger c_c|0\rangle \\ &\approx g_c(t)G(t) \end{aligned} \tag{5.11}$$

$$\mu(\omega) = \Im\frac{1}{\pi}\int_0^\infty dtF(t) \tag{5.12}$$

where $|0\rangle$ is the ground state oscillating with energy E_0, d is the dipole operator $\mathcal{P}$ is the projector onto unoccupied orbitals of the ground state, and $\mathbf{H}'$ is the single particle Hamiltonian with an effective core hole potential. Whereas ND use a non-interacting Hamiltonian, we use the KS TDDFT Hamiltonian for $\mathbf{H}'$.

In ND, the interactions between the valence electrons and photoelectron are renormalized out, so they are effectively non-interacting. In this way the Green's functions do not interact and the total Green's function can be expressed as a convolution of the core hole and transient Green's functions. In our case we make the approximations that the photoelectron has no effect on the valence electrons, while the valence electrons only affect the photoelectron via an effective static screening.

We obtain the core hole Green's function via a cumulant expansion, and the transient Green's function via a time-correlation function. It is interesting to note that we observe a small amount shake-down in the transient Green's function, which represents the photoelectron mixing with the valence electrons. This shake-down shows up in the final, convolved spectrum for XAS as peaks below the edge, and is an error in the ND-like approximation which allows the photoelectron and valence electrons to occupy the same orbital. If we enforced Fermi statistics, the shake-down of the photoelectron would require the shake-up of a valence electron, and the resulting peaks would show up at or above the edge in the XAS.

Although within the ND formalism, the transient and core hole Green's functions must be entirely independent for them to be separable, we have explored using TDDFT to obtain the transient Green's function. This is because if the approximation that the Green's functions are independent is valid, then the effect of TDDFT will be only to add an effective screening which quickly becomes nearly static. Our calculations of G with TDDFT versus final-state screening of the core hole are approximately the same, and therefore the it appears that within our approximations, G is approximately independent of g_c, and furthermore the TDDFT screened core hole is approximately the same as the final-state screened core hole.

5.3 Cumulant expansion of core-hole Green's Function

The "dressed" core-hole Green's function, g_c, contains the bare Green's function plus plamons which are created by interactions of the valence electrons with the bare core-hole. The bare core-hole Green's function $g_c^{(0)}$, in following ND, is taken to be structureless and simply oscillates at a single frequency.

In the linear response regime, we may expand the core-hole Green's function g_c in terms of the cumulant $C(t)$ and bare core-hole Green's function $g_c^{(0)}$ according the following equations

$$\beta(\omega) = \frac{\omega}{\pi}\int_0^\infty dte^{i\omega t}\int d^3xv_c(t)(\rho(t)-\rho(0)) \tag{5.13}$$

$$C(t) = \int_{-\infty}^{\infty} d\omega\beta(\omega)\frac{e^{i\omega t}-1}{\omega^2} \tag{5.14}$$

$$g_c(\omega) = \int_0^\infty g_c^{(0)}(t)e^{C(t)}e^{-i\omega t}dt \tag{5.15}$$

$$g_c^{(0)}(t) = i\theta(t)e^{i\epsilon_c t}, \tag{5.16}$$

where $\theta(t)$ is zero for $t < 0$ and one elsewhere, and ϵ_c is the core level energy. See eq. 44. of reference [34]. The imaginary part of $g_c(\omega)$ is the valence-band shake-up spectrum which corresponds roughly with XPS.

In practice we remove the average from $\int d^3xv_c(t)(\rho(t)-\rho(0))$ before taking the transform. This allows us to enforce that the integrand for $C(t)$, $\beta(\omega)(e^{i\omega t}-1)/\omega^2$, is zero at $\omega = 0$, so that the expression is well behaved.

Note that $\int d^3xv_c(t)(\rho(t)-\rho(0))$ is a cosine series. This is because the sudden onset of the core hole enforces a boundary condition which implies the time series is described by the a superposition of cosines, and contains no sines. Intuitively it is akin to holding a system in an unrelaxed position and suddenly letting go.

The Cumulant expansion is derived from the linked cluster theorem, which implies

$$g_c(t-t') = g_c^{(0)}(t-t')e^{C(t-t')} \tag{5.17}$$

where $C(t)$ is the sum of all diagrams which would be linked when all instances of the bare core-hole propagator $g_c^{(0)}$ are removed. In our case there is only one such "linked" diagram in $C(t)$, which represents the plasmon propagator.

We obtain the density to calculate β via TDDFT with a Crank-Nicolson propagator. This method is closely based on the method developed by Takimoto *et al.* for real-time TDDFT optical response [2].

Note that our expression for $C(t)$ only applies within linear response with respect to core-hole strength. In particular, the factor $\beta(\omega)$ which appears in $C(t)$ would need to be replaced with a more general form when outside of linear response. To calculate β within linear response, we add a scaling factor λ to the core-hole potential. Then we scale up β by $1/\lambda^2$. $\rho(t)$ is calculated using RT-TDDFT. Note that we scale by $1/\lambda^2$ since both δv and $\delta\rho$ are linear in λ.

$$\delta\rho(t) = \lambda(\rho(t) - \rho(0)) \tag{5.18}$$

$$\delta v = \lambda v_c \tag{5.19}$$

$$\begin{aligned} \Rightarrow \beta(t) &= v_c(\rho(t) - \rho(0)) \\ &= \delta v \delta\rho(t)/\lambda^2 \end{aligned} \tag{5.20}$$

To obtain the XAS spectrum, g_c must be convolved with the photoelectron Green's function G.

5.4 Core-hole potential

When adding a core-hole, we may either leave the core electron in place and simply introduce an effective core-hole potential to the system, or actually remove the core electron. Calculationally it is more convenient to add an external potential, since we already use such an external potential to calculate β. Removing the core electron introduces complications with PAW as described below. We have tried both methods for calculating the transient Green's function and found the differences to be small.

When applying the external potential, the potential is integrated against the pseudo wavefunctions and the core correction partial waves. The integration aginst pseudo wavefunctions is straightforward since the pseudo wavefunctions are on a cartesian grid. The integration against core correction partial waves must be handled separately for each atom. The core correction partial waves are expressed as a combination of spherical harmonics, so the potential is also expanded in spherical harmonics to perform the integration. For the atom which has the core hole, the expansion is trivial since the effective core-hole potential is spherically symmetric. For off-site atoms, the potential is expanded in an a Taylor series to first-order about the site. This appears to be a sufficient approximation because we have found in calculations of β that the zero order contribution is dominant in the shape of the spectrum. This is confirmed by a quick estimate of the strength of the second-order term relative to the zero-order term. The PAW cutoff for Carbon is $1.14a_0$,[1] while the distance between two Carbon atom nuclei is at least about $2.65a_0$. This means for a $1/r$ potential, the second order terms are at most $\frac{1}{2}\left(\frac{1.14}{2.65}\right)^2$, or about 0.09 times the zero order term, which is itself 1/2.65 Hartree. This is further reduced by the size of the d-character PAW correction, which is small since d-waves have little overlap with the core.

An alternate method for adding a core hole is to actually remove a core electron, resulting in a change in the PAW setup. A PAW setup contains a set of pseudo and all-electron partial waves. Since a core electron is removed, this means a new set of pseudo and all-electron partial waves need to be consnstructed. When changing the PAW setup, one must also be careful to correct for the fact that given an all-electron wavefunction, its pseudized counterpart wavefunctions with the first PAW setup may not be the same as with the second setup. Therefore the wavefunctions need to be re-pseudized. Writing the PAW reconstruction relation for both PAW setups,

$$|\psi\rangle = \mathcal{T}_1|\tilde{\psi_2}\rangle \tag{5.21}$$

$$|\psi\rangle = \mathcal{T}_2|\tilde{\psi_2}\rangle \tag{5.22}$$

---

[1] a_0 is the Bohr radius. Its value is 0.529 Å.

where $\mathcal{T}_1$ and $\mathcal{T}_2$ are the PAW correction operators. We need to calculate

$$|\tilde{\psi}_2\rangle = \mathcal{T}_2^{-1}\mathcal{T}_1|\tilde{\psi}_1\rangle. \tag{5.23}$$

Expanding,

$$\begin{aligned}\mathcal{T}_2^{-1}\mathcal{T}_1 = \sum_{ij}\Big[1 &+ \Big(|\tilde{\phi}_{2i}\rangle - |\phi_{2i}\rangle\Big)\langle p_{2i}| \\ &+ \Big(|\phi_{1i}\rangle - |\tilde{\phi}_{1i}\rangle\Big)\langle \tilde{p}_{1i}| \\ &+ \Big(|\tilde{\phi}_{2i}\rangle - |\phi_{2i}\rangle\Big)\langle p_{2i}|\Big(|\phi_{1j}\rangle - |\tilde{\phi}_{1j}\rangle\Big)\langle \tilde{p}_{1j}|\Big]\end{aligned} \tag{5.24}$$

A possible pitfall of this approach is that the re-pseudized wavefunction may not be as smooth, and so smaller grid spacing will be needed to converge the calculation. Additionally, inverting the PAW correction operator is a complicated process.

5.5 Equivalence to first-order perturbation theory

As a check and to see how things go, we expand the determinantal method and the cumulant method to first order in perturbation theory, assuming *absolutely* no interactions between electrons, not even via a time-dependent density-functional potential[2]. For simplicity let us ignore the spin of the electrons. We may fill in the appropriate factors of two later. Also, let us assume the system has a gap. This allows us to ignore degenerate eigenstates because all first order particle-hole excitations will be between eigenstates of different energies. The unperturbed Hamiltonian H_0 and perturbed Hamiltonian H' are

$$\begin{aligned}H_0 &= H_{KS}[\rho(0)] \\ H'(t) &= H_0 + v_c\theta(t),\end{aligned} \tag{5.25}$$

where the perturbation v_c is chosen to be a small potential representing the core-hole[3]. Notice that the density argument to the KS Hamiltonian H_{KS} is the density at time $t = 0$,

---

[2] To clarify, the particles are truly non-interacting in the sense that they have *absolutely no effect* on each other. It must be emphasized that here "absolutely non-interacting" is distinct from the sense of "non-interacting" from the literature on KS TDDFT. In KS TDDFT the particles in fact interact indirectly through an external potential which is a functional of the time-dependent density. In the "absolutely non-interacting" system of this section, even the indirect interaction via the external potential is absent.

[3] Since we are only interested in checking that the determinantal and cumulant methods agree for the absolutely non-interacting system, the perturbing potential does not need to be physically accurate.

i.e. the ground state density. The non-interacting perturbed Hamiltonian H' is not updated when the density changes.

For convenience, let

$$V_{ij} = \langle i|v_c|j\rangle \tag{5.26}$$

where v_c is the core-hole potential, and $\{|i\rangle\}$ are the ground state single particle eigenstates. Since we have a non-interacting system, the many body ground state is

$$|\boldsymbol{\Psi}_g\rangle = \det_{i\leq f}\{|i\rangle\}, \tag{5.27}$$

where i runs over single particle eigenstates below f, the Fermi level. The system starts in the ground state of H_0, then each electron evolves under the perturbed Hamiltonian $H'(t > 0) = H_0 + v_c$.

$$|\boldsymbol{\Psi}'(0)\rangle = |\boldsymbol{\Psi}_g\rangle \tag{5.28}$$

$$|\boldsymbol{\Psi}'(t)\rangle = \det_{i\leq f} |\psi'_i(t)\rangle \tag{5.29}$$

$$|\psi'_i(t)\rangle = e^{-iH't}|i\rangle \tag{5.30}$$

Let $|n^{(1)}\rangle$ be an eigenstate of the perturbed Hamiltonian, to first order in v_c. Expanding the overlap between an eigenstate of the perturbed Hamiltonian $H'(t > 0)$ with an eigenstate of the ground state Hamiltonian to first order in v_c yields

$$\langle n^{(1)}|m\rangle = \delta_{nm} + \sum_{n\neq m} \frac{V_{nm}}{\epsilon_n - \epsilon_m} \tag{5.31}$$

therefore

$$|\psi'_i(t)\rangle = |i\rangle e^{-i\epsilon_i t} + \sum_{j>f} \frac{V_{ji}}{\epsilon_j - \epsilon_i}|j\rangle e^{-i\epsilon_j t}. \tag{5.32}$$

The first-order excitations must be to states $j > f$ due to Fermi statistics. This will be useful for expanding both the determinantal and cumulant forms.

5.5.1 Cumulant

Let us first focus on expanding the cumulant in perturbation theory. The main part is the response.

$$\begin{aligned}\int d^3xV(\mathbf{x})\delta\rho(\mathbf{x},t) &= \sum_{i\leq f}\left(\langle\psi_i'(t)|v_c|\psi_i'(t)\rangle - \langle\psi_i'(0)|v_c|\psi_i'(0)\rangle\right)\\ &= \sum_{i\leq f}\langle i|e^{i\epsilon_i t}v_c\left(\sum_{j>f}\frac{V_{ji}}{\epsilon_j-\epsilon_i}|j\rangle e^{-i\epsilon_j t}\right) + h.c. + const \\ &= \sum_{i\leq f, j>f}\frac{|V_{ij}|^2}{\epsilon_j-\epsilon_i}e^{-i(\epsilon_j-\epsilon_i)t} + h.c. + const\end{aligned} \tag{5.33}$$

Let us drop the constant term and the Hermitian conjugate term, which is what is done in practice when calculating the spectrum. Now we may expand the spectrum $\Im g_c/\pi$, expressed in terms of the cumulant, to first order.

$$\begin{aligned}\mathrm{XPS}_{\mathrm{cumulant}} &= \frac{\beta(\omega)}{\omega^2}\\ &= \frac{1}{\pi\omega}\int dte^{i\omega t}\theta(\omega)\int d^3xV(\mathbf{x})\delta\rho(\mathbf{x},t)\\ &= \sum_{i\leq f,j>f}\frac{|V_{ij}|^2}{\omega^2}\delta(\omega-(\epsilon_j-\epsilon_i))\end{aligned} \tag{5.34}$$

5.5.2 Determinant

In taking determinantal states in linear order in V^2, note that to this order the determinantal excited states can only have a single particle-hole excitation.

Consider an excited determinantal state containing a single excitation from level $|m'\rangle$ to $|n'\rangle$,

$$|\mathbf{\Psi'}_{mn}\rangle = \det_j\{|j'\rangle\}, \tag{5.35}$$

where j runs over n and all states below the Fermi level, except m. We have, up to an overall sign, and retaining only terms up to linear order in v_c,

$$\begin{aligned}\langle\mathbf{\Psi}_g|\mathbf{\Psi'}_{mn}\rangle &= \det_{i,j}\langle i|j'\rangle\\ &= \langle m|n'\rangle\\ &= \frac{V_{mn}}{\epsilon_n-\epsilon_m}.\end{aligned} \tag{5.36}$$

Many factors reduce to unity since $\langle k|k'\rangle = 1$ for any level k. Also, the determinant has many terms which contain factors

$$\langle m|k'\rangle\langle k|n'\rangle \tag{5.37}$$

where $k \neq m$. These terms are second order in v_c so we neglect them.

The spectrum is

$$\begin{aligned} \mathrm{XPS}_{\mathrm{determinantal}} &= \sum_{m\leq f, n>f} |\langle \mathbf{\Psi}_g|\mathbf{\Psi}'_{mn}\rangle|^2 \delta(\omega - (\epsilon_n - \epsilon_m)) \\ &= \sum_{m\leq f, n>f} \frac{|V_{mn}|^2}{\omega^2}\delta(\omega - (\epsilon_n - \epsilon_m)), \end{aligned} \tag{5.38}$$

where the pair (m, n) runs over all possible particle-hole pairs. The above shows that the determinantal overlap reduces to a single-particle overlap. I showed earlier that the cumulant has the same form. Therefore it follows the determinantal and cumulant methods are the same to first-order perturbation in V^2.

A calculation using a benzene system with a small bare core-hole, and with non-interacting electrons, shows that the three methods agree (see Fig. 5.1). The core hole is gaussian shaped, $\sigma = 1$ Bohr, with height 0.02 Hartree/e at the center.

5.6 Core-hole green's function compared with XPS

The core-hole Green's function contains the reaction of the valence electrons to the creation of the core-hole. It is modeled via the core-hole response β and a first order cumulant expansion. The response β roughly corresponds with a weighted average of EELS over momentum transfer $\mathbf{q}$, while the core-hole Green's function roughly corresponds with XPS. In comparing with EELS and XPS, it is important to remember that certain features cannot be modeled within our approximations. Our core-hole response models plasmons well, but it will not give extrinsic losses in EELS, nor will it have the multiple excitations of the same plasmon which show up EELS. In addition, our calculation of β relies on TDDFT with PBE functional and therefore is subject to the limitations of that technique. For example, charge transfer excitations usually are not well described.

In Figs. 5.2 and 5.3, we compare the C_{60} spectrum calculated via the cumulant to experiment [88]. We see that the plasmon at 5 eV and the large plasmon at about 34

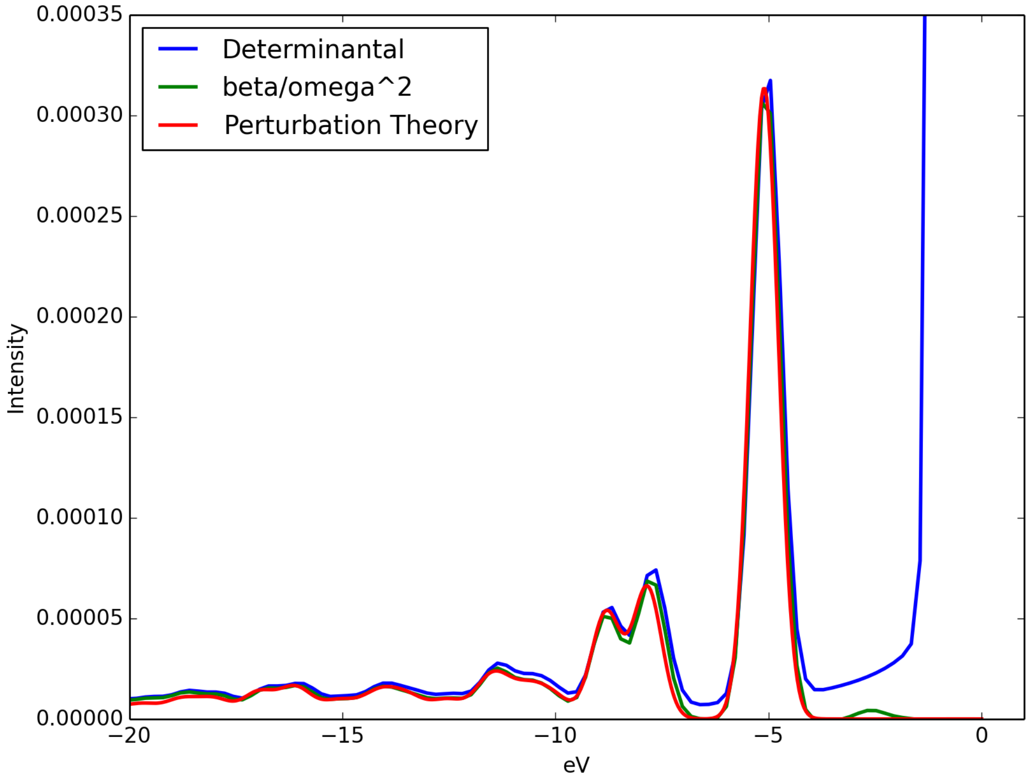

Figure 5.1: Benzene shakeup spectrum with non-interacting electrons. The core-hole potential is a gaussian well, $\sigma = 1$ Bohr, with height 0.02 Hartree/e. Note that the quasiparticle peak in this figure goes up to an intensity of 1.2 eV^{-1}

eV in the XPS show up in β. However, once we calculate the XPS, the large plasmon is suppressed and becomes much lower than the experiment. This may be in part due to the large experimental background that probably contains losses not accessible by our methods. I have plotted the results for a scaling factor λ of 0.05. β has been scaled back up by the corresponding amount before using it to calculate g_c. Note that the intensity scale is absolute and the imaginary part of g_c integrates to 1. To aid the eye in comparing with XPS, have also plotted the imaginary part of g_c versus XPS with background subtraction in Fig. 5.3. The background is a rough estimate of extrinsic contributions to XPS.

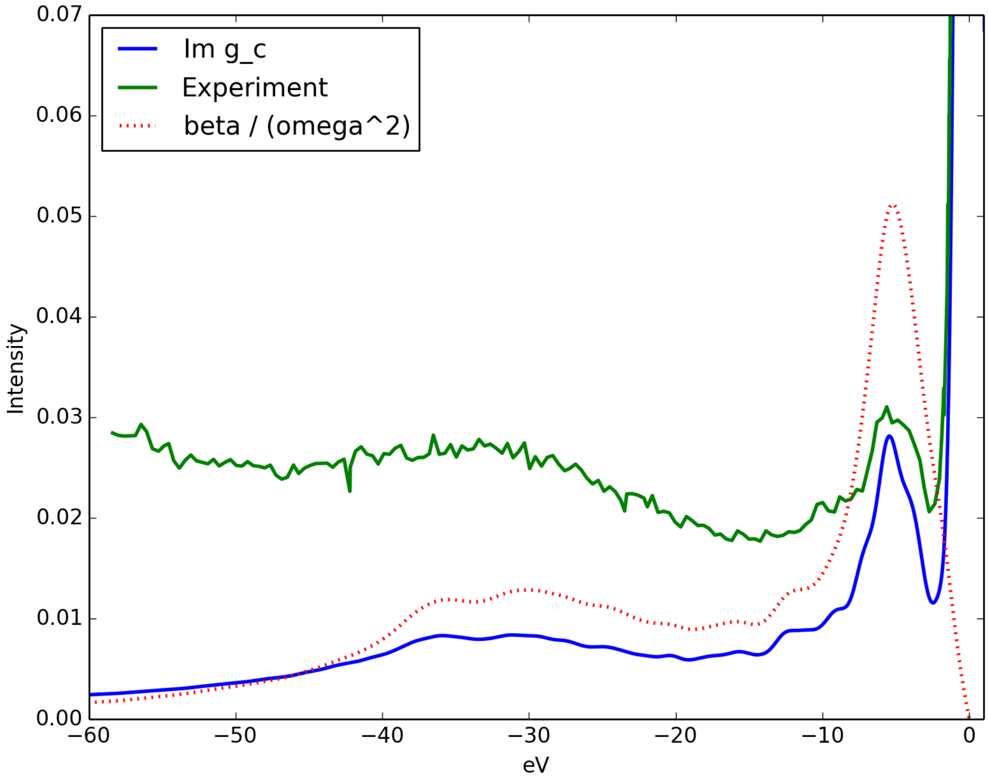

Figure 5.2: C$_{60}$ g_c and β compared with experimental XPS. The XPS is scaled to match g_c. g_c has been broadened such that the quasiparticle peak matches experiment. β has been scaled by 0.05 and reflected about 0 eV to show the correspondance to plasmons in XPS. The low energy plasmon at about 5 eV matches well with experiment. The large plasmon peak at 34 eV in the experiment is reproduced in β but becomes suppressed in g_c. Much of the difference in intensity is likely due to the lack of non-linear and extrinsic effects in the theory.

In Fig. 5.4, we compare the cumulant approach to graphite XPS experiment [89]. The plasmons at -7 eV and -30 eV in XPS show up in our calculation of g_c, but at a much lower in intensity. This is perhaps because in graphite much of the plasmon intensity is caused by the photoelectron exciting the valence electrons, our calculation of g_c does not

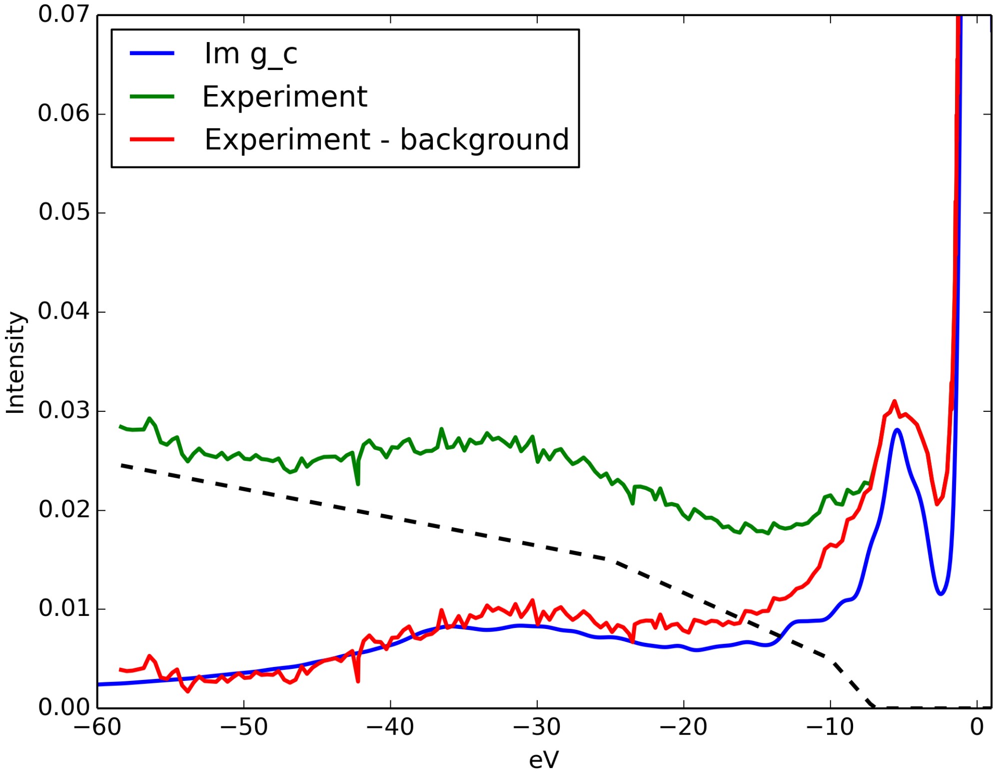

Figure 5.3: C_{60} g_c and β compared with experimental XPS, with background removed. The background, in black, is estimated to mostly consist of extrinsic contributitons, which tend to increase with energy.

include. There is also a large asymmetry of the quasi-particle peak which suggest some very low energy plasmons. g_c shows a plasmon at about -3 eV which may explain a part of the asymmetry in the quasparticle peak. Our calculation is not accurate at low frequencies, since these require very long simulated time intervals compared to the largest allowable time step. Since the fastest oscillating plasmon frequencies are at about 130 eV, this requires a time step of about 10 as. The loss of accuracy at frequencies of absolute value at or below 1 eV can be seen in slightly negative values of $\beta(\omega)$ at this point (not shown). This limitation of our calculation also applies to C_{60}, however in that system the system does not appear

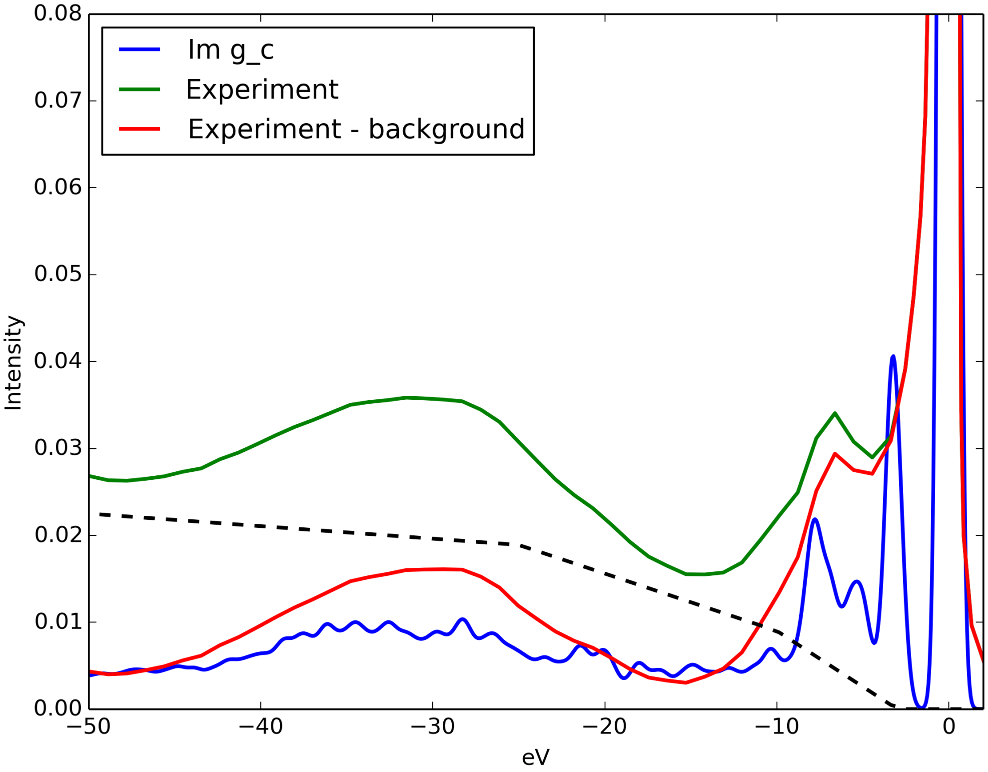

Figure 5.4: Graphite spectrum $\Im g_c$ compared with experimental XPS [89]. The experiment has been scaled, and the calculated spectrum broadened such that the quasiparticle peaks match. The total spectral weight of $\Im g_c$ is 1. The low energy plasmons at about 7 eV match well with experiment. The large plasmon peak at 30 eV in the experiment shows up clearly in our calculation but at a much reduced intensity. Much of the difference in intensity is likely due to the lack of non-linear and extrinsic effects in the theory.

to have such low energy plasmons.

Recalling that our expression for XPS only applies to the linear response regime, it is important to test that β is indeed within the linear regime. We see in Fig 5.5 that it is approximately in the linear regime up to a strength of $\lambda = 0.2$, but when we go to $\lambda = 1.0$ such that the simulated core-hole matches the physical core-hole strength, β

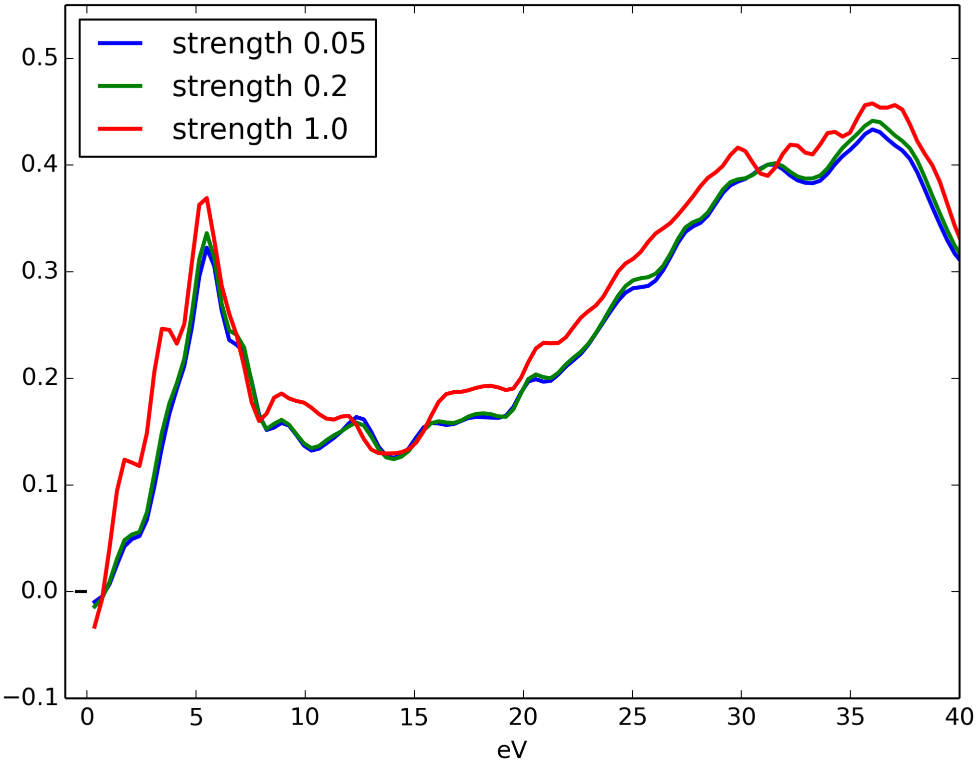

Figure 5.5: C_{60} $\beta(\omega)/\omega$ at different values of the core-hole scaling factor λ. There are significant non-linear effects at $\lambda = 1.0$, especially at small energies.

begins to show some non-linear effects, although the spectrum does not differ drastically as a whole. The non-linearity can also be seen by calculating the total satellite weight a. It goes from 0.72 at $\lambda = 0.05$ to 0.73 at $\lambda = 0.2$ to 0.87 at $\lambda = 1.0$. Therefore, β does remain approximately within the linear regime. However, the non-linearity does have a significant effect on the intensity of the low energy plasmon peaks. For example, the plasmon at 2 eV is the most prominent plasmon in the XAS. Therefore, the non-linearity possibly introduces significant error in the calculation of XAS. In the next chapter I discuss obtaining XAS without assuming linear response. One final consideration for the a values is that they are unexpectedly high. The total satellite intensity is equal to $1 - e^{-a}$. The satellites generally appear to have too much intensity in our calculations. This requires further study.

In Fig. 5.6, the RTXS calculation of condensed Si $\beta(\omega)$ produces closely the EELS experiment [90] plasmon peak at about 17 eV. It is slightly closer to the experiment than RT-SIESTA. In both calculations a core hole with a shape of $1/r$ capped at 1 Bohr was used. This is because RT-SIESTA uses the pseudopotential method and does not model the core region accurately.

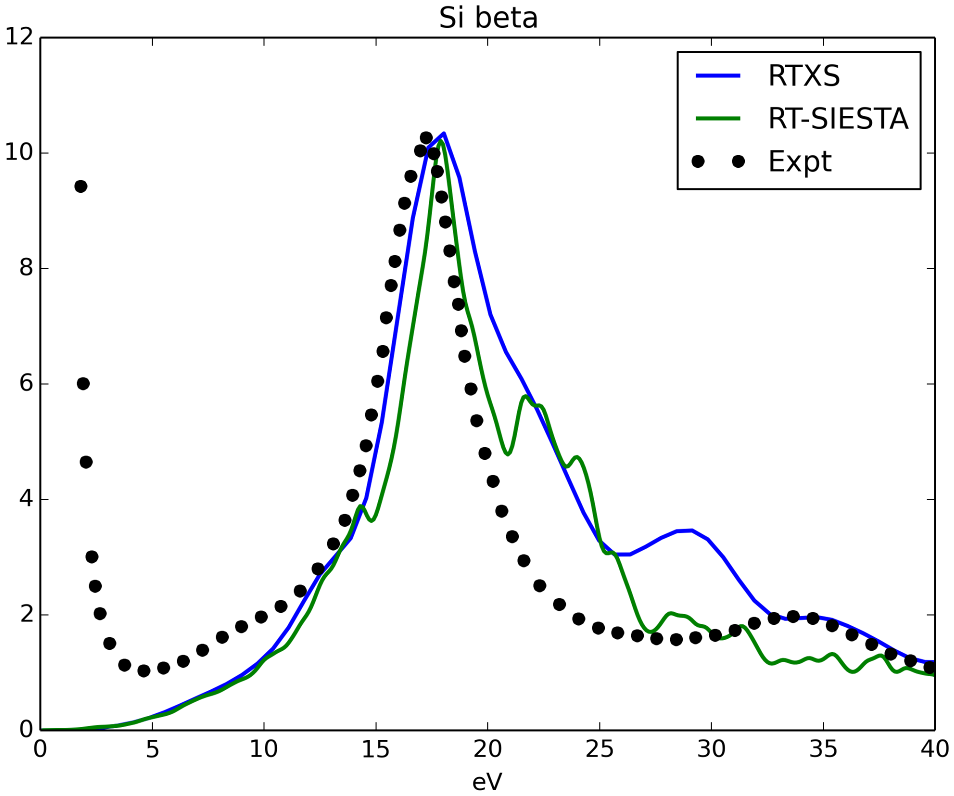

Figure 5.6: Silicon β compared with RT-SIESTA and experimental EELS. Both calculations agree closely with experiment on the plasmon peak at 17 eV.

5.7 Time-correlation method for calculating transient Green's function

In our single particle approximation to the transient Green's function, we include only single particle amplitude for the photoelectron to evolve into any orbital. For example, if the photoelectron evolves into an orbital below the Fermi level, we do not include the amplitude factors from requiring that a valence particle-hole pair has been created. In our calculations, the amplitude of the photoelectron filling a valence hole can be seen as small spurious pre-edge peaks.

In the ΔSCF approximation, the XAS is given by

$$\mu(t) = \frac{1}{\pi}\int_0^\infty dt \exp i\omega t \langle \psi_+(0) | \psi_+(t) \rangle \tag{5.39}$$

The initial state $\psi_+(0)$ is given by the dipole operator $d|c\rangle$, projected onto unoccupied ground states.

In traditional methods, an ambiguity exists as to the single particle Hamiltonian we should evolve under to obtain $\psi_+(t)$. In the final-state rule, we use the Kohn-Sham Hamiltonian with a fully-screened core-hole, and the initial state is created by projecting out occupied states of this final-state Hamiltonian. Note that as discussed above, we project out the occupied states of the ground state Hamiltonian when following the ND formalism.

5.7.1 XAS results

We compare with experimental and theoretical results for C_{60}, graphite, and diamond. We have chosen to study C_{60} and graphite in particular because they have been studied using a Mahan-Nozières-De Dominicis approach by Wessely *et al.* Their calculation is performed in frequency space with VASP as the DFT engine [36]. Wessely *et al.* approximate the effective core-hole potential using adiabatic screening[4]. Additionally they use effectively non-interacting electrons[5], and their method does not make use of TDDFT or real-time

---

[4] Note that the approximation of an adiabatically screened effective core-hole potential is a subtly distinct approximation from the final-state rule, in which the valence electrons are adiabatically relaxed after the creation of the core hole. See the original ND formulation [14] and Eq. (14) of Wessely *et al.* [36].

[5] The electrons in the approach of Wessely *et al.* do not interact with a Kohn-Sham time-dependent external potential. See Eq. (1) of Wessely *et al.* [36].

dynamics. When Wessely *et al.* compare their results with MND dynamics to the final-state rule, they find a significant improvement in intensities. We obtain a similar improvement over the final-state rule.

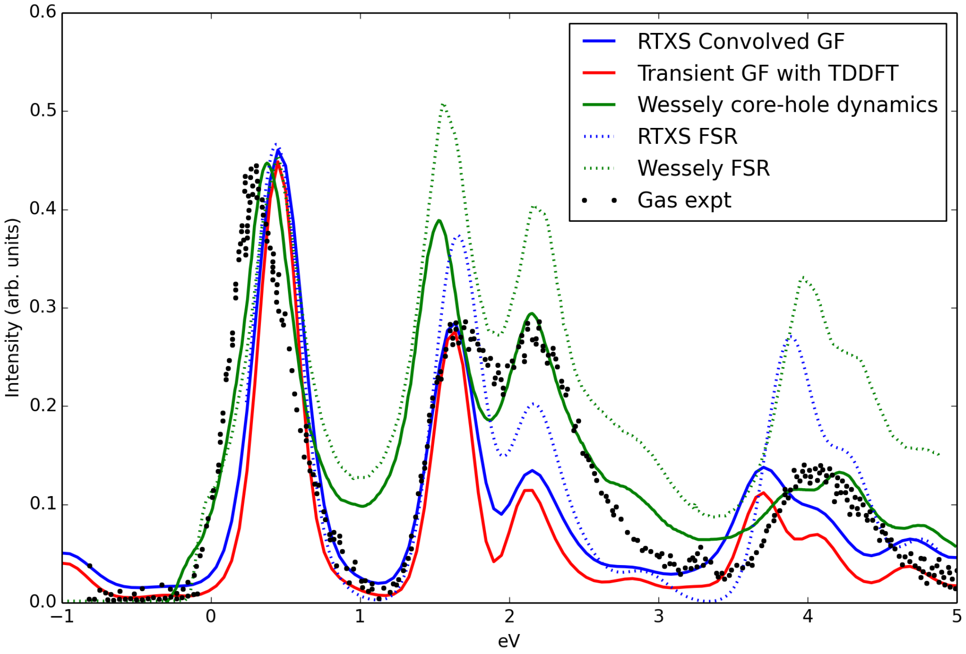

Figure 5.7: C_{60} XAS compared with Wessely *et al.* and experimental XAS. Convolving with g_c improves agreement with experiment slightly. There is a significant improvement over the adiabatically relaxed final-state rule (FSR) in both our's and Wessely's calculations.

In Fig. 5.7, we compare our calculations for C_{60} XAS with experiment and Wessely *et al.* The experiment is for gas phase C_{60} [88]. Most of the features of the spectrum are due to the transient Green's function. Whether we use TDDFT, or fix the valence density at the final-state density, we obtain similar results. Only the results with TDDFT are shown. If the calculation is run for long enough of a total time interval, the TDDFT calculation begins to show negative regions in the spectrum. These negative regions do not show up at the level of broadening that matches experiment, however this is indicative of the errors in our approximations.

There is a significant improvement over the final-state rule in both our's and Wessely's calculations. The nature of the specific corrections to the intensities is also very similar. The intensities of the second, third, and fourth peaks show similar reductions. It is interesting to note that in our calculations the core hole is screened via the relaxation of interacting valence electrons under TDDFT while Wessely *et al.* instead use an adiabatically screened effective core-hole potential. Therefore similar corrections are arrived at via two different approaches.

In convolving the core-hole Green's function with the photoelectron Green's function to obtain the XAS, we see that the core-hole Green's function improves the agreement with experiment slightly. The peaks at 2.2 eV and 4 eV are slightly intensified.

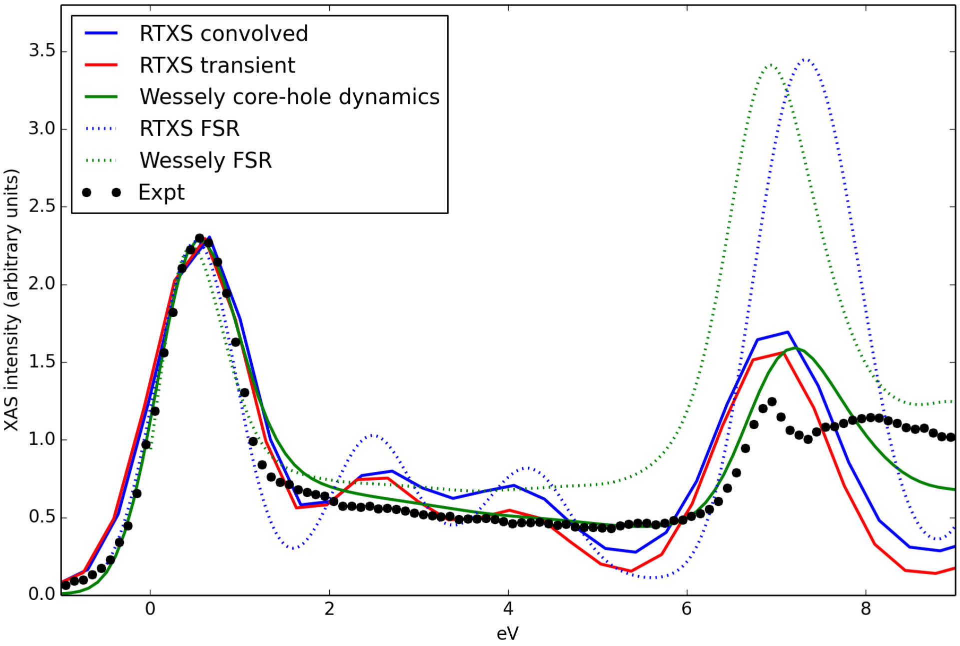

Figure 5.8: Graphite XAS compared with Wessely *et al.* and experimental XAS. Including dynamics improves the intensities over the final-state rule in both theoretical curves.

In Fig. 5.8, we compare our calculations for graphite XAS with experiment [91] and Wessely *et al.* For graphite, we again see a large improvement in intensities compared with the final-state rule, similar to what Wessely *et al.* see in their calculations. The reduction in intensity seen in Wessely *et al.* 's calculations for the σ^* peak at 7 eV is reproduced in our calculations.

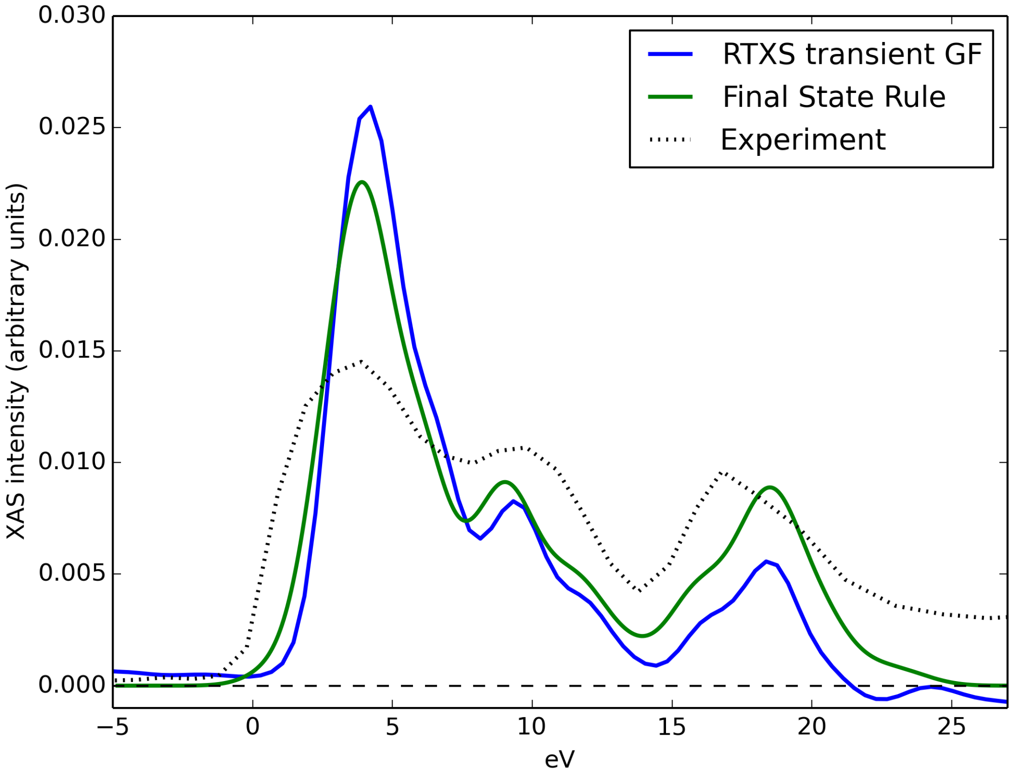

Figure 5.9: Diamond cluster XAS with TDDFT transient Green's function compared with final-state rule and experimental XAS. Core-hole dynamics does not change the spectrum significantly. This diamond cluster is the same 48 carbon atom cluster with hydrogen caps as in previous calculations.

For diamond, we do not find a significant improvement over the final-state rule when introducing core-hole dynamics. However, the region of negative spectrum which shows up in the transient Green's function indicates we may need a better approximation for the transient Green's function in diamond.

5.8 Conclusions

We have developed real-time methods based on the ND formalism to include core-hole dynamics in the calculation of XANES. Our convolved correlation-function and cumulant-expansion method allows the valence electrons to relax in real time and dynamically screen the core-hole. The improvement in XANES follows closely that shown in Wessely *et al.*, who used the MND formalism with an adiabatic approximation for the screening in the effective core-hole potential.

We are also able to analyze the effects of valence-electron core-hole dynamics separately. It appears that including core-hole dynamics of the valence electrons improves agreement with experiment in C_{60}, and is significant in understanding XANES. However, our approach here is limited by containing only intrinsic effects, and we work only within the linear response regime. We have estimated that non-linear effects are most significant in the near edge region, so methods which include non-linear effects should be developed. Also we have used XPS to estimate the accuracy of our calculation of the core-hole Green's function g_c, and while we find a close correspondence with the calculated plasmon frequencies and the experimental plasmon frequencies, we find a large amount of intensity differences, increasing with energy. This difference is estimated to be mostly due to extrinsic effects, with some part due to non-linear effects.

We have taken a first step into real-time core-hole dynamics, and found that we can model some new physical effects which appear to be significant in understanding XANES and XPS. Our studies also indicate effects due to extrinsic and non-linear core-hole dynamics are significant. It will be interesting to see how incorporating these effects elucidates the electronic structure of XANES.

Chapter 6

CONCLUSION

We have developed a general and practical real-time method for modeling dynamics in X-ray spectroscopy. We have reproduced previous linear XAS MND calculations by Wessely *et al.* It is interesting that we obtain similar results without requiring the assumption of adiabatic screening and effectively non-interacting electrons once the screening has occurred. In our model, the screening of the core hole is dynamic and comes about from the evolution of interacting electrons modeled via TDDFT.

Furthermore, our method can be used in more demanding experimental setups for time dependent X-ray spectroscopy. In this way we may explore regimes where there exist no useful approximations for static methods. For example, we may pump the system with an arbitrary potential in real time before creating the core hole and photoelectron. We may also create multiple core hole and photoelectron pairs, at times of our choosing. Other possible extensions include time dependent X-ray emission and Auger emission.

These developments will aid theory to join experiment in the exploration of dynamics in electronic structure. They may be especially relevant for experiments made possible with the recently developed XFELs.

BIBLIOGRAPHY

[1] Vincenzo Carravetta and Hans Agren. Computational x-ray spectroscopy. In *Computational Strategies for Spectroscopy: from Small Molecules to Nano Systems*. John Wiley and Sons, 2011.

[2] Y. Takimoto, F. D. Vila, and J. J. Rehr. Real-time time-dependent density functional theory approach for frequency-dependent nonlinear optical response in photonic molecules. *J. Chem. Phys.*, 127(15):154114, 2007.

[3] L. Triguero, L. G. M. Pettersson, and H. Ågren. Calculations of near-edge x-ray-absorption spectra of gas-phase and chemisorbed molecules by means of density-functional and transition-potential theory. *Phys. Rev. B*, 58:8097–8110, Sep 1998.

[4] Chung-Li Dong, Jinghua Guo, Yang-Yuan Chen, and Chang Ching-Lin. Soft-x-ray spectroscopy probes nanomaterial-based devices. *SPIE Newsroom*, 2007. http://spie.org/x15809.xml (accessed 10-15-2014). doi: 10.1117/2.1200708.0812.

[5] L. Triguero, L.G.M. Pettersson, and H. Ågren. *J. Phys. Chem. A*, 102(52):10599–10607, 1998.

[6] Dan Imre, Ahmed Zewail, John Arthur, Michael Wulff, Richard Neutze, Jerry Hastings, Chi-Chang Kao, and Mark Renner. Femtochemistry. In *LCLS: The First Experiments* [110].

[7] Hidekazu Mimura, Hirokatsu Yumoto, Satoshi Matsuyama, Takahisa Koyama, Kensuke Tono, Yuichi Inubushi, Tadashi Togashi, Takahiro Sato, Jangwoo Kim, Ryosuke Fukui, Yasuhisa Sano, Makina Yabashi, Haruhiko Ohashi, Tetsuya Ishikawa, and Kazuto Yamauchi. Generation of 10^{20}W cm^{-2} hard x-ray laser pulses with two-stage reflective focusing system. *Nature Communications*, 5(3539), 2014.

[8] R. R. Freeman, P. H. Bucksbaum, K. Kulander, L. Young, and R. Falcone. Atomic Physics Experiments. In *LCLS: The First Experiments* [110].

[9] L. Young, E. P. Kanter, B. Krssig, Y. Li, A. M. March, S. T. Pratt, R. Santra, S. H. Southworth, N. Rohringer, L. F. DiMauro, G. Doumy, C. A. Roedig, N. Berrah, L. Fang, M. Hoener, P. H. Bucksbaum, J. P. Cryan, S. Ghimire, J. M. Glownia, D. A. Reis, J. D. Bozek, C. Bostedt, and M. Messerschmidt. Femtosecond electronic response of atoms to ultra-intense X-rays. *Nature*, 466:56 – 61, 2010.

[10] M. Mitchell Waldrop. X-ray science: The big guns. 2014.

[11] M. Marques and E. Gross. Time-dependent density functional theory. In *A Primer in Density-Functional Theory*, volume 620 of *Lecture Notes in Physics*, pages 144–184. Springer, Berlin., 2003.

[12] E. Runge and E. K. U. Gross. *Phys. Rev. Lett.*, 52:997, 1984.

[13] K. Yabana and G. F. Bertsch. Time-dependent local-density approximation in real time. *Phys. Rev. B*, 54:4484–4487, Aug 1996.

[14] P. Nozières and C. T. De Dominicis. Singularities in the X-Ray Absorption and Emission of Metals. III. One-Body Theory Exact Solution. *Phys. Rev.*, 178:1097–1107, Feb 1969.

[15] J. J. Kas, J. J. Rehr, and L. Reining. Cumulant expansion of the retarded one-electron Green function. *Phys. Rev. B*, 90:085112, Aug 2014.

[16] C. D. Wagner, W. M. Riggs, L. E. Davis, and J. F. Moulder. *Handbook of X-ray Photoelectron Spectroscopy.* Perkin-Elmer Corporation, 1979.

[17] P. Hohenberg and W. Kohn. *Phys. Rev.*, 136:B864, 1964.

[18] W. Kohn and L. J. Sham. Self-consistent equations including exchange and correlation effects. *Phys. Rev.*, 140:A1133–A1138, Nov 1965.

[19] D. C. Langreth and M. J. Mehl. *Phys. Rev. B*, 28, 1983.

[20] J. P. Perdew. *Phys. Rev. Lett.*, 55, 1985.

[21] John P. Perdew, Kieron Burke, and Matthias Ernzerhof. Generalized Gradient Approximation Made Simple. *Phys. Rev. Lett.*, 77(18):3865–3868, Oct 1996.

[22] J. P. Perdew and Stefan Kurth. Density functionals for non-relativistic coulomb systems in the new century. In *A Primer in Density Functional Theory* [97].

[23] A. Dreuw, J. Weisman, and M. Head-Gordon. Long-range charge-transfer excited states in time-dependent density functional theory require non-local exchange. *J. Chem. Phys.*, 119, 2003.

[24] C. Rostgaard. The Projector Augmented-wave Method. 2010. https://wiki.fysik.dtu.dk/gpaw/documentation/literature.html (accessed 9-21-2014).

[25] P. E. Blöchl. Generalized separable potentials for electronic-structure calculations. *Phys. Rev. B*, 41:5414–5416, March 1990.

[26] A. J. Lee, F. D. Vila, and J. J. Rehr. Local time-correlation approach for calculations of x-ray spectra. *Phys. Rev. B*, 86:115107, Sep 2012. Copyright (2012) by the American Physical Society.

[27] J. J. Rehr and R. Alben. Vibrations and electronic states in a model amorphous metal. *Phys. Rev. B*, 16(6):2400–2407, Sep 1977.

[28] Fernando D. Vila, J. J. Rehr, H. H. Rossner, and H. J. Krappe. Theoretical x-ray absorption debye-waller factors. *Phys. Rev. B*, 76(1):014301, Jul 2007.

[29] Mathieu Taillefumier, Delphine Cabaret, Anne-Marie Flank, and Francesco Mauri. X-ray absorption near-edge structure calculations with the pseudopotentials: Application to the K edge in diamond and α-quartz. *Phys. Rev. B*, 66:195107, Nov 2002.

[30] H. Ebert. *Rep. Prog. Phys.*, 59:1665, 1996.

[31] M. P. Ljungberg, J. J. Mortensen, and L. G. M. Pettersson. *Journal of Electron Spectroscopy and Related Phenomena*, 184(8):427–439, 2011.

[32] L. Young, E. P. Kanter, B. Krässig, Y. Li, A. M. March, S. T. Pratt, R. Santra, S. H. Southworth, N. Rohringer, L. F. Dimauro, G. Doumy, C. A. Roedig, N. Berrah, L. Fang, M. Hoener, P. H. Bucksbaum, J. P. Cryan, S. Ghimire, J. M. Glownia, D. A. Reis, J. D. Bozek, C. Bostedt, and M. Messerschmidt. *Nature*, 466:56, 2010.

[33] G. F. Bertsch, J.-I. Iwata, Angel Rubio, and K. Yabana. Real-space, real-time method for the dielectric function. *Phys. Rev. B*, 62:7998–8002, Sep 2000.

[34] David C. Langreth. Singularities in the x-ray spectra of metals. *Phys. Rev. B*, 1:471–477, Jan 1970.

[35] V. I. Grebennikov, Yu. A. Babanov, and O. B. Sokolov. Extra-atomic relaxation and x-ray spectra of narrow-band metals. *Phys. Stat. Sol. (b)*, 79(1):423–432, 1977.

[36] O. Wessely, O. Eriksson, and M. I. Katsnelson. Dynamical core-hole screening in the x-ray absorption spectra of graphite, c_{60}, and carbon nanotubes: A first-principles electronic structure study. *Phys. Rev. B*, 73:075402, Feb 2006.

[37] Timofei Privalov, Faris Gel'mukhanov, and Hans Ågren. Role of relaxation and time-dependent formation of x-ray spectra. *Phys. Rev. B*, 64:165115, Oct 2001.

[38] Ulf von Barth and Günter Grossmann. Dynamical effects in x-ray spectra and the final-state rule. *Phys. Rev. B*, 25:5150–5179, Apr 1982.

[39] J. J. Rehr and R. C. Albers. Theoretical approaches to x-ray absorption fine structure. *Rev. Mod. Phys.*, 72:621–654, Jul 2000.

[40] J. Crank and P. Nicolson. *Math. Proc. Cambridge*, 43:50–67, 1947.

[41] P. E. Blöchl. Projector augmented-wave method. *Phys. Rev. B*, 50:17953–17979, Dec 1994.

[42] J. M. Soler, E. Artacho, J. D. Gale, A. García, J. Junquera, P. Ordejón, and D. Sánchez-Portal. *J. Phys.: Condens. Matter*, 14:2745, 2002.

[43] John J. Rehr, Joshua J. Kas, Micah P. Prange, Adam P. Sorini, Yoshinari Takimoto, and Fernando Vila. Ab initio theory and calculations of x-ray spectra. *C. R. Phys.*, 10(6):548 – 559, 2009.

[44] B. Hetenyi. Calculation of near-edge x-ray-absorption fine structure at finite temperatures: Spectral signatures of hydrogen bond breaking in liquid water. *J. Phys. Chem.*, 120:8632–8637, May 2004.

[45] J. Vinson, J. J. Rehr, J. J. Kas, and E. L. Shirley. Bethe-salpeter equation calculations of core excitation spectra. *Phys. Rev. B*, 83:115106, March 2011.

[46] G. Herzberg. *Electronic spectra and electronic structure of polyatomic molecules.* Van Nostrand, New York, 1966.

[47] W. Robert Carper, Larry P. Davis, and Michael W. Extine. Molecular structure of 2,4,6-trinitrotoluene. *J. Phys. Chem.*, 86(4):459–462, 1982.

[48] Fernando D. Vila, Terrence Jach, W. T. Elam, John J. Rehr, and J. D. Denlinger. X-ray emission spectroscopy of nitrogen-rich compounds. *J. Phys. Chem. A*, 115(15):3243–3250, 2011.

[49] A. M. Rappe, K. M. Rabe, E. Kaxiras, and J. D. Joannopoulos. Optimized pseudopotentials. *Phys. Rev. B*, 41:1227–1230, Jan 1991.

[50] W. Kutzelnigg, U. Fleischer, and M. Schindler. In *The IGLO-Method: Ab Initio Calculation and Interpretation of NMR Chemical Shifts and Magnetic Susceptibilities*, volume 23. Springer-Verlag, Heidelberg, 1990.

[51] L.G.M. Pettersson. unpublished.

[52] R. Krishnan, J. S. Binkley, R. Seeger, and J. A. Pople. Self-consistent molecular orbital methods. xx. a basis set for correlated wave functions. *J. Chem. Phys.*, 72(1):650–654, 1980.

[53] Per Skytt, Jinghua Guo, Nial Wassdahl, Joseph Nordgren, Yi Luo, and Hans Ågren. Probing symmetry breaking upon core excitation with resonant x-ray fluorescence. *Phys. Rev. A*, 52:3572–3576, Nov 1995.

[54] J Nordgren, L Selander, L Pettersson, R Brammer, M Bäckström, C Nordling, and H Ågren. Electronic structure of benzene studied in usx emission. *Physica Scripta*, 27(3):169, 1983.

[55] Y. Ma, N. Wassdahl, P. Skytt, J. Guo, J. Nordgren, P. D. Johnson, J-E. Rubensson, T. Boske, W. Eberhardt, and S. D. Kevan. Soft-x-ray resonant inelastic scattering at the c K edge of diamond. *Phys. Rev. Lett.*, 69:2598–2601, Oct 1992.

[56] T. T. Fister, G. T. Seidler, J. J. Rehr, J. J. Kas, W. T. Elam, J. O. Cross, and K. P. Nagle. Deconvolving instrumental and intrinsic broadening in core-shell x-ray spectroscopies. *Phys. Rev. B*, 75:174106, May 2007.

[57] Shunsuke Sato and Kazuhiro Yabana. Personal communication.

[58] G. F. Bertsch and A. J. Lee. Time-dependent mean-field theory for x-ray near-edge spectroscopy. *Phys. Rev. B*, 89:075135, Feb 2014. Copyright (2014) by the American Physical Society.

[59] M. P. Prange, J. J. Rehr, G. Rivas, J. J. Kas, and John W. Lawson. Real space calculation of optical constants from optical to x-ray frequencies. *Phys. Rev. B*, 80:155110, 2009.

[60] A. Sakko, A. Rubio, M. Hakala, and K. Hamalainen. *J. Chem. Phys.*, 133:174111, 2010.

[61] K. Lopata, B. Van Kuiken, M. Khalil, and N. Govind. *J. Chem. Theory Comput.*, 9:3284, 2012.

[62] A. J. Lee, F. D. Vila, and J. J. Rehr. Local time-correlation approach for calculations of x-ray spectra. *Phys. Rev. B*, page 115107, 2012.

[63] In M. Marque, N. Maitra, F. Nogueira, and E. Gross, editors, *Fundamentals of time-dependent density-functional theory*, volume 837 of *Lecture Notes in Physics*. 2012.

[64] K. Ohtaka and Y. Tanabe. *Rev. Mod. Phys.*, 62, 1990.

[65] M. Beck et al. *Phys. Rep.*, 324:1, 2000.

[66] O. Alon. *J. Chem. Phys.*, 127:154103, 2007.

[67] C.A. Ullrich. Time-dependent density-functional theory: Concepts and applications. 2011.

[68] R. van Leeuwen and E. Gross. page 249. Ref. [63].

[69] G. Puddu. *arXiv:1208.0122v3*, 2013.

[70] G. Vignale. *Phys. Rev. A*, 77:062511, 2008.

[71] M. Ruggenthaler and R. van Leeuwen. pages 206–210. Ref. [63].

[72] P. Ring and P. Schuck. The nuclear many-body problem. 1980.

[73] See the URL `http://www.phys.washington.edu/users/bertsch/rt-xfs.tar` or "Supplementary Material" accompanying the published journal article.

[74] K. Ohtaka and Y. Tanabe. *Phys. Rev. B*, 34:3717, 1986.

[75] M. Combescot and P. Nozières. *J. Phys. (Paris)*, 32:913, 1971.

[76] Michael Knap, Aditya Shashi, Yusuke Nishida, Adilet Imambekov, Dmitry A. Abanin, and Eugene Demler. Time-dependent impurity in ultracold fermions: Orthogonality catastrophe and beyond. *Phys. Rev. X*, 2:041020, Dec 2012.

[77] K. Schn̈hammer and O. Gunnarsson. *Solid State Comm.*, 23:691, 1977.

[78] V. Grebennikov, Y. Babanov, and O. Sokolov. *Phys. Status Solidi B*, 80:73, 1977.

[79] T. Privalov, R. Gel'mukhanov, and H. Agren. *Phys. Rev. B*, 64:165115, 2001.

[80] U. von Barth and G. Grossmann. *Physica Scripta*, 21:580, 1980.

[81] A. Kotani and Y. Toyozawa. *J. Phys. Soc. Jpn.*, 35:1082, 1973.

[82] C. Swartz, J. Dow, and C. Flynn. *Phys. Rev. Lett.*, 43:158, 1979.

[83] J.Dow and C. Flynn. *J. Phys. C*, 13:1341, 1980.

[84] L. Feldkamp and L. Davis. *Phys. Rev. B*, 22:4994, 1980.

[85] G. Mahan. *Phys. Rev. B*, 21:1421, 1980.

[86] B. Roulet, J. Gavoret, and P. Nozières. *Phys. Rev.*, 178:1072, 1969.

[87] M. Guzzo, J.J. Kas, F. Sottile, M.G. Silly, F. Sirotti, J.J. Rehr, and L. Reining. Plasmon satellites in valence-band photoemission spectroscopy. *The European Physical Journal B*, 85(9), 2012.

[88] S. Krummacher, M. Biermann, M. Neeb, A. Liebsch, and W. Eberhardt. Close similarity of the electronic structure and electron correlation in gas-phase and solid c_{60}. *Phys. Rev. B*, 48:8424–8429, Sep 1993.

[89] D. M. Poirier and J. H. Weaver. Carbon (as Graphite, Buckminsterfullerene, and Diamond) by XPS. *Surf. Sci. Spectra*, 2, 1993.

[90] Monica Bollani, Johann Osmond, Giuseppe Nicotra, Corrado Spinella, and Dario Narducci. Strain-induced generation of silicon nanopillars. *Nanotechnology*, 24, 2013.

[91] P. A. Brühwiler, A. J. Maxwell, C. Puglia, A. Nilsson, S. Andersson, and N. Måtensson. *Phys. Rev. Lett.*, 74, 1995.

[92] Lars Hedin. On correlation effects in electron spectroscopies and the gw approximation. *J. Phys.: Cond. Mat.*, 11:R489–R528, 1999.

[93] J J Rehr, J A Soininen, and E L Shirley. Final-state rule vs the Bethe-Salpeter equation for deep-core x-ray absorption spectra. *Physica Scripta*, 2005(T115):207, 2005.

[94] A. Poiarkova and J. J. Rehr. *Phys. Rev. B*, 59:948, 1999.

[95] A. Poiarkova and J. J. Rehr. *J. Synchrotron Radiat.*, 8:313, 2001.

[96] E. D. Crozier, J. J. Rehr, and R. Ingalls. In D. C. Koningsberger and R. Prins, editors, *X-Ray Absorption: Principles, Applications, Techniques of EXAFS, SEXAFS, and XANES*, page 375. Wiley, New York, 1988.

[97] C.Fiolhais, F. Nogueira, and M. Marques, 2003.

[98] John P. Perdew and Yue Wang. Accurate and simple analytic representation of the electron-gas correlation energy. *Phys. Rev. B*, 45(23):13244–13249, Jun 1992.

[99] R. Kubo. *J. Phys. Soc. Jpn*, 17:1100, 1962.

[100] E. Artacho, D. Sánchez-Portal, P. Ordejón, A. García, and J. M. Soler. *Phys. Status Solidi B*, 215:809, 1999.

[101] N. Troullier and José Luriaas Martins. Efficient pseudopotentials for plane-wave calculations. *Phys. Rev. B*, 43(3):1993–2006, Jan 1991.

[102] F. Vila, J. J. Rehr, J. Kas, R. G. Nuzzo, and A. I. Frenkel. Dynamic structure in supported pt nanoclusters: Real-time density functional theory and x-ray spectroscopy simulations. *Phys. Rev. B*, 78(12):121404, Sep 2008.

[103] W. H. Press, S. A. Teukolsky, W. T. Vetterling, and B. P. Flannery. *Numerical Recipes in Fortran: The Art of Scientific Computing, Second Edition*, pages 565–566. Cambridge University Press, Cambridge, 1992.

[104] A. Goldoni, R. Larciprete, C. Cepek, L. Sangaletti, S. Pagliara, G. Paulucci, and M. Sancrotti. Investigation of thermally driven surface phenomena in fullerene-based systems using synchrotron radiation photoemission. *Electrochemical Society Proceedings*, 2002-12, 2002.

[105] Y. Takimoto. A real-time time-dependent density functional theory method for calculating linear and nonlinear dynamic optical response. 2008. PhD Thesis, University of Washington.

[106] J. J. Mortensen, L. B. Hansen, and K. W. Jacobsen. Real-space grid implementation of the projector augmented wave method. *Physical Review B*, 71, 2005.

[107] J. Enkovaara, C. Rostgaard, J. J. Mortensen, J. Chen, M. Dulak, L. Ferrighi, J. Gavnholt, C. Glinsvad, V. Haikola, H. A. Hansen, H. H. Kristoffersen, M. Kuisma, A. H. Larsen, L. Lehtovaara, M. Ljungberg, O. Lopez-Acevedo, P. G. Moses, J. Ojanen, T. Olsen, V. Petzold, N. A. Romero, J. Stausholm, M. Strange, G. A. Tritsaris, M. Vanin, M. Walter, B. Hammer, H. Hkkinen, G. K. H. Madsen, R. M. Nieminen, J. K. Nrskov, M. Puska, T. T. Rantala, J. Schitz, K. S. Thygesen, and K. W. Jacobsen. Electronic structure calculations with gpaw: a real-space implementation of the projector augmented-wave method. *J. Phys.: Condens. Matter*, 22, 2010.

[108] M. Walter, H. Hkkinen, L. Lehtovaara, M. Puska, J. Enkovaara, C. Rostgaard, and J. J. Mortensen. Time-dependent density-functional theory in the projector augmented-wave method. *Journal of Chemical Physics*, 128, 2008.

[109] J. B. Hastings, J. Arthur, P. Emma, D. Mills, C. Pellegrini, D. Peter Siddons, R. Tatchyn, A. Toor, and L.-H. Yu. X-ray Laser Physics. In *LCLS: The First Experiments* [110].

[110] Gopal K. Shenoy and Joachim Stöhr. LCLS: The first experiments, 2000.

Appendix A

WHERE TO FIND THE FILES

The RTXS software package contains the code written for this thesis. It includes the main body of code, a modified version of GPAW, and analysis tools and libraries. It can be found at the RTXS webpage.

- RTXS webpage.

  `http://staff.washington.edu/ajylee/rtxs`

Appendix B

RTXS SOFTWARE PACKAGE

The RTXS package implements the real-time methodologies for calculating XAS and XPS that are the subject of the thesis. The package consists of Python code and can be used via a command-line interface or a scripting API. This appendix begins with an overview of version 1.0 of the RTXS package, describes the command-line interface, provides example parameters, describes the scripting API, and finally describes the parameters that control RTXS. Both the command-line interface and scripting API allow the user to read in the same parameters. This allows the user to use the command line for standard tasks and the scripting interface for custom tasks while maintaining consistency. RTXS also provides tools for post analysis.

B.1 Overview

RTXS is based on GPAW [106, 107, 108], which itself is based on the Atomic Simulation Environment (ASE). Much of the code in RTXS revolves around manipulating ASE and GPAW objects, which are coded in Python. Additionally, the RTXS package and interface was made with GPAW conventions in mind.

The main objects in GPAW are the so called "calculator objects." Under GPAW naming conventions, the DFT SCF calculators are members of the class `GPAW`, while the TDDFT calculators are members of the class `TDDFT`. (The naming scheme is due to the fact that originally GPAW could only do DFT calculations, and the TDDFT capability was added later.) Since RTXS manipulates these calculator objects internally to perform calculations, it will be helpful to keep this in mind when learning to use RTXS. Some of the parameters given to RTXS are directly passed on as initialization parameters for the calculator objects. It will be helpful to refer to GPAW documentation on the `GPAW` and `TDDFT` classes to understand the use of these paramaters and the details of the calculations that RTXS performs.

The RTXS package is distributed with several external subpackages, and an install script. The main parts are a modified version of GPAW and the code in the `rtxs/` subdirectory. After installation, refer to the examples subdirectory to find a C60 example. Within the example you will find the `params.py` file and the `xyz` file. In general these are the only files you need to begin a calculation. Run the calculation with the following commands.

B.2 Command line interface

```
rtxs setups
rtxs scf
rtxs seeds
rtxs evolve
```

Multiple steps can be run in one line, like below.

```
rtxs setups scf
```

You can also run

```
rtxs help
```

for a brief description of each command.

The `setups` step creates the PAW setups (see official GPAW documentation). The `scf` step runs the ground state calculation. If you requested a core hole in a PAW setup, as opposed to modeling the core hole as an external field, the `scf` step also finds the ground state with a core hole. The `seeds` step generates the initial states. Finally, the `evolve` step runs the real-time TDDFT propagation.

B.3 Scripting

The main reason for scripting is to perform some custom calculation at each time step of the real time time evolution. This is achieved by providing a custom callback object to the time evolution. A callback class defines a `take_a_step()` method which is called at every step, and a `finalize()` method which is called at the end of time evolution. Both methods take only the implicit `self` argument. RTXS provides the functions necessary for loading the outputs of the PAW setups generation, SCF, and initial state generation steps. Usage of the custom callback and the loading tools will become more clear in the provided example.

B.3.1 Example script

The following example script is a customized version of the `evolve` step. It runs the time evolution while outputting the determinantal correlation function for the valence electrons. You may define your own callback class in place of the `CorrelationCallback` class. Your custom callback needs only to have a `take_a_step()` method which is called at every step, and a `finalize()` method which is called at the end of time evolution. Both methods take only the implicit `self` argument.

```
import numpy as np

from rtxs.file_tools import gpw_dir, mkdir_if_necessary
from rtxs.td import td_params
from rtxs.external_potential import setup_standard_core_hole_vext
from rtxs.correlation import CorrelationCallback, one_body, many_body
import rtxs.td
import rtxs.generate_seeds

import gpaw.tddft
import gpaw.rtxs.options



def _setup_seed(td_calc):
    """NOTE: no paw conversion so compatible with MPI"""
    many_body_seed = rtxs.td.get_init_kpt_u_from_calculator(
        td_calc, np.load(rtxs.generate_seeds.photoelectron_seed_fname))
    rtxs.td.copy_seed(many_body_seed, td_calc)



## Depends on params file
td_calc = gpaw.tddft.TDDFT(rtxs.generate_seeds.td_calc_gpw_file(),
                           **rtxs.td.get_TDDFT_kwargs())

_setup_seed(td_calc)

setup_standard_core_hole_vext(td_calc, time_dependent_strength=lambda t: 1.0)

gpaw.rtxs.options.EVOLVE_HAMILTONIAN = False
```

```
mkdir_if_necessary('out')
delay_time = 1000.

_correlation_callback_g_c = CorrelationCallback(
    td_calc,
    correlation_type=many_body,
    filename='out/correlation_g_c.dat',
    delay=delay_time,
    with_unocc_photoelectrons=False)


if __name__ == '__main__':
    td_calc.propagate(td_params['time_step'], td_params['iterations'],
                      callbacks = [_correlation_callback_g_c])
```

B.4 Parameters (params.py)

The command line steps all depend on the parameters in the `params.py` file. This is actually a valid Python source file which defines variables that are recognized by RTXS. The variables and descriptions are as follows.

RTXS specific parameters

`atoms`

> An ASE `Atoms` object. This defines the coordinates of the atoms in the system, and the boundary conditions. ASE has a rich set of functions for manipulating and creating `Atoms` objects. Refer to official ASE documentation for their use.

`ch_strength`

> A string indicating the PAW core-hole strength at the core-hole site. Use `"nch"` for a zero-strength core hole, `"fch"` for full core hole. Set it to `"xch"` to indicate that the core-hole is modeled using an external potential (see `"vext_strength"`), instead of incorporating the core-hole in the PAW setup.

`ch_site`

> The index of the atom which has a core hole. RTXS provides a convenience function for finding the centermost atom index, `rtxs.atom_tools.centermost_idx(atoms)`.

`constant_scf_hamiltonian`

> Whether to set the Hamiltonian to a constant for all times after the core hole is created. The Hamiltonian used will be the SCF Hamiltonian with the core-hole strength specified by `ch_strength`.

`core_conversion`

> Boolean indicating whether to account for the change in PAW setups when introducing the core hole. This is not necessary if the core hole is modeled via an effective external potential.

`core_hole_response`

A boolean indicating whether to output the core-hole response during the `evolve` step.

`correlation`

The correlation to output in the `evolve` step. Choose between `"G"`, `"g_c"`, `"F"`, or `"all"`. You may also give a list of choices.

`extrinsic`

Boolean indicating whether to include the photoelectron density when calculating the KS density-functional external potential.

`iterations`

Number of iterations for the `evolve` step. The iterations times the time step is the total simulation time. Typical simulation times are about 40 femtoseconds.

`photoelectron_nbands`

Number of levels above the Fermi level for describing the photoelectron. The more levels included, the better the description of the photoelectron. (Internally, the GPAW calculator object's `nbands` parameter will be set to `nbands = -photoelectron_nbands`.)

`time_step`

Time step, in attoseconds, for the `evolve` step.

`vext_strength`

A scalar function of time (attoseconds). Scales the external core-hole potential. Default is `lambda t: 1.0`, i.e. full strength for all times after time $t = 0$. This only applies when setting `ch_strength = "xch"`.

In addition to the above parameters, you may also include the following standard GPAW SCF and TDDFT calculator parameters. These are all optional and may be omitted from the `params.py` file.

Standard GPAW parameters

`xc`

String indicating the XC functional. I recommend `xc="PBE"`.

`h`

Float indicating grid spacing in angstroms. Used in both SCF and TDDFT calculators. Typical values are 0.2 to 0.35.

`maxiter`

Maximum number of SCF iterations. The default is usually enough.

`eigensolver`

Eigenvector solver for scf loop. If the SCF loop does not converge, try “`cg`” for conjugate gradient.

`kpts`

Tuple of integers indicating K-Points used in both the SCF and TDDFT calculations. Example: `(1, 1, 1)`.

`solver`

Optional. String indicating matrix inversion solver for time evolution. If the numerical time evolution has convergence problems, try `solver = "BiCGStab"`.

B.5 Analysis tools

The analysis tools are in the `rtxs.fourier_tools` and `rtxs.analyze_beta` modules. These modules are for analyzing correlation functions and $\beta(t)$, respectively.

The correlation analysis tools rely on the `Dataset` class defined in `rtxs.data`.

The main functions of interest are

`rtxs.fourier_tools.load_correlations(filename)`

Loads a correlation function time series from a file. the output is a `Dataset`.

`rtxs.fourier_tools.spectrum(dataset)`

Fourier analyzes the time series to give a spectrum. Input is a `Dataset`, outputs a `Dataset`.

`rtxs.analyze_beta.transform_beta.spectrum((time, response))`

Fourier analyzes the time series to give $\beta(\omega)$.

`rtxs.analyze_beta.spectrum_from_beta(omega, beta)`

Obtain the spectrum from $\beta(\omega)$.

The `Dataset` class contains some useful methods. One can also extract the data as a `numpy` array, via the properties `Dataset.cols` or `Dataset.pts`. The array obtained from the latter is the transpose of the former. Some of the most useful methods are

`xscale(scale)`

Scales the independent variable.

`yscale(scale)`

Scales the dependent variable(s).

`xshift(shift)`

Shifts the independent variable.

`yshift(shift)`

Shifts the dependent variable(s).

`plot(**kwargs)`

Plots the data. Takes the same arguments as `matplotlib.pyplot.plot`.

B.6 Sample calculation

The following sample `params.py` file and analysis script can be used in a quick calculation of the full Green's function F for an H_2O molecule. It sets up the photoelctron with a projection onto unoccupied states of the ground state Kohn-Sham Hamiltonian. Then it evolves using the final-state Hamiltonian, which is calculated via relaxing the valence density under an external core hole potential.

Place the file in an empty directory, then run

```
rtxs setups

rtxs scf

rtxs seeds

rtxs evolve
```

After the calculation finishes, run the analysis script to produce the included sample output. The parameters are chosen for a fast calculation. For realistic parameters, see the GPAW tutorial at https://wiki.fysik.dtu.dk/gpaw/tutorials/xas/xas.html.

```
## Sample params.py for H2O (must be adjusted for a realistic calc)

import ase, math as ma

# a, d, t only used to set var ‘atoms‘, which is recognized by RTXS.
a = 5.0    # Cell size in angstrom. Should use 12.0 for more realistic calc.
d = 0.9575 # Bond length in angstrom.
t = ma.pi / 180 * 104.51
atoms = ase.Atoms(’OH2’,
                  [(0, 0, 0), (d, 0, 0), (d * ma.cos(t), d * ma.sin(t), 0)],
                  cell=(a, a, a))
atoms.center()

ch_site = 0
## fch, hch, nch, or xch, for full, half, no core hole, external pot core hole
ch_strength = ’xch’

xc=’PBE’
photoelectron_nbands = 10
h=0.35   # grid spacing

core_conversion = False   # not necessary for external core hole
extrinsic = False
constant_scf_hamiltonian = True
correlation = ’F’

time_step = 10.0
iterations = int(20e3 / time_step) # end at 20 fs.
```

```
## plot_sample.py

from rtxs.data import Dataset
from scipytools.plotting import prep_plot, plt
from rtxs.fourier_tools import spectrum_from_file as spec

prep_plot()

## Note ad-hoc shift of 650 eV to smooth correlation fn.
## Tried different shifts to get edge to be around 0.
spec('out/correlation_F.dat', shift=650).real().maxto1().plot()

plt.xlim(0, 15)
plt.xlabel('eV')
plt.ylabel('Intensity (arb. units)')
```

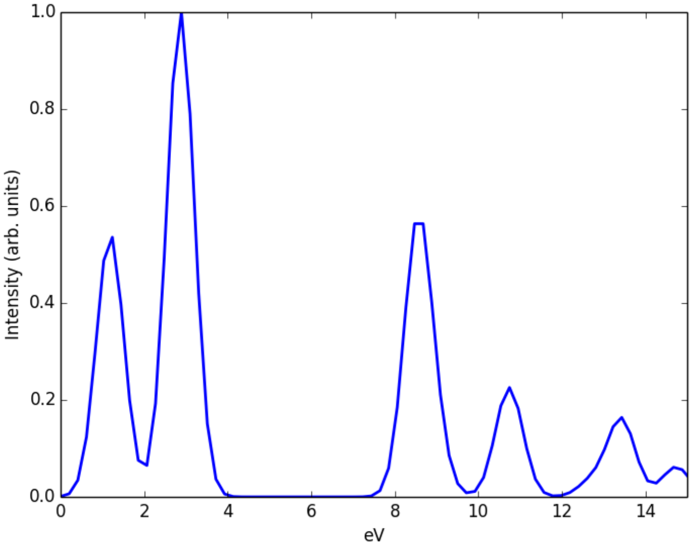

Appendix C

TIME-SHIFTED CORRELATION METHOD FOR XPS AND XAS

The XAS and XPS can be calculated via a determinantal time-correlation approach. We focus on the Green's function F for XAS; the methods are readily adapted to the core-hole Green's function g_c for calculating XPS. We form the excited many-body Kohn-Sham state by taking a determinant of the Kohn-Sham single-particle states,

$$|\mathbf{\Psi}'(t)\rangle = \det\left\{|\psi'_i(t)\rangle\right\}, \tag{C.1}$$

where the index i runs over valence electrons and the photoelectron[1]. The Kohn-Sham valence electrons $\psi'_{i\neq x}(t)$ are initialized to the ground-state valence states obtained via SCF. The photoelectron is initially $|\psi'_x(0)\rangle = n_x(1-\mathcal{P}_{occ})d|c\rangle$, up to a normalization constant n_x, i.e. it is obtained by projecting $d|c\rangle$ onto states not already occupied by valence electrons, then normalizing. We let $\rho'(0)$ be the sum of ground-state density of the valence electrons and the photoelectron density,

$$\rho'(\mathbf{r},0) = \left(\sum_{i\neq x}|\psi'_i(\mathbf{r})|^2\right) + |\langle\mathbf{r}|n_x(1-\mathcal{P}_{occ})d|c\rangle|^2. \tag{C.2}$$

The Kohn-Sham states are evolved under the Hamiltonian

$$H'[\rho(t)] = -\frac{1}{2m}\nabla^2 + v_{\text{Hartree}}[\rho(t)] + v_{\text{XC}}[\rho(t)] + v_c, \tag{C.3}$$

where v_c is the effective core-hole potential. As previously shown, the full Green's function becomes

$$\begin{aligned} F(t) &= i\langle\mathbf{\Psi}'(0)|\mathbf{\Psi}'(t)\rangle \\ &= i\det\langle\psi'_i(0)|\psi'_j(t)\rangle. \end{aligned} \tag{C.4}$$

---

[1] When calculating the core-hole Green's function g_c for comparison with XPS, the index i runs over only valence electrons, i.e. we leave the photoelectron out from the determinant and the density.

The last determinant is simply a determinant of the overlap matrix.

Calculating the Green's function $F(t)$ in Eq. (C.4) reveals this approximation is inaccurate, however. The spectrum has regions which are negative, as in the example for C_{60} in Fig. C.1. This was discussed previously and can be explained by the fact that using two single-determinantal Kohn-Sham Hamiltonians to approximate the double-determinantal Kohn-Sham Hamiltonian does not accurately model the relative phase between the two determinants.

C.1 Time-shifted correlation approximation

One method to recover a reasonable approximation to the true many-body correlation function from the TDDFT Kohn-Sham states is by waiting until the density becomes almost constant. This can happen in any system with a sufficiently large number of degrees of freedom, and without any pathological symmetries which might prevent the system from reaching such an equilibrium. For a detailed justification for shifting the correlation function, see Section D.1. From here on I shall refer to this method as the "time-shifted correlation method" or the "delayed determinantal method."

The true many-body state evolves with a time-independent Hamiltonian after the X-ray absorption event at $t = 0$. Therefore, its time-correlation function after time $t = 0$ can be arbitrarily shifted to a starting time t', as long as we only consider times $t > t'$. We have

$$|\mathbf{\Psi}'(t)\rangle = \sum_i e^{-i\epsilon_i t} a_i |\mathbf{\Phi}'_i\rangle \tag{C.5}$$

$$\begin{aligned}\langle \mathbf{\Psi}'(t')|\mathbf{\Psi}'(t)\rangle &= \sum_i \langle \mathbf{\Phi}'_i| a_i^* e^{i\epsilon_i t'} e^{-i\epsilon_i t} a_i |\mathbf{\Phi}'_i\rangle \\ &= \sum_i a_i^* a_i e^{-i\epsilon_i (t-t')}\end{aligned} \tag{C.6}$$

where $\mathbf{\Phi}'_i$ are many body eigenstates with energy ϵ_i. From this it is clear that we may obtain the spectrum by Fourier transforming $\langle \mathbf{\Psi}'(t')|\mathbf{\Psi}'(t)\rangle$ with respect to $\Delta t = t - t'$. I choose t' to be after the density is nearly constant, because in that case, it is expected that the determinantal KS correlation function is a good approximation to the true correlation

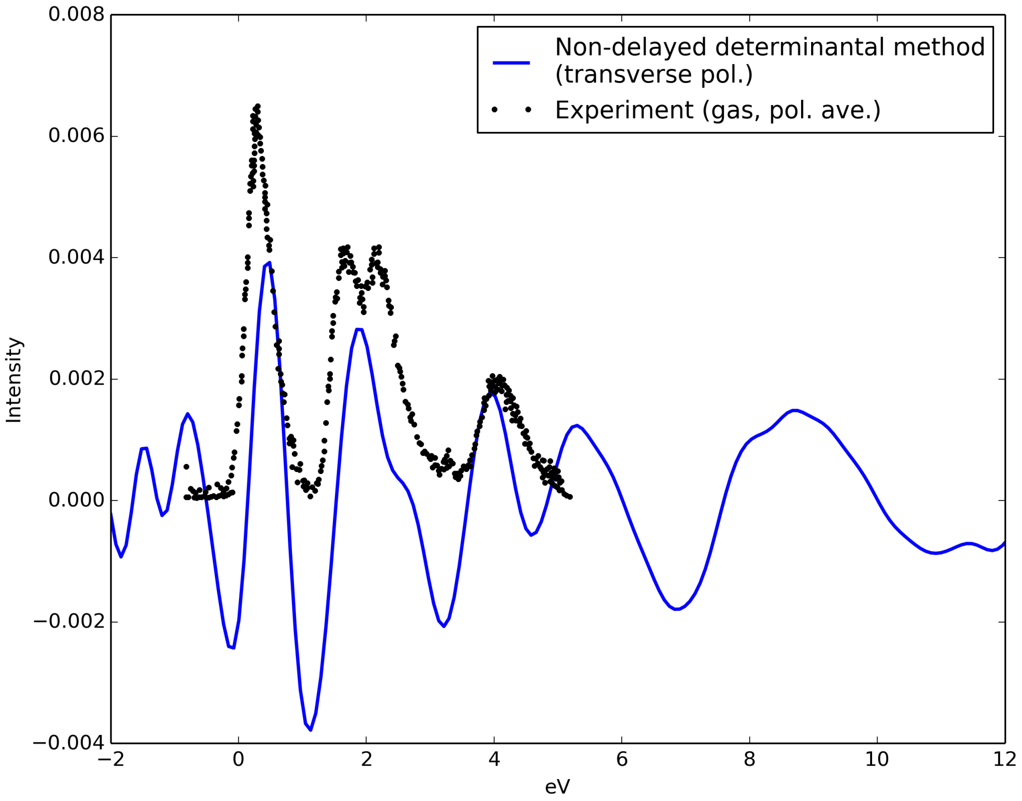

Figure C.1: C_{60} XAS calculated with unshifted correlation function, with polarization transverse to the surface of the molecule. The correlation function begins at time $t = 0$, i.e. the time of creation of the core hole and photoelectron. Although a spectrum appears to be distinguishable, there are large negative regions in the spectrum. The experiment is polarization averaged.

function, up to a total energy shift[2]. For example, when calculating XPS for C_{60}, one can estimate from the response to the core-hole potential in Fig. C.2 that the density becomes nearly constant about 1 fs after the core hole is created. At the time $t = t'$, since the density has only small oscillations, and is approximately constant, we may simply hold the density

---

[2] See Section D.1 for explanation.

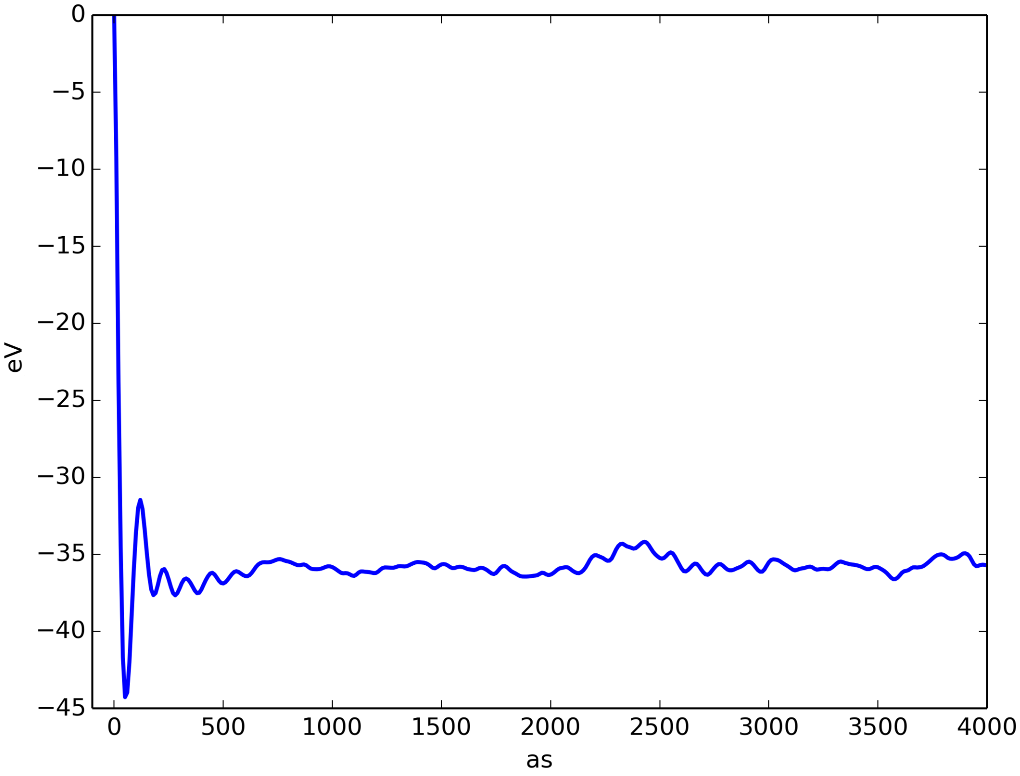

Figure C.2: C_{60} $\int d^3x v_c(\mathbf{x})\rho'(\mathbf{x},t)$ with core-hole strength set to 1. At 1 fs the large oscillations have diminished. Therefore the density is estimated to be approximately at equilibrium at that time. Note that in this figure there is no extrinsic density, i.e. the photoelectron is not included.

fixed at $\rho'(t')$ and obtain the KS determinantal correlation function

$$F(t-t') = i \det_{ij} \langle \psi_i'(t') | e^{-iH'[\rho'(t')](t-t')} | \psi_j'(t') \rangle. \tag{C.7}$$

The spectrum calculated from this correlation function will not have the negative regions which were previously encountered, which were caused by the time dependence of the KS Hamiltonian and the lack of a double determinantal phase correction. In practical terms we evolve the system via RT-TDDFT a certain amount of time and then freeze the Hamiltonian and record the correlation function. We use various values for the time shift t' to see when the spectrum calculated in this way converges. By conducting a convergence study it was found that the XPS converges soon after 1 fs. The XAS calculated by this method appears to converge between 10 to 15 fs.

In waiting for our system to reach statistical equilibrium, it is important to note that we are able to do this in our model because the core hole does not decay unless we change its occupation explicitly. In a real experiment the core hole might decay before the system reaches equilibrium. In Neon, for example, the Auger process has a relaxation time of about 2.5 fs [8].

C.2 Results

Both the cumulant method and time-shifted correlation method can be used to obtain the core-hole Green's function g_c for approximating XPS. In Fig. C.3, we see that the calculations with the time-shifted correlation are in good agreement with the cumulant method and experiment in terms of overall shape of the spectrum. However, the weight of the satellites is significantly larger with the time-shifted correlation method, especially at low frequencies[3]. The differences between the time-shifted correlation method and the cumulant could be due to nonlinear effects. The cumulant method only applies to the linear regime, whereas the time-shifted correlation method does not require that assumption. As was seen in Fig. 5.5, nonlinear effects are more prevalent for smaller losses.

For C_{60}, the time-shifted correlation method appears to converge, up to an overall energy shift of about 2 eV, at about 15 fs. The total energy shift may converge at some later time, and will be studied in the future.

In Fig. C.4, we see that the time-shifted correlation method gives a better peak position for the peak at 4 eV than the calculation of $\Im G * g_c$ using our convolved Green's function formulation with an unshifted TDDFT photoelectron correlation function G convolved with g_c from the cumulant method. The intensity of the peak just above 2 eV is also improved over the convolved Green's function method. Given that using a delayed correlation function

---

[3] Note that the quasi-particle peaks in the time-shifted correlation calculations are significantly smaller than in the cumulant method. The quasi-particle peaks are much larger than the satellite peaks and are not shown in the figure. The experiment has been scaled so the quasi-particle peak matches the quasi-particle intensity from the cumulant.

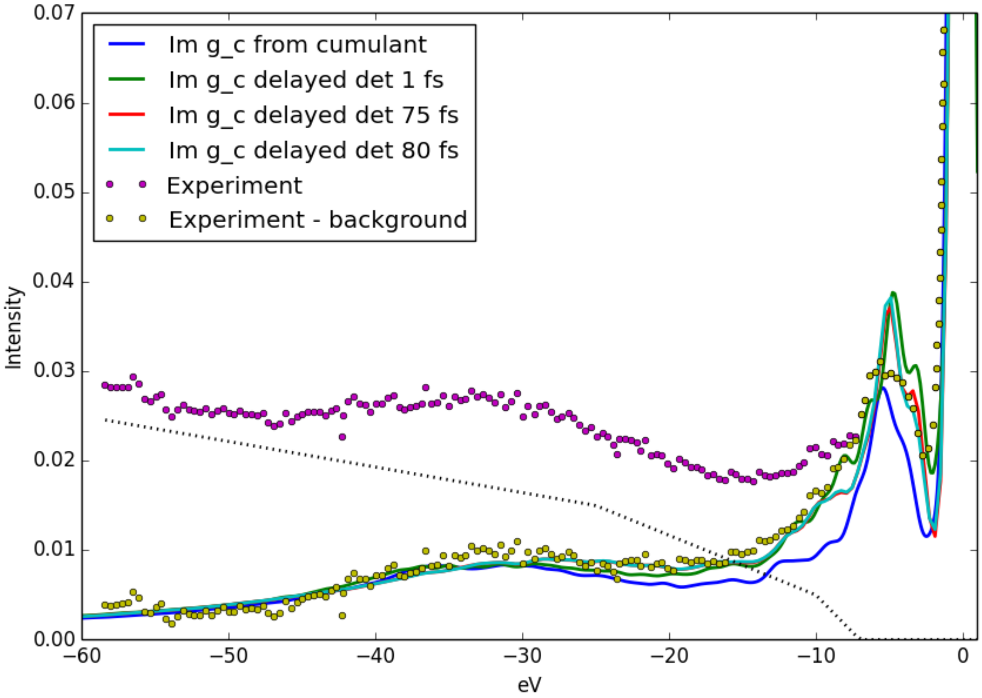

Figure C.3: C_{60} XPS with delayed determinantal correlation compared our cumulant method. The peak positions are improved. However, the two central peaks are slightly diminished in strength and become slightly further from experiment.

is more rigorous than the non-delayed correlation-function, due to our ignoring the cross-term phase-correction in the double-determinantal XC functional, it is encouraging that the comparison with experiment improves.

Note that in the time-shifted correlation calculations, we include the density of the photoelectron in the TDDFT time evolution. Without the extrinsic density, the method converges only after 80 fs and the intensities become very different from experiment, although the energies are still similar. We have not studied the effect of including density of the photoelectron in the unshifted photoelectron correlation function, but plan to in the future.

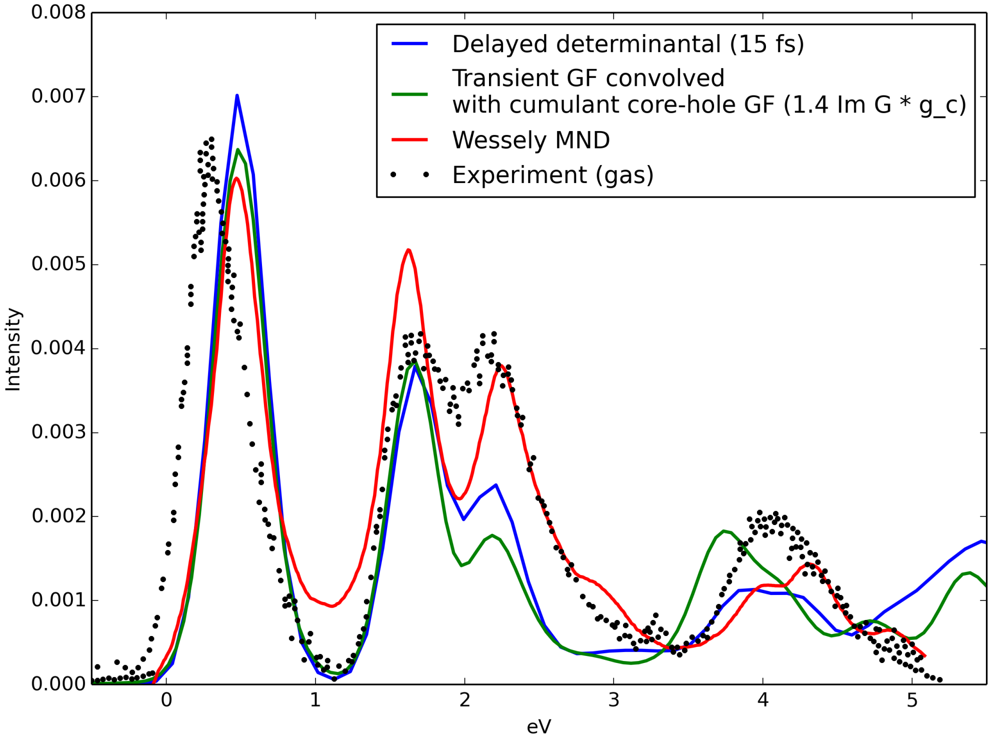

Figure C.4: C_{60} polarization-averaged XAS calculated using the time-shifted correlation method compared to our convolved Green's function calculation from Chapter 5. The peak position at 4 eV is improved, and the intensity at 2.2 eV is also improved over the convolved Green's function method.

C.3 Discussion

The time-shifted correlation method has broad applicability since it requires only a large enough number of degrees of freedom such that the density reaches statistical equilibrium in a practical number of time steps. The method can be applied to any disturbance which can be modeled within TDDFT. For example, we might consider a double X-ray absorption event, where we would simply wait a certain time after the second absorption event, and then calculate the determinantal correlation function with a static Kohn-Sham Hamiltonian.

Another example is a time-dependent external potential. To obtain the spectrum at a certain time t_0, one would freeze the time-dependent potential at t_0, wait until $t' > t_0$ for the system to equilibrate, and then calculate the shifted correlation function. In the pumped case, we may want to calculate the energy difference between the unprobed (but pumped) state and the state which has absorbed a probe photon. Our correlation function would replaced by the time-dependent overlap between these two states, and we would need to evolve them both explicitly.

This method has a few advantages over previously discussed methods. It is not limited to linear regime in core-hole strength which is a limitation of the cumulant method. Also, the time-shifted correlation method does not have the same difficulty with low satellite energies which shows up in calculations of β. The function $\beta(\omega)$ has a tendency to become negative at $\omega < 1$ eV, whereas the time-shifted correlation method has no such problem.

One can consider modifying the time-shifted correlation method by calculating the spectrum in frequency space by diagonalizing the Kohn-Sham Hamiltonian after the freeze time t'. However, as noted in [105], the real-time method is much simpler than frequency space calculations because a frequency space calculation would involve summation over the configuration space of determinants constructed from the single-particle eigenstates of the Kohn-Sham Hamiltonian. The real-time method includes all such configurations via a single time-dependent determinant.

One might ask how this method is distinct from evolving using a final-state rule Hamiltonian. In the final-state rule, the valence electrons are adiabatically relaxed and therefore do not have any shake up, i.e. the final-state density is the “ground state” density in the presence of the effective core hole potential. In the time-shifted correlation method, the system never reaches the “ground state” from the final-state rule. The valence electrons exhibit shake-up for all time. The Kohn-Sham Hamiltonian at t', $H'[\rho'(t')]$, is obtained via TDDFT time evolution, not via an SCF loop as is done in obtaining the final-state Kohn-Sham Hamiltonian, $H'[\rho'_{SCF}]$. Also note that after we wait for the Kohn-Sham system to reach statistical equilibrium, its spectrum is expected to approximate the spectrum of the true electronic system which evolves under a time-independent Hamiltionian. The true electronic system has a time-independent spectrum, exhibiting shake-up for all times $t > 0$.

Finally, it would be interesting to study the expansion of G in Eq. 4.15. One may obtain G by deconvolving F and g_c, i.e. by simply taking the quotient $G(t) = F(t)/g_c(t)$. We can then compare with expansions of G. In this way we can use the determinantal method to gain insight into the convolved correlation and cumulant method.

C.4 Method for calculating double X-ray absorption

As mentioned above, one can use the time-shifted correlation method to calculate the spectrum for a double-absorption event. This can be modeled by creating the first core hole and photoelectron as usual, then time evolving under TDDFT, creating a second core hole and photoelectron, evolving until the density equilibrates, then stopping the update of the Kohn-Sham Hamiltonian and starting recording of the determinantal correlation function. When creating the second core hole, one would simply project out the occupied states so that $(1 - \mathcal{P}_2^{\mathrm{occ}})d|c_2\rangle$ is orthogonal to the first photoelectron and the valence electrons at the time of creation. By having double excitations, more pronounced dynamical effects could be explored.

C.5 Conclusion

We have developed the time-shifted correlation method for modeling core-hole dynamics using RT-TDDFT. For C_{60}, the method gives a similar XPS spectrum to the cumulant method, and the XPS calculated via both methods are similar to experiment for low energy losses. At energy losses above 10 eV both exhibit a similar plasmon in comparison to experiment but at lower intensities, perhaps due to the lack of extrinsic effects in the core-hole Green's function used to model the XPS. The time-shifted correlation function has an advantage that it does not assume linear response, and so it may be able to model nonlinear effects more accurately than the cumulant method. For C_{60} XAS the time-shifted correlation calculation gives a similar result to the convolved Green's function calculation, with a slight improvement in agreement with experiment.

More calculations comparing the time-shifted correlation method to the cumulant method for XPS and to the convolved Green's function method for XAS are presently underway for systems like titanium dioxide (rutile) and graphite.

Appendix D

TECHNICAL CONSIDERATIONS

D.1 Development of time-shifted correlation function

In this section the time-shifted correlation function is developed in detail. Notice that for a time-independent Hamiltonian, the start time of the true many-body correlation function can be arbitrarily time shifted, and we obtain the same function of time. This can be seen from the following derivation.

$$\begin{aligned}\langle \mathbf{\Psi}(t_0)|\mathbf{\Psi}(t_1)\rangle &= \langle \mathbf{\Psi}(0)|U^\dagger(t_0)U(t_1)|\mathbf{\Psi}(0)\rangle \\ &= \langle \mathbf{\Psi}(0)|U(t_1-t_0)|\mathbf{\Psi}(0)\rangle \\ &= \langle \mathbf{\Psi}(0)|\mathbf{\Psi}(t_1-t_0)\rangle\end{aligned} \tag{D.1}$$

In XAS the Hamiltonian is time-independent after the absorption event, so the correlation function can be shifted to any time after absorption of the photon.

In Section D.2, it is shown that one may obtain overlaps of many-body states from overlaps of KS states. Applying this to the time-shifted correlation function, we see that one may obtain the time-shifted correlation function via double-determinantal KS TDDFT. Without rigorously developing such a formalism, one can nontheless attempt to approximate it with ordinary, single-determinantal KS TDDFT, for long enough time shifts.

Notice that given enough degrees of freedom, the density at long times should eventually reach statistical equilibrium, unless there is some special symmetry which should be broken by considering phonons. In our calculations we then approximate the density as a constant as far as the KS Hamiltonian is concerned. This assumes that the small density fluctuations do not significantly affect the KS density-functional external potential, although the small fluctuations in fact correspond to the spectrum we intend to calculate. With a constant KS Hamiltonian, the phase correction from the true double-determinantal KS TDDFT can only affect the spectrum by a constant energy shift.

In summary the approximation entails: (1) Evolve the KS states $\psi_i'(t)$ under RT-TDDFT until some time t'. (2) Holding the Hamiltonian constant at t', calculate the spectrum from the time-shifted correlation function

$$F(t-t') = i \det_{ij} \langle \psi_i'(t') | e^{-iH'[\rho'(t')](t-t')} | \psi_j'(t') \rangle. \tag{D.2}$$

(3) Converge the calculation with respect to the time shift t'.

An alternative would be to allow the Hamiltonian to update for all times, so in step (2) we would instead calculate

$$F(t-t') = i \det_{ij} \langle \psi_i'(t') | e^{-i\mathcal{T} \int_{t'}^{t} dt H'[\rho'(t)]} | \psi_j'(t') \rangle, \tag{D.3}$$

where $\mathcal{T}$ is the time-ordering operator. Another interesting alternative is to calculate a "tail correlation function" instead. We may calculate the tail end of the unshifted correlation function $\langle \mathbf{\Psi}'(0) | \mathbf{\Psi}'(t) \rangle$ for t greater than some cutoff t' such that the system has reached equilibrium after t'. This can be used to estimate the power spectrum.

D.2 Physical overlaps from KS overlaps

In Chapter 4 it was shown that in the case of XAS, the true autocorrelation function $\langle \mathbf{\Psi}_x(0) | \mathbf{\Psi}_x(t) \rangle$ is equivalent to the corresponding autocorrelation function from double-determinantal KS TDDFT. Let us now extend the XAS scenario and generalize our results to arbitrary overlaps. The essential idea is to correlate a single external electron to the two many-body states $\mathbf{\Psi}_0$ and $\mathbf{\Psi}_1$ for which we want to obtain the overlap. In other words, the many-body system is in a superposition of $\mathbf{\Psi}_0$ and $\mathbf{\Psi}_1$, such that each of $\mathbf{\Psi}_0$ and $\mathbf{\Psi}_1$ is correlated with a different state of the external electron. In this case the overlap $\langle \mathbf{\Psi}_0 | \mathbf{\Psi}_1 \rangle$ can be extracted from the integral $\int d^3x V_s(\mathbf{x}) \rho(\mathbf{x})$, where V_s is a potential which connects the two states of the single external electron but does not disturb the rest of the system, and $\rho(\mathbf{x})$ is the total density of the system plus the external electron.

To begin, consider any system of electrons, $|\mathbf{\Psi}_{\text{sys}}\rangle$, evolving under some Hamiltonian $\mathcal{H}$. We may attach an extra electron far away, so that the system is now $|\mathbf{\Psi}\rangle = |\mathbf{\Psi}_{\text{sys}}\rangle \wedge |\psi_s\rangle$, where "$\wedge$" denotes the antisymmetric tensor product. The $|\psi_s\rangle$ electron acts as a switch, hence the s subscript. When we kick it with some laser potential V_s at frequency ϵ_s we can flip the switch. The shape and frequency of V_s is such that it only affects the switch electron. The switch electron can be placed in a potential trap shaped such that our laser can easily create transitions between only the ground state and the first excited state of the switch, which differ by the energy ϵ_s. Let us call these stationary single-particle states $|0\rangle$ and $|1\rangle$. We can set up the potential trap and pick the spacial form of the laser field such that $\langle 0|V_s|0\rangle = 0 = \langle 1|V_s|1\rangle$ holds[1]. This is analogous to how our X-ray flips the core electron "switch." Let us specify the system as

$$|\boldsymbol{\Psi}(t)\rangle = a_0|\boldsymbol{\Psi}_0(t)\rangle \wedge |0\rangle + a_1|\boldsymbol{\Psi}_1(t)\rangle \wedge |1\rangle e^{-i\epsilon_s t}, \tag{D.4}$$

where a_0 and a_1 are amplitudes chosen by us, and $\boldsymbol{\Psi}_0$ and $\boldsymbol{\Psi}_1$ are states of the system also chosen by us. If we expand the integral of the total density ρ times V_s at some time $t = t_s$, we obtain the overlap

$$\begin{aligned}\int d^3x V_s(\mathbf{x})\rho(\mathbf{x}, t_s) &= a_0^* a_1 \langle \boldsymbol{\Psi}_0(t_s)|\boldsymbol{\Psi}_1(t_s)\rangle\langle 0|\hat{V}_s|1\rangle e^{-i\epsilon_s t_s} + h.c. \\ &= 2\Re a_0^* a_1 \langle \boldsymbol{\Psi}_0(t_s)|\boldsymbol{\Psi}_1(t_s)\rangle\langle 0|\hat{V}_s|1\rangle e^{-i\epsilon_s t_s}.\end{aligned} \tag{D.5}$$

Since $|\boldsymbol{\Psi}_0\rangle$ and $|\boldsymbol{\Psi}_1\rangle$ can be prepared in any arbitrary state, we have essentially obtained the real part of the overlap for any two states from the density. Note that ϵ_s, a_0, a_1 are chosen by us in preparing the scenario. We can just modify a_1 by a phase and obtain the imaginary part, completing the missing part of the overlap. Since we have relied only on the density, this means we may use TDDFT to obtain the necessary densities and therefore the overlap of arbitrary states[2].

Applying the above to double-determinantal KS TDDFT, we can obtain any overlap directly from KS determinantal overlaps. In particular, for any system we may obtain a correspondence between the true correlation function and the KS determinantal correlation function. However, this depends on us having a good enough XC kernel. It must be a highly non-local XC kernel to handle the correlation between the switch and the rest of the system. One method to get around this is to wait for the density to reach statistical equilibrium,

---

[1] For example, if $|0\rangle$ has s-wave symmetry and $|1\rangle$ has p-wave symmetry, we can pick V_s to be a localized dipole field.

[2] That is, assuming one can successfully prepare the scenario in a way that is compatible with TDDFT. In practice we have made this assumption without rigorously checking it.

and then approximating the phase correction from the true double-determinantal XC as an oscillating phase factor at a single frequency, as described in Section D.1.

We apply the switch scenario to obtain a time-shifted correlation function as follows. Suppose $\mathbf{\Psi}_0$ is a state which has absorbed an X-ray photon at time t_0, and $\mathbf{\Psi}_1$ is the state which has absorbed an X-ray at time t_1. Note that the X-ray field aimed at the system is different than the V_s which is aimed at the switch. By setting them up this way, $\mathbf{\Psi}_0$ and $\mathbf{\Psi}_1$ are the same state but time shifted by $t_1 - t_0$. We may obtain the autocorrelation function by taking the overlap of these states. One might note a difficulty in setting up this scenario. Obtaining the equivalence between the KS density and the true density formally requires the state be created by exciting the ground state with some potential. If we excite the ground state with an actual laser field, we are unable to actually prepare $\mathbf{\Psi}_0$ and $\mathbf{\Psi}_1$ in purely excited states, i.e. there will always exist some amplitude for them to be in the ground state. However, these complications do not prevent us from recovering the overlap with straightforward modifications to the above treatment.

D.3 Component density equivalence

We show for the XAS scenario described in Section 4.2 that the component densities for the KS and true systems are equivalent. We then extend the results to the system-plus-switch scenario from Section D.2.

Let us label the KS ground-state and excited densities ρ_g^{KS} and ρ_x^{KS} respectively, and label the true ground-state and excited densities ρ_g and ρ_x respectively. We want to show that $\rho_g^{KS} = \rho_g$ and $\rho_x^{KS} = \rho_x$.

To begin, note that the true total density ρ is the same as the KS total density ρ^{KS}. Also note that before the absorption of the X-ray photon, $\rho(t < 0) = \rho_g$ so we can establish the correspondence for ground state densities, $\rho_g^{KS} = \rho_g$.

Let us now consider the zero frequency components of the densities. We have

$$\bar{\rho} = |a_g|^2\rho_g + |a_x|^2\bar{\rho}_x \tag{D.6}$$

$$\bar{\rho}^{KS} = |a_g^{KS}|^2\rho_g + |a_x^{KS}|^2\bar{\rho}_x^{KS}. \tag{D.7}$$

$$\begin{aligned} \Rightarrow |a_x^{KS}|^2\bar{\rho}_x^{KS} &= |a_x|^2\bar{\rho}_x + (|a_g|^2 - |a_g^{KS}|^2)\rho_g \\ &= |a_x|^2\bar{\rho}_x + (|a_x^{KS}|^2 - |a_x|^2)\rho_g. \end{aligned} \tag{D.8}$$

With the assumption that $|a_x|^2 = |a_x^{KS}|^2$, this implies that $\bar{\rho}_x^{KS} = \bar{\rho}_x$.

Now we note that the cross terms in the total time-dependent density oscillate at X-ray frequencies while ρ_x and ρ_x^{KS} only oscillate at UV-vis frequencies. Therefore for every frequency $\omega \neq 0$ in the UV-vis regime we may separate $\rho_x(\omega)$ and $\rho_x^{KS}(\omega)$ from the cross terms and arrive at the correspondence for each frequency component,

$$\rho_x^{KS}(\omega) = \rho^{KS}(\omega) = \rho(\omega) = \rho_x(\omega). \tag{D.9}$$

Since we have now established that the zero and nonzero frequency components match, we have $\rho_x^{KS}(t) = \rho_x(t)$. This completes the derivation.

Note that it may not be necessary to assume $|a_x|^2 = |a_x^{KS}|^2$. This may be derivable by considering the full time dependence of the X-ray field exciting the system, as in Chapter 3. I leave the exploration of this possibility for the future.

To adapt the above to our system-plus-switch scenario from Section D.2, we could choose the switch frequency to be in a completely different regime than the oscillations of the component densities. This would allow us to separate the cross terms in the density from the ground-state and excited-state component densities, similarly to the above. Therefore the above derivation can be adapted and applied to the system-plus-switch scenario.

VITA

Andrew Lee graduated from the California Institute of Technology with a B.S. in Physics in 2008. He was a graduate student in Physics at the University of Washington, Seattle from 2008 to 2014.